Journal of Sedimentary Research

Journal of Sedimentary Research, 2023, v. 93, 741–775
Research Article
DOI: 10.2110/jsr.2023.018

BRAIDED-RIVER ARCHITECTURE OF THE TRIASSIC SWARTBERG MEMBER, KATBERG FORMATION, SOUTH AFRICA: ASSESSING AGE, FLUVIAL STYLE, AND PALEOCLIMATE AFTER THE END-PERMIAN EXTINCTION

MARTIN R. GIBLING,[1] RUOFEI JIA,[2,3] ROBERT A. GASTALDO,[2] JOHANN NEVELING,[4] AND HERIBERTO ROCHÍN-BAÑAGA[5]

[1]*Department of Earth and Environmental Sciences, Dalhousie University, Halifax Nova Scotia B3H 4R2, Canada*
[2]*Department of Geology, Colby College, Waterville, Maine 04901, U.S.A.*
[3]*Department of Civil and Environmental Engineering, Massachusetts Institute of Technology, Cambridge, Massachusetts 02139, U.S.A.*
[4]*Council for Geosciences, Private Bag x112, Silverton, Pretoria, South Africa 0001*
[5]*Jack Satterly Geochronology Laboratory, Department of Earth Sciences, University of Toronto, Ontario M5S 3B1, Canada*

ABSTRACT: **The Triassic Katberg Formation has played a central role in interpreting the end-Permian ecosystem crisis, as part of a hypothesis of aridification, vegetation loss, and sediment release in continental settings. We use drone images of an inaccessible cliff near Bethulie to investigate the Swartberg member, a braided-fluvial body 45 m thick, describing *remote outcrop facies* to identify geomorphic units and using spatial analysis to estimate their proportions in 2-D sections. Here the Swartberg member comprises three channel belts within shallow valleys, the lowermost of which is ~500 m wide and incised into lacustrine deposits. The component channel bodies consist mainly of trough cross-bedded sand sheets (48%) and channel-scour fills (28%). Recognizable bars (15%) comprise unit bars with high-angle slipfaces and mounded bar cores (components of mid-channel compound bars), bars built around vegetation, and bank-attached bars in discrete, probably low-sinuosity conduits. Abandoned channels constitute 8% and 16% of flow-parallel and -transverse sections, respectively. When corrected for compaction, the average thalweg depth of the larger channels is 3.9 m, with an average bankfull width of 84 m, scaling broadly with the relief of the bars and comparable in scale to the Platte and South Saskatchewan rivers of North America. The fluvial style implies perennial but seasonably variable flow in a vegetated landscape with a humid paleoclimate. The northward paleoflow accords with regional paleoflow patterns and deposition on a megafan sourced in the Cape Fold Belt, where the Swartberg member represents the avulsion of a major transverse-flowing river.**

U-Pb dating of *in situ* and reworked pedogenic carbonate nodules from below the base of the Swartberg member yielded Anisian to Ladinian ages (Middle Triassic), younger than the previously assumed Early Triassic age and implying that considerable gaps in time exist in the succession. An assessment of the interval spanning the lower to mid Katberg Formation is needed to reevaluate the inferred unidirectional trend in fluvial style, aridification, and fossil distributions in this condensed, disjunct succession.

INTRODUCTION

The end of the Permian marked the most severe crisis in the Phanerozoic history of life, when more than 90% of marine species became extinct during a short-lived biosphere collapse (Benton and Newell 2014; Zhu et al. 2019). On land, the extinction period was marked by a profound loss of vertebrate families (Benton and Newell 2014), a decrease in invertebrate bioturbation (Buatois et al. 2021), and a decline in plant species richness (Looy et al. 2001; McElwain and Punyasena 2007). An enhanced flux of sediment and acidified soil material has also been reported (Algeo and Twitchett 2010; Sephton et al. 2015). The currently favored killing model highlights the Siberian and Emeishan large igneous provinces, with the main phase of extinction possibly triggered by the emplacement of extensive sills (Bond and Grasby 2017; Burgess et al. 2017; MacLeod et al. 2017). Multiproxy datasets based on geochemistry, sedimentology, and paleontology document the destabilization of the carbon cycle and Earth system in the marine and terrestrial spheres. This has been attributed to a combination of warming, release of greenhouse gases, anoxia, acidification of land and oceans, ozone depletion, and toxic-metal poisoning (Algeo et al. 2011).

For the terrestrial realm, changes in fluvial style across the extinction level provide important evidence for ecosystem alteration (e.g., Newell et al. 1999; Arche and López-Gómez 2005; Davies et al. 2010; Midwinter et al. 2017; Zhu et al. 2019). In the Karoo Basin of South Africa (Fig. 1A), Permian–Triassic outcrop belts with abundant vertebrate fossils have played a central role in evaluating trends in fluvial style and paleoclimate (Smith 1995; Abdala et al. 2006; Viglietti et al. 2016; Smith et al. 2020; Retallack 2021) (Table 1). A key post-extinction stratigraphic unit is the Triassic Katberg Formation (Fig. 1B), characterized by its relatively arenaceous character when compared with the adjacent Balfour and Burgersdorp formations (Groenewald 1996). Neveling (2004) recognized an upward-thickening and -coarsening trend in the formation, culminating in stacked cliff-forming sandstones in the middle to upper part. He proposed the term Swartberg member for this sandstone-rich interval, based on the cliff that caps Swartberg Koppie (hill) on the Free State farms of Bethel,

Published Online: October 2023
 1527-1404/23/093-741

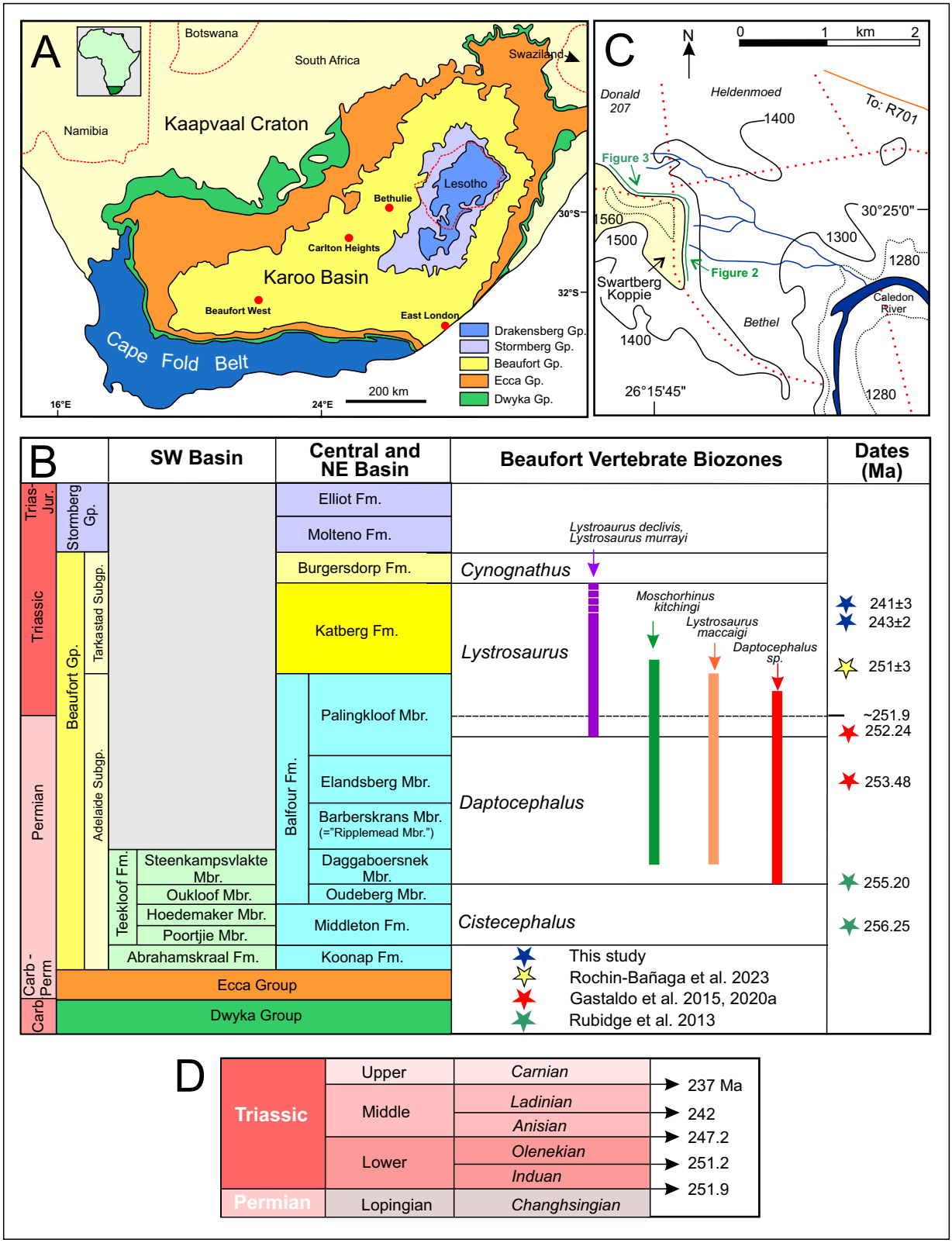

FIG. 1.—**A)** Geological map of the Karoo Basin, southern Africa, extending onto the Kaapvaal Craton, with study area near Bethulie. Inset shows generalized map of Africa, with map area in dark green. Modified from Bordy and Paiva (2021). **B)** Generalized litho- and vertebrate biostratigraphy of the Karoo Basin succession, in chronostratigraphic context. Vertebrate-assemblage zone boundary assignments after Viglietti (2020) and Botha and Smith (2020). Age assignments: the middle of the *Cistecephalus* and base of the *Daptocephalus* AZs (blue stars) is from Rubidge et al. (2013); the Elandsberg Member (red star) is after Gastaldo et al. (2015); the base of

Heldenmoed, and Donald 207 (Fig. 1C; Facies E of Smith and Botha-Brink 2014). Strata below the Swartberg member are referred to informally as the lower Katberg Formation, and the thickness of sandstone units and average grainsize decrease above the Swartberg member. Due to its thickness and prominence in outcrops, the Swartberg member has been considered a useful lithostratigraphic marker to correlate localities across the basin (Botha et al. 2020).

The sandbed rivers that laid down the Katberg Formation have been linked to sediment transport under a relatively warm and dry climate (Stavrakis 1980; Hiller and Stavrakis 1984; Smith and Botha-Brink 2014). Several authors have attributed this fluvial style to aridification, vegetation dieback, and enhanced landscape erosion associated with the end-Permian crisis (Ward et al. 2000, 2005; Viglietti et al. 2018; Botha et al. 2020). These and other features of the formation have been extrapolated worldwide as characteristic of fluvial regimes associated with the extinction (Zhu et al. 2019). However, a rapid and unidirectional drying trend in the Karoo Basin has been disputed (Neveling et al. 2016a, 2016b; Li et al. 2017; Gastaldo et al. 2014, 2019a, 2019b, 2020a) and studies elsewhere have documented little change in paleoenvironment across the extinction level (Fielding et al. 2019, 2021; Ji et al. 2023).

Two problems exist with using the Katberg Formation to infer ecosystem dynamics. The first problem is the paucity of accessible outcrop and a consequent lack of detailed architectural analysis beyond the proximal outcrop belt in the Eastern Cape and northeast Free State provinces (Groenewald 1996). The formation crops out in low escarpments with exposures in gullies (dongas) and on largely inaccessible mountain tops. Consequently, the fluvial systems have been characterized mainly in roadcuts where the strata are limited in thickness and extent, yielding measured sections but few extensive lateral profiles (Neveling 2004; Gastaldo et al. 2021). Studies to date have broadly characterized the Katberg Formation as composed of thick, linear and multi-storied channel bodies (Groenewald 1996; Neveling 2004) separated by mudrock intervals. The latter yield evidence of landscape stasis (Gastaldo and Demko 2011) as evidenced by paleosols (Gastaldo and Rolerson 2008; Pace et al. 2009) and the preservation of vertebrate burrows (Bordy et al. 2010; Bordy and Krummeck 2016).

To provide a more comprehensive assessment of fluvial architecture and, by inference, paleoclimate for the Swartberg member at Swartberg Koppie, we employ an unmanned aerial vehicle (UAV, or drone) to generate 2-D photomosaics and 3-D models for the largely inaccessible cliff. This locality has yielded some 80% of the vertebrate fossils used to interpret a terrestrial end-Permian extinction event (Gastaldo et al. 2019a) and is one of eight classic localities where a changeover in fluvial style has been reported (Ward et al. 2000, 2005).

The second issue concerns the age of the Katberg Formation. Several workers (Neveling 2004; Botha and Smith 2006; Smith and Botha-Brink 2014, their Fig. 1) assigned the formation at Swartberg Koppie to the Induan stage of the Early Triassic (Fig. 1D). This assessment was based on the presence of vertebrates placed in the *Lystrosaurus declivis* Assemblage Zone (AZ), which has traditionally been considered to represent the post-extinction biosphere (but see Gastaldo et al. 2021). To date, geochronometric constraints are lacking, although Gastaldo et al. (2018) reported that the unit lies in a normal-polarity magnetozone. We use laser ablation inductively coupled plasma mass spectrometry (U-Pb LA-ICPMS; Davis and Rochín-Bañaga 2021) to date calcite cements of nodules from paleosols and pedogenic nodule conglomerates (Pace et al. 2009) in the hillslope more than 70 m below the base of the Swartberg member.

GEOLOGIC SETTING

Stratigraphy and Tectonics

The Karoo Basin developed as a foreland basin associated with the Cape Fold Belt (Hälbich 1992; Gresse et al. 1992; Catuneanu et al. 1998; Hancox et al. 2002; Johnson et al. 2006). The fold-and-thrust belt borders the southern and western coast of South Africa and forms part of an extensive orogenic belt from Argentina to Antarctica, linked to subduction of the paleo-Pacific Plate. Extending north from the Cape Fold Belt onto the Kaapvaal Craton, the Karoo Basin has an area of 700,000 km^2 and contains some 12.5 km of Carboniferous to Jurassic strata of the Karoo Supergroup (Fig. 1B), the greater part of which accumulated in a continental interior. The basin was situated at about 50° S by the end of the Triassic (Seton et al. 2012). Carboniferous to Early Permian glacial deposits of the Dwyka Group (Isbell et al. 2008) were followed by marine turbidites (Ecca Group: Sixsmith et al. 2004; Cairncross et al. 2005), deltaic deposits (Waterford Formation of the Ecca Group: Rubidge et al. 2012), and fluvial endorheic strata of the Beaufort Group (Gulliford et al. 2017). Beaufort fluvial styles in the eastern part of the basin (east of 24°) include Middle Permian meandering systems of the Balfour Formation (Smith 1987, 1995), a fluvial style that is considered to have dominated the landscape until latest Permian time (Barberskrans Member). Thereafter, the Elandsberg and Palingkloof members of the Balfour Formation were reported to mark a changeover to a low-sinuosity system (Smith 1995; Ward et al. 2000, 2005; Smith and Botha-Brink 2014; Viglietti et al. 2018), passing up into braided systems of the Katberg Formation of the Tarkastad Subgroup. The younger Triassic succession includes the high-sinuosity fluvial system of the Burgersdorp Formation (Hancox 1998) and the braided-fluvial Molteno Formation of the Stormberg Group (Turner 1983).

In the southwestern part of the basin near Beaufort West, the Lower Beaufort Group (upper part of the Abrahamskraal Formation and lower part of the Teekloof Formation) have been attributed to a range of high- and low-sinuosity fluvial systems, with no single style predominant but with an upward transition to higher-sinuosity systems (Wilson et al. 2014; Gulliford et al. 2014; Bordy and Paiva 2021). The paleoclimate has been considered relatively arid for much of the Permian succession, based on evidence from sedimentary structures, paleosols, and assessments of fluvial style (Table 1).

The Katberg Formation is about 1000 m thick in coastal exposures at East London, with coarser pebbly sandstone. The rock unit thins and fines northward to a few hundreds and then tens of meters over a distance of several hundred kilometers, consisting largely of fine- to very fine-grained sandstone in the Bethulie area (Neveling 2004; Gastaldo et al. 2019a). The base of the lower member is defined at a sharp increase in the ratio of sandstone to mudstone above the Palingkloof Member (Groenewald 1996), thickening upwards into the thick sandstones of the Swartberg member above. Sandstone-dominated bodies at the level of the Swartberg member can be traced for kilometers in cliff faces along the strike of mountain ridges. This exposure pattern results from the resistance of the sandstone bodies, with the adjacent valleys marking fine-grained, interfluvial units (now eroded) that were formerly laterally equivalent at ridge-top level. Exposures along cliff faces and in valley floors represent variously oriented longitudinal and transverse profiles of the ancient river systems (Sasajima et al. 2015; Gastaldo et al. 2019b). Jurassic dolerite intrusions cut the outcrops locally, associated with continental breakup and the emplacement of the Karoo Large Igneous Province.

←

the *Lystrosaurus* AZ is after Gastaldo et al. (2020a) and the base of the Katberg Formation is after Rochín-Bañaga et al. (2023), both at Nooitgedacht; and the Permian–Triassic boundary is after Burgess et al. (2014) in the Tarkastad Subgroup, following Gastaldo et al. (2015, 2021). **C)** Map of Bethel/Heldenmoed/Donald 207 farm with contours in meters. Green line shows the exposure of the informal Swartberg member along Swartberg Koppie. Dashed red lines mark farm boundaries as depicted on 3026AD Tampasfontein 1:50,000 map. **D)** Triassic stages and dates, from Ogg et al. (2016).

TABLE 1.—*Fluvial interpretations for some Permian to Triassic formations of the Beaufort Group, Karoo Basin. Note that the inferred settings are based on analysis of widely separated localities across a large area of the basin.*

Rock Unit	Inferred Fluvial Setting	References
Lower to Upper Triassic		
Molteno and Elliot formations	***Braided channels*** (Molteno Fm.), with coarse grain size, scoured surfaces, transverse bars, and trough cross-beds prominent. Perennial flow with variable discharge and channel switching, in a humid temperate climate.	Turner 1983; Bordy et al. 2004.
	High-sinuosity channels and floodplains (Elliot Fm.), with desiccation cracks and seasonal flow.	
Burgersdorp Formation	***High-sinuosity or anastomosing channels***, with frequent avulsion. Floodplains with crevasse splays and playa lakes. Relatively arid, with desiccation cracks, more humid at higher levels.	Hiller and Stavrakis 1980, 1984; Hancox 1998; Groenewald 1996.
Katberg Formation, Swartberg member	***Braided channel system***, vertically stacked channel bodies in three channel belts, maximum thalweg depth averages 3.9 m. Geomorphic units include sand sheets with dunes and plane beds, channel scours, bartop channels, mid-channel and unit bars grouped into compound bars, bars and pools around vegetation, and abandoned channels. Smaller, probably **low-sinuosity channels** have bank-attached bars, benches, and accretionary banks. Channels occupied shallow valleys with local tributaries and lakes blocked by alluvium. Perennial flow with variable discharge, relatively humid but seasonal paleoclimate.	This study.
	Braided channels with transverse bars, sandy banks, and flat-lying units with high flow-strength features. Vertical accretion prominent, lateral accretion and downstream accretion rare. Small ***low-sinuosity channels*** at the tops of some braided channel belts. Subordinate floodplain, playa-lake, and lake deposits.	Johnson 1976; Hiller and Stavrakis 1980, 1984; Stavrakis 1980; Groenewald 1996; Ward et al. 2000; Hancox et al. 2002; Neveling 2004; Botha and Smith 2006.
Katberg Formation, lower member	***Low-sinuosity or anastomosing channels***, prominent incised bases and multistoried. Channel bodies up to 3–5 m thick (lenticular fixed channels), with sheetflood deposits. Channel gravel lags of pedogenic carbonate and mudstone, with sand-sized pedogenic mud aggregates, indicate episodes of aggradation, degradation, and soil formation. Overall coarsening upward from isolated sandstone bodies with mudstone to sandstone-rich deposits of the Swartberg member. Relatively arid, seasonal paleoclimate.	Ward et al. 2000; Botha and Smith 2006; Pace et al. 2009; Smith and Botha-Brink 2014.
Includes Permian–Triassic boundary		
Palingkloof Member of Balfour Formation	***Low-sinuosity channels***, represented by ribbon and sheet sandstones with rare lateral accretion and gullied basal contacts. Reddish-brown mudrocks and laminated shale laid down in playa lakes. Calcic paleosols. Relatively arid paleoclimate, with desiccation cracks.	Smith 1995; Ward et al. 2000, 2005; Botha and Smith 2006; Smith and Botha-Brink 2014; Botha et al. 2020.
Middle to Upper Permian		
Abrahamskraal and Teekloof formations	***High- and low-sinuosity channels***, point bars (locally exhumed), mid-channel bars, and strong discharge fluctuations. Systems confined to unconfined, channel scour and filling influenced by early cementation. Floodplain, crevasse-splay, and lake deposits. No single fluvial style dominant, a range of hydrodynamic processes, ephemeral flow. Upward change from downstream accretion to lateral accretion, linked to retrogradational stacking and backstepping of the tectonic front. Relatively arid and seasonal paleoclimate, pseudomorphs after gypsum, desiccation cracks, rain prints, rill casts, and adhesion structures.	Stear 1978, 1980, 1983, 1985; Hiller and Stavrakis 1984; Smith 1980, 1987, 1993a, 1993b; Gulliford et al. 2014, 2017; Wilson et al. 2014; Bordy and Paiva 2021.

Depositional packages and unconformities in the Karoo Basin have been linked to episodes of thrust loading and relative quiescence in the Cape Fold Belt (Turner 1983; Hiller and Stavrakis 1984; Catuneanu et al. 1998; Catuneanu and Elango 2001; Viglietti et al. 2017). Earlier tectonic analysis suggested that hinterland deformation and flexural subsidence was active from late Carboniferous to at least the end of the Triassic (Hälbich 1992; Gresse et al. 1992; Bordy et al. 2004; Catuneanu et al. 2005). Recent research using $^{40}Ar/^{39}Ar$ muscovite plateau ages has indicated a major phase of deformation between about 253 and 250 Ma, across the Permian–Triassic boundary and possibly overprinting earlier

events (Blewett and Phillips 2016; Hansma et al. 2016; Blewett et al. 2019). However, the precise correlation of tectonic events in the Cape Fold Belt with rock units in the Karoo Basin remains uncertain (Bordy and Paiva 2021).

Much of the Permian and Triassic succession was probably deposited on large distributive fluvial systems (DFS, or megafans; Weissmann et al. 2010) that built northwards from the Cape Fold Belt, generating northward and locally radiating paleoflow patterns (Turner 1983; Hiller and Stavrakis 1984; Gulliford et al. 2014; Wilson et al. 2014; Bordy and Paiva 2021). Consistent with a DFS model, Gulliford et al. (2014) noted similar paleocurrents in early frontal splays (precursor drainage) and younger channel belts (main prograding system) in the Abrahamskraal and Teekloof formations. The Katberg Formation has been attributed to a pulse of thrusting and the progradation of a clastic wedge with a large sandy braided system (Smith 1995; Catuneanu et al. 1998, 2005), although Ward et al. (2000) later suggested a predominantly climatic interpretation for the sandy fluvial systems. For megafans in general and those of the Karoo Basin in particular, resolving the effects of tectonics and climate has proved challenging (Bordy and Paiva 2021).

Swartberg Koppie Locality

The Swartberg Member is named for an exposure capping an escarpment on Bethel 763 Farm, Free State Province, between the intersection of the R207 and the Caledon River, some 30 km northeast of Bethulie (S 30.419256°, E 026.259594°; Fig. 1C). Exposure is restricted to cliff faces with nearly horizontal strata along Swartberg Koppie, which rises $>$ 200 m from the adjacent valley to an elevation of $\sim$ 1565 m. The cliff comprises two long, steep faces that are broadly at right angles and curve into each other at an outcrop corner. The South–North (S–N) face is about 1 km long, with 492 m of nearly continuous cliff exposure at its northern end (Fig. 2). The East–West (E–W) face is 675 m long (Fig. 3), although only $\sim$ 100 m of the face that adjoins the S–N face is well exposed. Areas of overlap between photomosaics of the two faces are marked on the composite drone images of Figures 2 and 3, which show the locations of photos and interpreted panels. The outcrop ends abruptly at the top of Swartberg Koppie.

Despite playing a central role in an end-Permian terrestrial-extinction model, architectural features at Swartberg Koppie have not been described in detail. This is largely due to the sheer nature of the outcrop, which is accessible for only 3 m at the base. Dolerite sills and dikes a few meters wide run obliquely and discontinuously through the S–N face (but not the E–W face). Strata are locally displaced but can be correlated across the intrusion, and some areas appear to have been thermally affected.

METHODS

Swartberg Koppie Data Acquisition

Two UAVs were deployed to obtain orthogonal images of the cliff, a DJI Phantom 3 Pro and a DJI Mavik Pro. Waypoint paths were set before each flight, with geo-referenced images taken every two seconds to ensure $>$ 80% overlap. Images were captured in JPEG format to manage the large amount of field data, with preliminary models constructed on site between successive flights to ensure that sufficient images had been acquired. The GPS software tagged each image with metadata on longitude, latitude, and relative altitude above ground level, for use in building 2-D and 3-D outcrop models. Altitude data in the metadata set vary because they are referenced from the take-off location and are calculated using the UAV's barometer and GPS system.

Digital images were imported into Agisoft Metashape Pro (http://www.agisoft.com/; Supplemental Materials S2, S3), generating 2-D photomosaics and 3-D virtual outcrop models through structure-from-motion. The

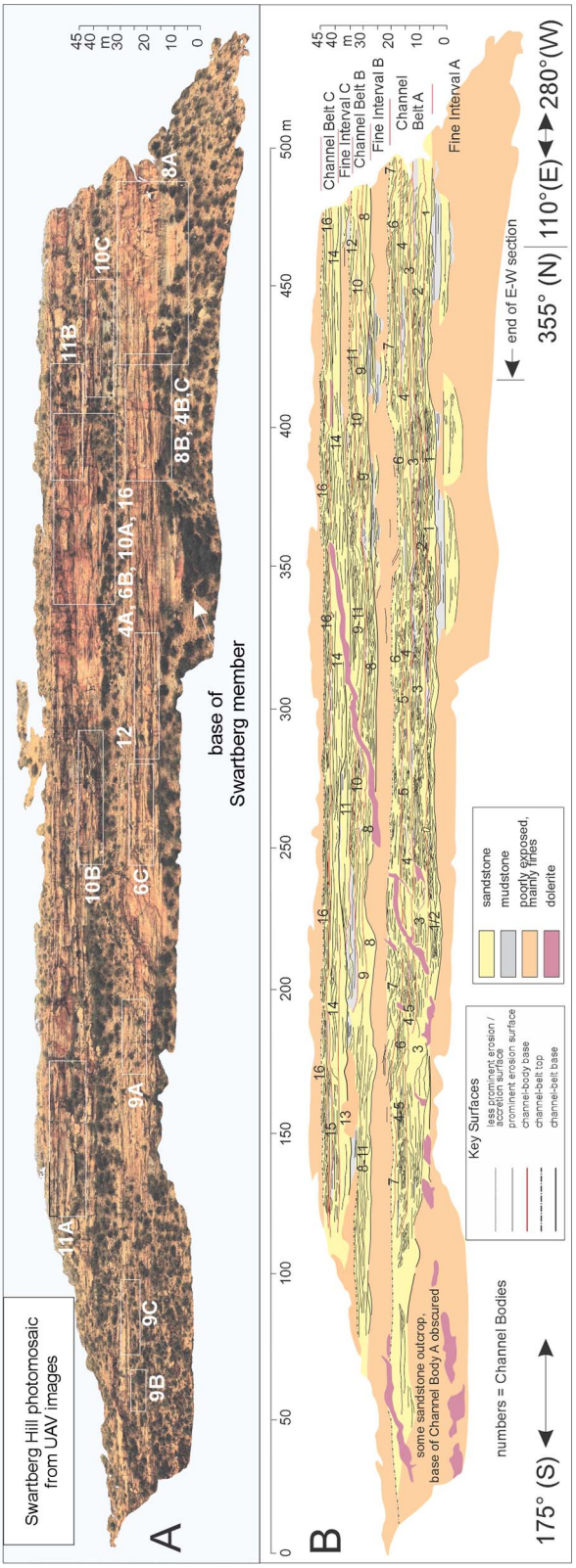

FIG. 2.—**A)** Uninterpreted and **B)** interpreted composite image of the Swartberg Koppie exposure (S–N profile). "End of E–W section" denotes area of overlap with Figure 3. Locations of later figures are shown in Part A. The outcrop of the Swartberg member comprises three channel belts separated by fine-grained intervals, with an aggregate thickness of 45 m.

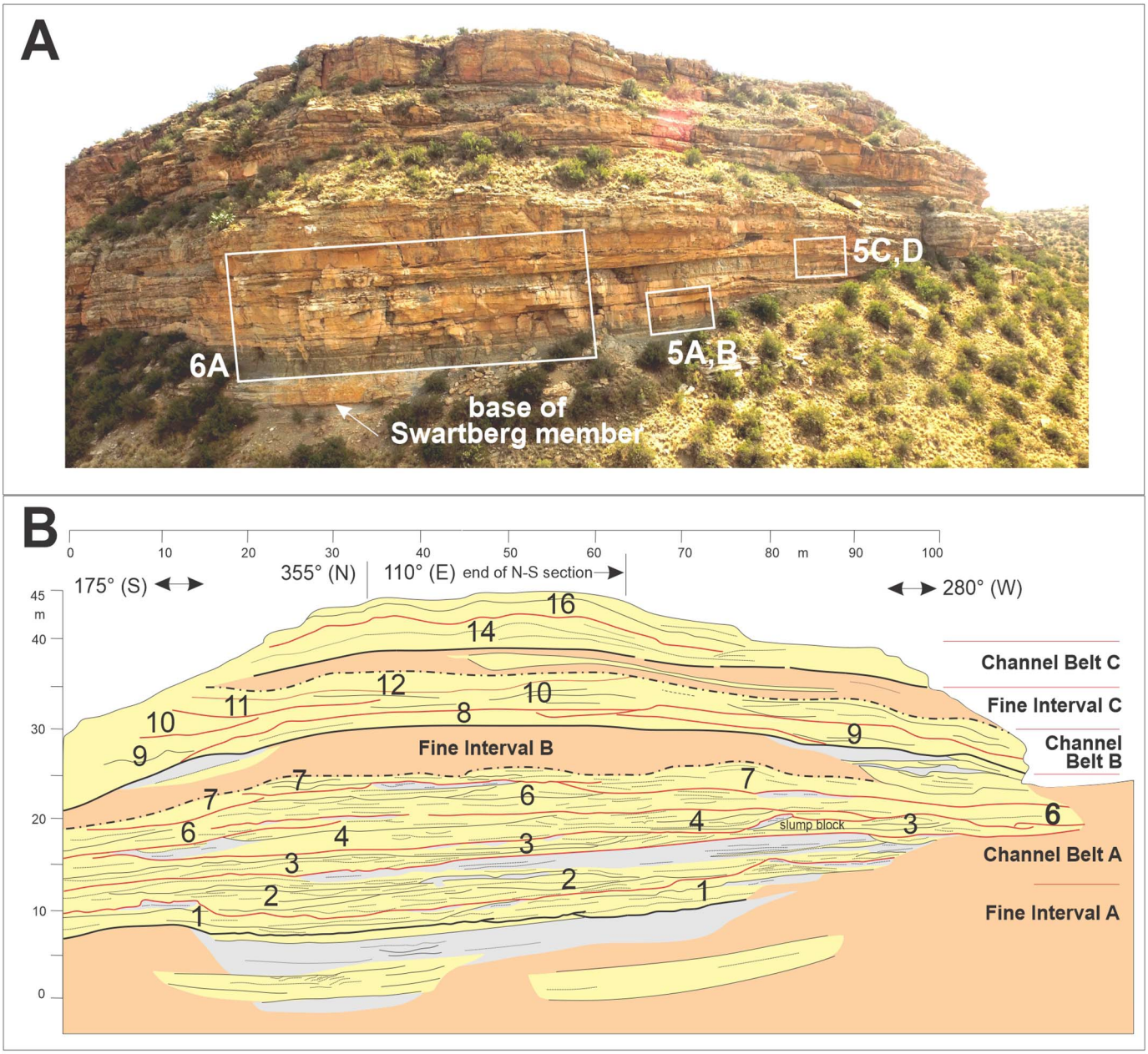

FIG. 3.—**A)** Uninterpreted and **B)** interpreted composite image of the Swartberg Koppie exposure (E–W profile). "End of S–N section" denotes area of overlap with Figure 2. The three channel belts shown in Figure 2 continue around the outcrop corner into the E–W profile.

workflow included initial generation of a sparse point cloud (Stonesifer et al. 2018), followed by a dense point cloud, construction of meshes, and eventual texturing in RGB space. The final model textures used four JPEG tiles with 8192 × 8192 pixels, generating sufficient resolution to recognize key elements of stratal geometry, which can be further viewed from different perspectives by zooming and rotating the 3-D model.

Metashape models were exported to interactive PDF files (Supplemental Material S2) that were imported into virtual-reality tools (Stonesifer et al. 2018). Orthogonal views of the two cliff faces were captured with the highest resolution available. A 10-m scale bar was added to each model using the built-in measurement tool in Metashape, and measurements presented in the results section originate from orthogonal screen shots that use these scale bars. Architectural analysis is based primarily on the S–N face using the digital model, supplemented by close-up images from the original flight. Due, in part, to insufficient image overlap, the stratal tracing along the E–W face only partly reflects the original outcrop, and our evaluation of this area has relied on the original drone images and photomosaics. Compared to 2-D photo-stitching software that may require considerable manual effort, the automated system of Agisoft Metashape Pro overcomes the challenge in identifying accurate control points caused by low color contrast in the Karoo setting.

Analysis of UAV Images

We use a conceptual *Landscape Systems* approach in characterizing the Swartberg member, based on reconstructions of the alluvial landscape as it might have appeared in a bird's-eye view (Gibling et al., in press; see also Ghinassi and Ielpi 2017; Nesbit et al. 2018). Using detailed tracings of the

cliff face, we analyze facies and facies successions, geomorphic units, and fluvial architecture, inferring the paleoflow direction in this part of the basin and estimating paleodischarge. The interpretations draw on studies of modern sandy and gravelly braided rivers for which subsurface profiles are available from ground-penetrating radar (GPR), using radar facies to link surface morphology to preserved channel-bar complexes. Fine-scale sedimentological features are typically below the resolution of the UAV images, limiting an assessment of depositional processes, but the orthogonal photomosaics and 3-D models provide an exceptional opportunity to establish larger-scale architectural features.

Analysis centered around the manual tracing of stratal surfaces on the S–N and E–W 2-D photomosaics, carried out at high resolution using CorelDRAW 2019© and yielding an estimated accuracy of 0.1 m. All dimensions recorded in the text are apparent, measured on the photomosaics. Special attention was given to the tracing of irregular and discontinuous surfaces, without assuming planar geometry or continuity across the outcrop. Examination of the surfaces focused on their erosional or non-erosional nature, truncation of older by younger surfaces, surface style (sub-planar to wavy, concave- or convex-up), and apparent inclination. Varied line weights were later applied to the surfaces to denote their relative importance in the alluvial architecture, as judged by their extent, prominence of erosion, and the lithological contrast across them (e.g., sandstone on mudstone remnants). Although no surface hierarchy was assumed *a priori*, the surfaces were later interpreted in relation to the sediment bodies that they bound (e.g., channel bases, bar tops, increments of bar accretion). Unexposed, poorly exposed, and vegetated areas were mapped to indicate areas of uncertainty, and major fractures and fallen blocks were noted to ensure that structural artifacts were not misidentified as sedimentary features.

A standard set of facies (recurring sediment types) and facies successions were identified in the basal, accessible few meters of the Swartberg member outcrop (–30.419108°, 26.259319°), as well as from bedset appearance at high resolution on the drone images. Facies codes are based on, or modified from, Miall (1978). Resolution was inadequate to note bioturbation, small fossils, and subtle sedimentary features. Subsequently, we identified what we term *remote outcrop facies* (ROFs) in the inaccessible cliff face. These facies are analogous in some respects to GPR radar facies for modern rivers, which are identified on the basis of reflector amplitude, frequency, and continuity, generating mappable 3-D units with reflections that differ in character from those of adjacent units (Huggenberger 1993). Remote outcrop facies are characterized by their sedimentary structures (where known), the style and continuity of stratal surfaces, the apparent inclination of the strata, and the resistant or recessive nature of the outcrop. Their identification was hampered where rock falls had left sheer, unweathered surfaces with cryptic features. Modern GPR studies are usually conducted across known surface morphology, testing stratification along and across flow directions to assess accretion directions (upflow, downflow, lateral). However, as paleocurrent measurements could not be collected for the inaccessible cliff, stratification styles could not be assessed along pre-determined directions.

For seven rectangular 2-D panels in the S–N face, we estimated the areal proportions of the remote outcrop facies. Facies areas were outlined and color-coded in CorelDraw and then exported as JPEG images. We then calculated the relative pixel fractions in the panels using an R script. The panels represent $\sim$ 31% of the channel-belt outcrop, excluding dikes. Much of the remaining outcrop area was unsuitable for analysis due to small or tapering exposures, partial vegetation cover, and distortion around dikes and sills; we estimate that our analysis covers about half of the suitable exposure. Several studies in modern rivers have employed a similar, quantitative analysis of radar facies (e.g., Horn et al. 2012a).

The remote outcrop facies were attributed to one or more *geomorphic units*, comparable to *architectural elements* (Allen 1983; Miall 1996), *macroscale forms* (Bridge 1993), and *geomorphic elements* (Horn et al. 2012a). The geomorphic units were assigned lower-case codes. In modern river systems, geomorphic units are defined as mappable landforms with distinctive geometry, sedimentary features, and bounding surfaces (Fryirs and Brierley 2018), and they constitute the "building blocks" of alluvial systems, fitting together to generate a reach-scale sediment body (Wheaton et al. 2015; Fryirs and Brierley 2018). The identification of units is conditioned by five characteristics: vertical position or formative flow stage relative to the channel bed; planform; unit type (e.g., bars, depressions); type and density of associated vegetation; and bed-material texture and other sedimentological features. Most of these aspects must be inferred for the present study, commonly leading to multiple interpretations. Terminology for architectural components is based on Miall (1996), Holbrook (2001), Gibling (2006), and Gibling et al. (in press). Broad criteria for identifying fluvial styles are set out in Table 2, with selected references for modern analogues.

A total of 269 thickness measurements were collected for channel bodies, facies successions, and remote outcrop facies. They were plotted as box-and-whisker diagrams that record the mean, the standard deviation, and the thickness range. Thickness data were used to assess channel and hydraulic parameters based on equations applicable to lithified fluvial strata, drawing on information from $>$ 4000 modern rivers (Long 2021). The equations rely on estimates of average bankfull channel depth (*dbf*, the average depth of a river across its full width), from which bankfull width, bankfull discharge, and drainage area can be estimated. The results are subject to much uncertainty, especially when estimating discharge and drainage area, and equations that employ several calculated parameters have cumulative errors (Long 2021). Average bankfull depth for individual channel bodies was calculated from thickness estimates that approximate maximum channel depth (d_{max}), subject to a correction factor for decompaction. This factor should ideally be based on thin-section analysis of diagenetic history, but because only a few meters of the basal strata could be accessed, a 10% correction factor (Cf) was applied as a 1.1$\times$ expansion, based on packing experiments (Ethridge and Schumm 1978):

$$d_{max} = \text{story thickness} \times \text{Cf}$$

Average bankfull depth (d_{bf}) was calculated as

$$d_{bf} = 0.6095 \times d_{max0.973} (r^2 = 0.87)$$

Bankfull width (w_{bf}) for channels with sinuosity $<$ 1.3 was calculated as

$$w_{bf} = 16.293 \times d_{max1.198} (r^2 = 0.63)$$

Bankfull discharge (Q_{bf}) was calculated as

$$Q_{bf} = 17.359 \times d_{max1.270} (r^2 = 0.66)$$

Drainage basin area (DA) was calculated as:

$$DA = 241 \times d_{bf2.17} (r^2 = 0.56)$$

Measured Sections

Gastaldo et al. (2019a, their Fig. 5) developed a stratigraphic framework across the Bethel and Heldenmoed farms, with eight measured sections of various thickness and paleomagnetic data available for three sections. The sections were correlated using prominent sandstone benches exposed along the S–N and E–W mountainsides in the lower part of Swartberg Koppie, waypointed every 40 to 80 m depending on physical conditions (WSG84 standard; Supplemental Material S1). Two additional sections were measured in 3/2019 and 8/2022 to determine the thickness of the succession down to the base of the Swartberg member (Supplemental Material S1). Measurements were made with a Jacob's staff equipped

TABLE 2.—*General description of alluvial systems referred to in the text.*

Fluvial Style	Key Features	Modern River Examples
Meandering channels	Sinuosity (channel length divided by valley length) > 1.5, with relatively strong banks, bank-attached bars prominent and mid-channel bars uncommon.	Wabash, USA: Jackson 1976; Beatton, Canada: Nanson 1980.
Braided channels	Single-thread at high stage when the bars are underwater. Multi-thread at low stage when flow divides around mid-channel bars of unvegetated gravel and sand, which show downstream, lateral, and oblique accretion. Deeper scour at channel confluences, and bank-attached bars common. Sinuosity of high-stage channel variable but generally low.	Sagavanirktok, Alaska: Lunt and Bridge 2004. South Saskatchewan, Canada: Sambrook Smith et al. 2006; Lunt et al. 2013; Parker et al. 2013. Platte, Nebraska: Horn et al. 2012a, 2012b. Kicking Horse, Canada: Cyples et al. 2020.
Low-sinuosity channels	Sinuosity < 1.5, transitional between braided and meandering. Channels show relatively straight reaches between bank-attached bars, with some mid-channel bars.	Calamus, Nebraska: Bridge et al. 1986, 1998.
Ephemeral rivers	Display infrequent, short-lived floods with high discharge after occasional or seasonal rainfalls, and prolonged dry periods. Commonly contain bedload sheets laid down during high-strength flow. Show meandering, braided and low-sinuosity planforms.	Ghash, Sudan: Abdullatif 1989. Ethiopian rivers: Billi 2008. Luni, India: Carling and Leclair 2019.
Valleys	Conduits that are larger than the channel systems they contain. Margins confined by bedrock or alluvium, influencing fluvial style and planform.	Gibling et al. 2011; Fryirs and Brierley 2018.

with an Abney level (see methods in Gastaldo et al. 2021). During both field seasons, representative calcite-cemented pedogenic nodules from available paleosols and intraformational conglomerate were collected.

U–Pb Isotopic Analysis of Pedogenic Carbonate Nodules

Calcite-cemented pedogenic nodules were sectioned and polished to generate a flat surface. Individual nodule surfaces were analyzed for U-Pb isotopic composition at the University of Toronto using an Agilent 7900 ICPMS and an NWR193 excimer laser system. U-Pb data (^{238}U, ^{206}Pb, and ^{207}Pb) were collected using scan-lines over individual nodules, resulting in hundreds of cycle data per line following the methodology of Davis and Rochín-Bañaga (2021). Analytical data are available in Supplemental Materials S4 to S8.

Each scan-line analysis, 4–5 mm long, was pre-ablated at a fast scan rate, 200 μm/s, and high frequency, 20 Hz, using a larger diameter beam to remove surface contamination. U-Pb line analyses were conducted with a laser frequency of 193 nm, fluence of ~ 4.5 J/cm^2, diameter beam of 120 μm, and frequency of 10 Hz at a rate of 15 μm/s. Baselines were accumulated on each scan-line for 20 seconds before opening the laser. LA-ICPMS parameters for U-Pb analyses are found in Supplemental Material S7.

Two standards, the Glass standard NIST612 and Duff Brown Tank, were used to correct for mass-and-oxide elemental fractionation bias. The uncertainty of our ^{238}U–^{206}Pb ages includes measurement errors in mass signals from the sample, NIST612, and Duff Brown Tank calcite-standard measurements. The Duff Brown Tank standard was used as a matrix-matched reference. The age of the Duff Brown Tank was measured here at 64.1 ± 1.4 Ma (2s; MSWD = 0.87) which agrees with its true age of 64.04 ± 0.67 Ma by isotope dilution (Hill et al. 2016). During each analytical session, another calcite material with a known age, determined by isotope dilution (Walnut Canyon standard of 254.4 ± 6.4 Ma; Roberts et al. 2017), was measured as a secondary standard to check on accuracy; the Walnut Canyon standard gave an age of 255 ± 3 Ma (2s; MSWD = 2.3).

U-Pb regression was carried out using a Bayesian statistical program (UtilChron) that regresses mass-count data in a 3-D signal space (Davis and Rochín-Bañaga 2021). Calcite minerals usually contain significant common Pb, as well as radiogenic Pb. Hence, age determinations are based on defining a mixing line in isotope-ratio space. Intersection with the concordia curve (showing radioactive equilibrium at a given age) provides the age of the radiogenic component, and its Y (^{207}Pb/^{206}Pb) axis intercept on the Tera-Wasserburg plot gives the isotopic composition of the initial common Pb component (denoted PbC). Mixing lines are defined using a data set, or multiple data sets, from samples with similar age and PbC. Data were processed as single or small-number average measurement cycles to exploit the maximum U over common Pb heterogenicity in the samples, giving the maximum spread along the mixing line. U-Pb data are plotted and regressed using Tera-Wasserburg (inverse) concordia diagrams, where the age represents the intersection of the best-fit line with the concordia curve and PbC is given by its Y axis intercept. Data sets consist of hundreds of measurements; as such, error ellipses are not shown but are taken into account in the calculations.

RESULTS AND ANALYSIS

Overview of Cliff Architecture, Paleoflow, and Definitions

The Swartberg member is 45 m thick (Fig. 4A) and contains six large-scale units that can be identified in both S–N and E–W faces (Figs. 2B, 3B). A basal mudstone-dominated unit with lensoid sandstone bodies is only partially exposed, overlying poorly exposed reddish gray and greenish gray mudstone in the slopes below (Supplemental Material S1). Above, three thicker units consist predominantly of sandstone with minor fine-grained lenses, separated by two additional mudstone-dominated intervals. The upper surface of the topmost thick sandstone unit forms the top of the outcrop at ~ 1565 m. The Swartberg member may attain a greater overall thickness, but vegetation obscures the extent of the resistant benches in Google Earth images of the southwest side of the koppie, which was inaccessible during field work.

The three mudstone-rich intervals (Fine Intervals A, B, and C) comprise small fluvial channel bodies and green-gray laminated fines, interpreted as *fluvio-lacustrine deposits*. The three sandstone-dominated units (A to C) are interpreted as *channel belts*, occupying shallow valleys, and defined in preserved strata as the amalgamated deposits of a channel system that developed through time. The channel belts are interpreted as braided-river systems based on cross sections with inferred braid bars and adjacent channels (Bridge 2003). For modern braided rivers, Lunt and Bridge

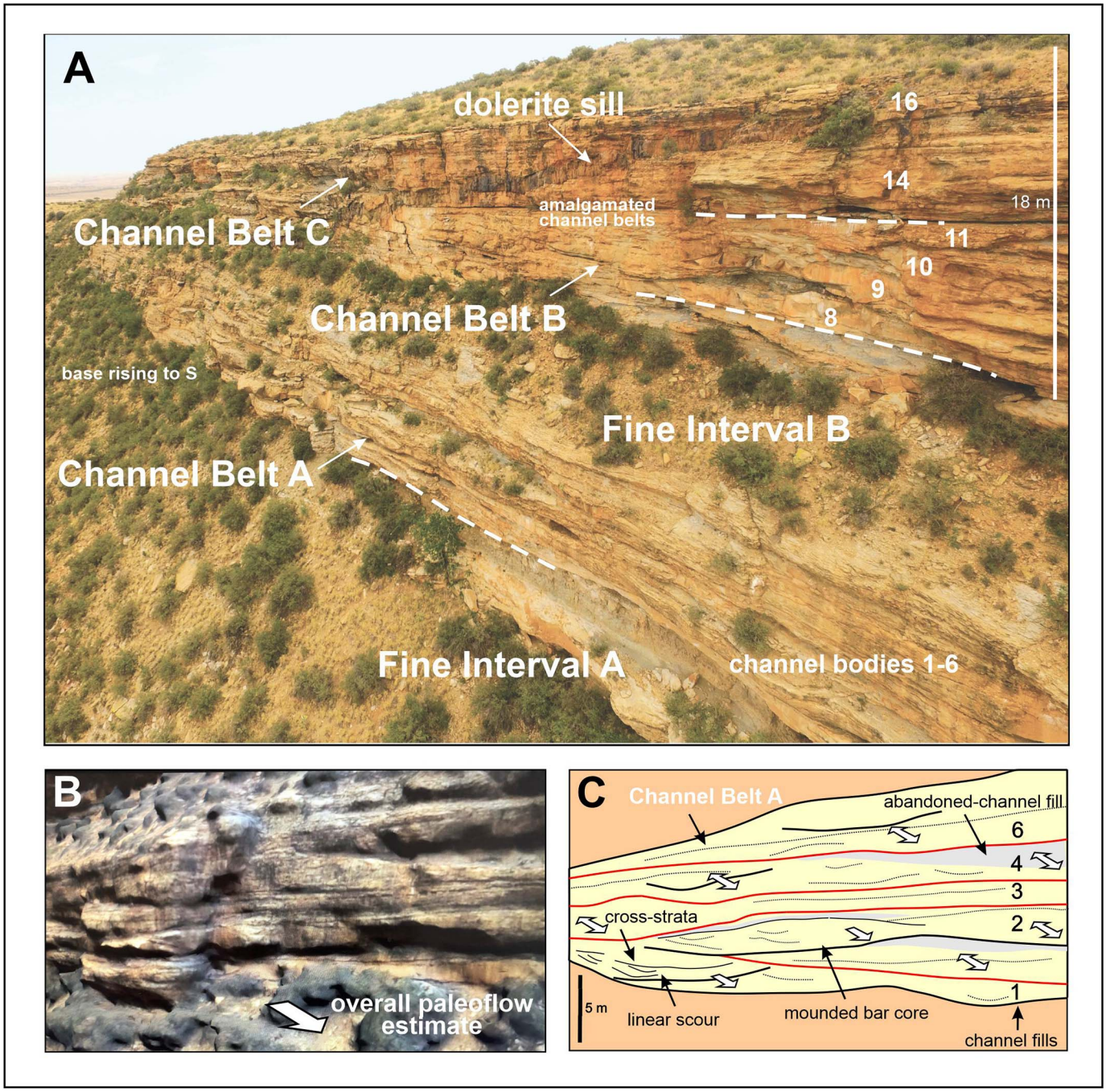

FIG. 4.—Swartberg Koppie outcrop. **A)** Oblique view from a drone image showing the three channel belts, component channel bodies, fine intervals, and a dolerite intrusion. **B)** Uninterpreted and **C)** interpreted view of the corner of the 3-D model indicating inferred northward paleoflow direction (obliquely to the right).

(2004) defined the channel belt as the extent of flow during bankfull flood events (the "active channel belt" of Horn et al. 2012a). This definition covers active and partially abandoned channels, as well as simple and compound bars and bar assemblages.

The channel belts each comprise three to seven *channel bodies* that are vertically stacked or locally inset, underlain by prominent erosional surfaces. Channel bodies are also referred to as *stories* (Friend et al. 1979). The term *channel fill* is used here to denote fluvial-channel sediments in general and is not restricted to the filling of a discrete, unmodified channel cut. The channel bodies contain numerous *bars*, defined as within-channel depositional features with a length proportional to the width of the adjacent channel and a height comparable to the bankfull channel depth (Lunt and Bridge 2004).

Although field measurements were not possible, several lines of evidence collectively indicate a general northward paleoflow direction along the S–N face (roughly longitudinal section), emerging in the E–W face (roughly transverse section). Channel bodies are mainly planar and continuous in the S–N face but are more lensoid in the E–W face (Figs. 2, 3). Inclined bar-accretion surfaces show apparent northward dips in 29 instances and apparent southward dips in three instances, in accord with the predominantly

TABLE 3.—*Facies identified in the Swartberg Koppie outcrop. ABS, accessible basal strata; DI, drone images.*

Facies	Description from Drone Images and Outcrop	Interpretation	Distribution
Gravel lag (Gl)	Scattered mudstone intraclasts a few cm in length on many erosion surfaces.	Reworked pedogenic and lacustrine mud.	Identified in ABS and DI for Channel Belt A.
Trough cross-bedded sandstone (St)	Suites of concave-up surfaces with 0.2 to 0.9 m relief, average 0.4 m. Surfaces symmetric or asymmetric with inclined surfaces (foresets) downlapping onto them locally.	3-D dunes formed under subcritical flow conditions.	Predominant bedform identified in DI for all channel belts.
Planar cross-bedded sandstone (Sp)	Isolated or grouped cross-sets on planar surfaces, a few meters to 50 m in apparent extent, 0.3 to 2.2 m thick, average 0.9 m. Foresets sub-planar with apparent dips up to 20°.	2-D dunes formed under subcritical flow conditions.	Identified in DI for all channel belts.
Ripple cross-laminated sandstone (Sr)	Thin (dm scale) bedsets with wavy surfaces, locally resting on concave-up surfaces. Form planar units and occupy scours and cross-beds troughs.	Ripples formed under subcritical flow conditions.	Identified in ABS, difficult to identify in DI.
Plane-laminated sandstone (Sh)	Thin (dm-scale) bedsets with planar surfaces that are horizontal or gently dipping.	Plane beds formed under transcritical flow conditions.	Identified in ABS, and locally in DI on weathered surfaces.
Scour and mound sandstone (Sac)	Low-amplitude mesoforms with dm-scale relief (0.6 to 1.0 m, average 0.9 m) and form-concordant internal strata, locally associated with and built over shallow scours.	Provisional interpretation as high-flow strength bedforms, including antidunes, formed under supercritical flow conditions.	Present in DI with flat-bedded strata along top surface of Channel Belt C.
Massive sandstone (Sm)	Beds of cm to m scale, apparently structureless in normally weathered outcrop faces (broken, unweathered surfaces may appear massive).	Rapid deposition from flows or sand collapse, or due to loss of structure from dewatering.	Identified in ABS, prominent with facies Fl below Channel Belt A, and in DI for all channel belts.
Scour-fill sandstone (Ss)	Concave-up, isolated scour fills of dm to meter scale that are not part of St suites.	Fills of discrete scours of varying scale.	Prominent in ABS and in DI for all channel belts.
Laminated mudstone (Fl)	Lenses dm to m thick and tens of meters in extent, with lamination locally contorted. Present in fine intervals and within channel belts, commonly recessively weathered.	Deposition from standing water in lakes and abandoned channels. Contorted units are probably slumps.	Prominent where interstratified with facies Sm in ABS below Channel Belt A, and in DI for all channel belts.
Massive mudstone (Fm)	Lenses in channel belts, lacking visible stratification. Recessive weathering, appear brown or gray.	Desiccation, bioturbation, root activity, and pedogenesis, with vegetation-induced sedimentary structures (VISS).	Present in ABS below Channel Belt A and in DI for all channel belts.

downstream dip of accretion surfaces in many GPR profiles of sandbed rivers (e.g., Calamus River: Bridge et al. 1998). Where trough cross-sets can be discerned, apparent dips are northward. For the outcrop corner (Figs. 4B, C), rotating the 3-D model to examine the strata from various angles confirmed the north–south orientation of linear, scour-based sediment bodies and the northward dip of cross-beds and larger-scale accretion sets. Additionally, as discussed below, large-scale bedsets in Channel Bodies 9 to 11 show northward depositional dips in the S–N face, and channel belts and bodies taper out westward in the E–W face, indicative of orientations along- and across-paleoflow, respectively.

Facies and Facies Successions

Ten sedimentary facies were identified at the outcrop base and in drone images (Table 3; Figs. 5, 6). A similar range of facies was identified in other studies of the Katberg Formation (Stavrakis 1980; Groenewald 1996; Neveling 2004) and other formations in the Karoo Basin (e.g., Gulliford et al. 2014; Wilson et al. 2014; Bordy and Paiva 2021). The coarser beds are fine- to very fine-grained sand, with admixtures of silt but relatively little coarser-grained sediment.

Thin units with pebble-size mudstone intraclasts are identified as *gravel lag* (Gl), overlying prominent erosional surfaces in the lower part of Channel Body A (Figs. 5A, C, 6A). *Trough cross-bedded sandstone* (St) is characterized by grouped trough forms that range in relief from 0.2 to 0.9 m, averaging 0.4 m ($n = 25$); individual cross-beds were difficult to resolve in the troughs, but the strata are interpreted as cosets of trough cross-beds. Cross-sets of smaller size were difficult to resolve. Trough cross-beds are typically preserved to about one third of the original dune height (Leclair and Bridge 2001), and many of the original dunes may have been > 1 m high. *Planar cross-bedded sandstone* (Sp) comprises isolated or grouped cross sets that rest on planar surfaces. Individual cross-sets are up to 2.2 m thick, average 0.9 m ($n = 21$), with apparent downdip extents of several meters (Fig. 6B) to 50 m. *Ripple cross-laminated sandstone* (Sr) was difficult to identify and may be more abundant than our data implies.

Plane-bedded sandstone (Sh) comprises sandstone bedsets with even lamination (Fig. 5D). *Scour-and-mound sandstone* (Sac; Walker and Holbrook 2022) is present in the topmost beds of Channel Belt C, where a series of sandstone mounds, with form-concordant internal stratification and quasi-regular spacing, is locally associated with facies Sh (Fig. 6B). The relief of the mounds ranges from 0.6 to 1.0 m, averaging 0.9 m ($n = 11$).

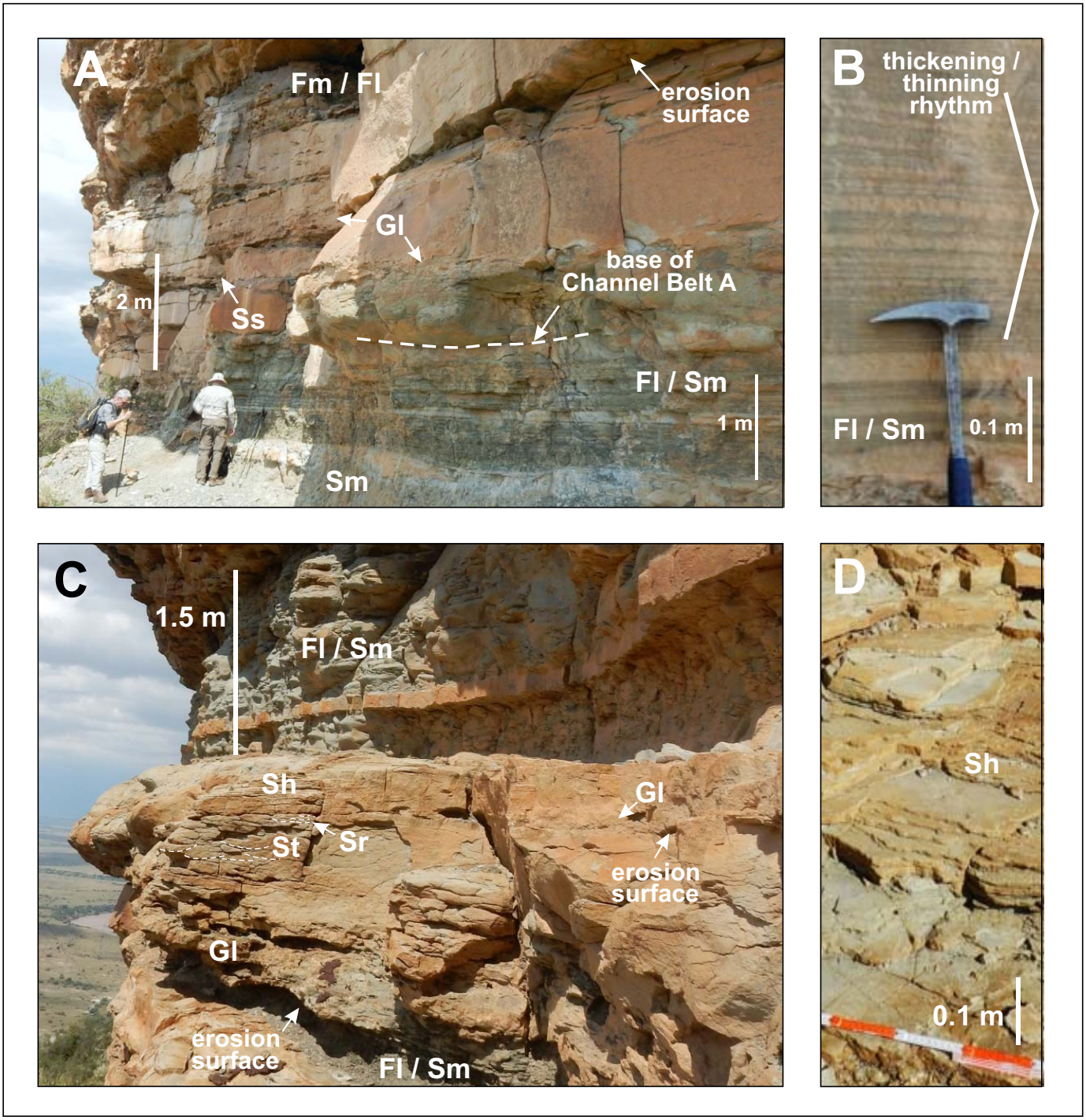

FIG. 5.—Facies in outcrop at the base of the Swartberg member, representing the base of Channel Belt A and underlying fluvio-lacustrine strata of Fine Interval A. See Table 3 for facies codes and details.

These features are provisionally interpreted as high-flow-strength bedforms, probably antidunes, formed under shallow, supercritical flows.

Massive sandstone (Sm) lacks obvious stratification. Most occurrences are interbedded with mudstone and comprise discrete layers with abrupt bases and tops, although some fine upward from sand to mud. Thickening/thinning rhythms are present in places (Fig. 5B). A thicker bed of facies Sm occupies a shallow scour at the base of the cliff (Fig. 5A). *Scour-fill sandstone* (Ss) overlies solitary, concave-up erosional surfaces of decimeter scale (Fig. 6A–C); their solitary nature distinguishes them from grouped trough forms of facies St.

Laminated mudstone (Fl) is commonly interstratified with massive sandstone and is well exposed at the outcrop base (Fig. 5A, B). *Massive mudstone* (Fm) is present locally as units $>$ 1 m thick, commonly within scour hollows.

Meter-scale facies successions in the basal strata commence with erosional surfaces overlain by facies Gl, St, and Sh with facies Sr

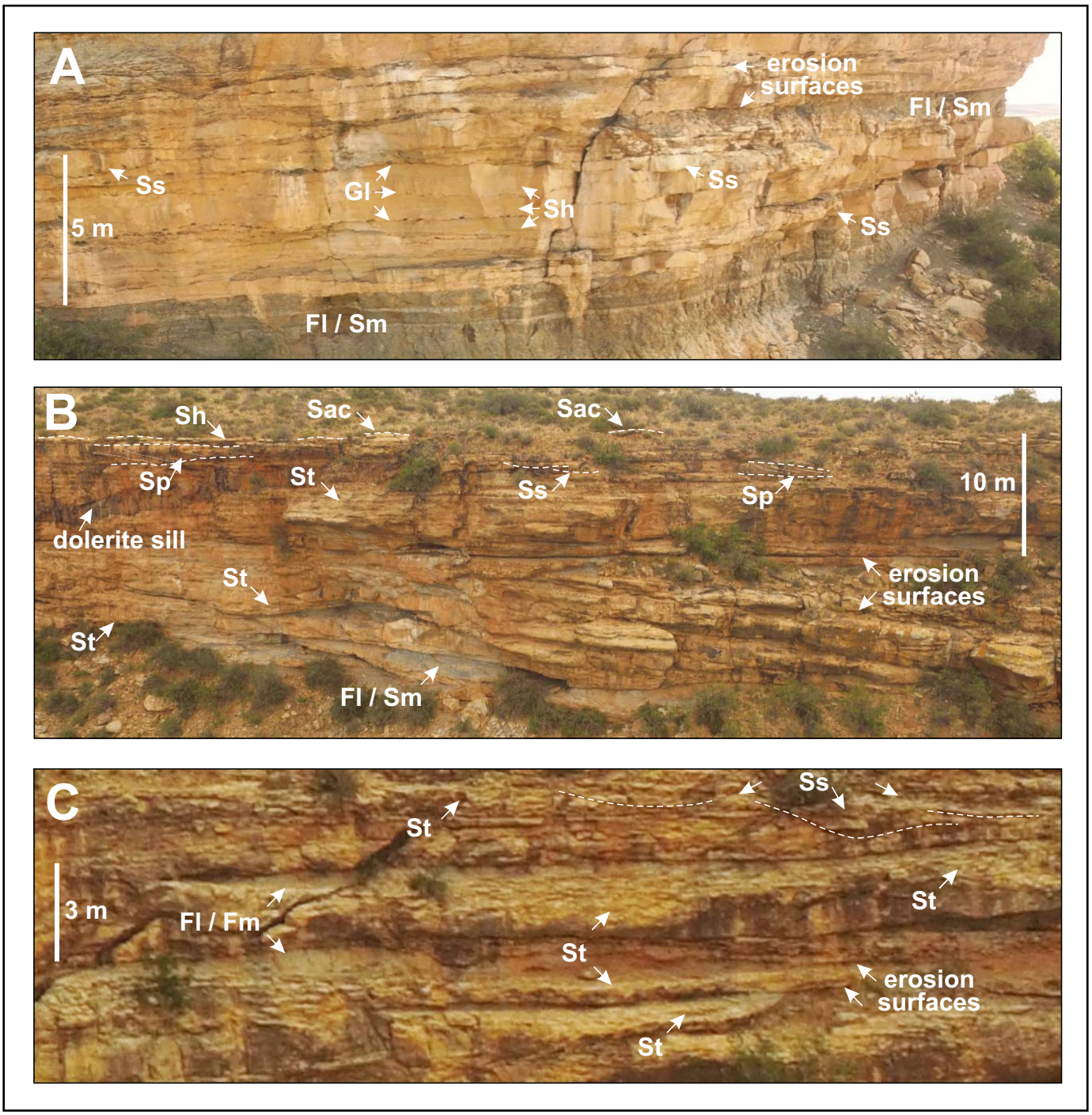

FIG. 6.—Facies identified in drone images of the Swartberg member. **A)** and **C)** represent Channel Belt A, and **B)** represents Channel Belts B and C. Note lenticular mudstone units (facies Fl and Fm) in abandoned channels. See Table 3 for facies codes and details.

locally, capped abruptly by lensoid dm-scale bedsets of facies Fl, Fm, and Sm (Fig. 5C). They are interpreted as shallowing-upward successions in small channels.

Remote Outcrop Facies and Geomorphic Units

Seven remote outcrop facies (ROF, Table 4) are illustrated at a comparable scale in Figure 7, provisionally linked to geomorphic units (Figs. 8–11) through the identification of key surfaces (Table 5). Dips and horizontal distances reported below are apparent and are not corrected for paleoflow. Thickness data for some ROF are illustrated in Figure 12A.

Flat-Lying Strata (ROF 1).—ROF 1 is present in all the channel belts as horizontal to slightly inclined bedsets up to 5 m thick that extend for tens of meters (Fig. 11A). Bed surfaces are variably planar, undular, trough and wavy, and the strata comprise trough cross-stratification, planar stratification, and

TABLE 4.—*Remote outcrop facies and inferred geomorphic units, identified in drone images. See Table 3 for facies codes and descriptions.*

Remote Outcrop Facies	Description from Drone Images on S-N cliff	Dimensions	Geomorphic Units
1) Flat-lying strata	Extensive bedsets with flat-lying to gently dipping internal surfaces that are concordant or erosional. Undular and trough-shaped forms prominent (facies St), with probable Sh, Sac, and Sr locally.	From dm to ~ 5 m thick, and tens of m in apparent extent.	**Sand sheets (ss)** with 3-D dunes and other bedforms. In channels, part of unit and mid-channel bars, and on bar tops. Some may be longitudinal sections of channel scours.
2) Strata within concave-up surfaces	A) Concave-up erosional surfaces overlain by flat-lying and gently inclined strata. Fill is commonly form-concordant with underlying surface and includes trough-shaped forms (facies St).	Relief up to 3.2 m, average 1.7 m (n = 23), with apparent widths of a few m to tens of m.	**Channel scours (cs)**, probably linear in 3-D form, that represent primary channels, secondary channels, and confluence scours.
	B) Concave-up erosional surfaces overlain by flat-lying strata. Incised into top of mounded macroform.	Decimeters thick and apparent extent up to 10 m.	**Bartop channels or hollows (btc)**, probably linear or elongate.
3) High-angle inclined strata at scour margins	A) Inclined bedsets with apparent dips < 15°, oriented sub-parallel to a discrete scour margin. Associated with flat-lying or gently dipping bedsets, at a level below top of scour margin.	Up to 3.2 m thick, average 2 m (n = 8), and apparent extent of up to 5–10 m.	**Point bars (pb), alternate bars (ab), or side bars (sb)**, formed at the migrating margins of bank-attached bars. Associated flat-lying bedsets are **benches (bc)**.
	B) Thin, steeply inclined bedsets, apparent dips of 23–25°, border the upper part of a discrete scour margin.	Up to 2 m thick, and a few m in apparent extent.	**Accretionary banks (ab)**, with inclined bedsets on steeper parts of scoured margin.
4) High-angle inclined strata with flat-lying bedsets	Solitary to stacked planar cross-sets (Sp) with planar lower surfaces and planar to slightly convex-up upper surfaces. Foresets relatively planar, apparent dips of 8–21°. Thicker than trough cross-sets (St). Slipface is locally preserved at the downflow margin. Inclined scoured surfaces (reactivation surfaces) in the upper part of one larger example. Locally occupy scours.	Up to 1.8 m thick, average 0.9 m (n = 21), with apparent extent of a few m, up to 10 m. One prominent example is 2.2 m thick with an apparent downdip extent of 50 m.	Slip-face component of **Unit bars (ub)** in mid-channel settings or as components of larger bars.
5) Mounded macroforms	Mounded accumulations with no apparent link to channel margins. Bases planar or overlie concave-up scours. Most contain form-concordant inclined strata, especially apparent at the tops, or discrete sets of systematically dipping strata (Sp sets) with dips of up to 10°. Some mounds comprise flat-lying beds.	Up to 2.8 m thick, average 1.7 m (n = 73), with apparent extent of up to 10 m.	**Mounded cores of mid-channel bars (mcb).** Linear components of large compound bars, in association with other remote outcrop facies. Probable longitudinal orientation with respect to paleoflow.
6) Vegetation-influenced strata	Mounded to flat-topped strata associated with upright trees, tree positions before decay or windthrow, or log accumulations. Strata planar to form-concordant, locally inclined towards the vegetation on one or both sides (centroclinal cross-stratification). Some strata overlie concave-up scours alongside or above the vegetation. A few lenses to sheets of facies Fm, structureless and brown colour, contain V-shaped features that mark former trees.	Up to 2.5 m thick, average 1.8 m (n = 4), with apparent extent of up to 4 m. Relief on scours up to 1 m. Sheets of Fm are up to 1.5 m thick.	**Forced mid-channel bars and pools (fmb, fmp).** Vegetation shadows and scours formed where vegetation provided obstacles. Not apparently associated with channel margins but may adjoin vegetated banks. **Floodplains (fp)**, as vegetated muddy remnants within channel belts, possibly part of vegetated islands.
7) Interbedded muddy and sandy strata	A) Hollows filled with fine-grained facies (Fl and Fm, locally contorted) and thin sandstone beds (Sm). Bases are erosional or concordant on underlying sandstone. Fills flat-lying or gently concave-up.	Fills up to 2.5 m thick, average 0.8 m (n = 66), apparent extent up to tens of m. Fills thicker in E–W (near-transverse) face.	**Abandoned channel fills (abc),** representing primary (main) channels and secondary channels within the channel belts.
	B) Sheet-like bedsets of facies Fl, Fm, and Sm, overlying or associated with lensoid channel bodies.	Up to 3 m thick, apparent extent up to tens of m.	**Floodplain lakes (fl)** associated with distributary channels in fine intervals.

ripple cross-lamination (St, Sh, Sr). Scour-and-mound stratification (Sac) is present in ROF 1 at the top of Channel Belt C.

The facies is attributed to *sand sheets* (ss), generated from 3-D dunes with contributions from other bedforms.

Strata in Concave-Up Surfaces (ROF 2).—ROF 2 comprises flat-lying to gently inclined bedsets, up to 3.2 m thick, that onlap and overlap an underlying erosional surface, and are prominent in all channel belts (Fig. 11B). The surfaces range from strongly concave-up to gentle scours

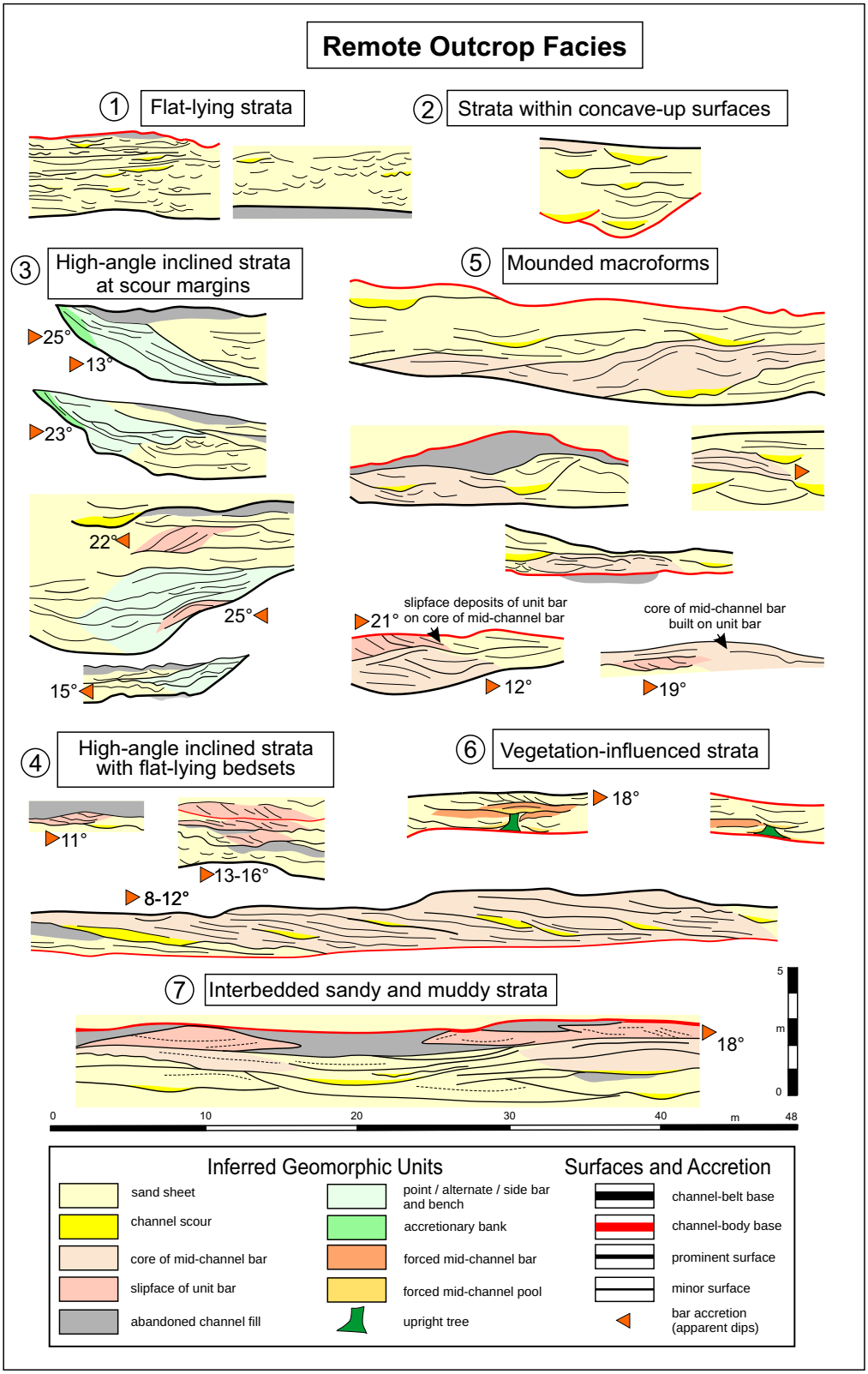

FIG. 7.—Seven remote outcrop facies and inferred geomorphic units in the three channel belts, illustrated in line drawings. All are at comparable scales, with 1.5 times vertical exaggeration. See Table 3 for facies codes and details, and Table 4 for details of the remote outcrop facies.

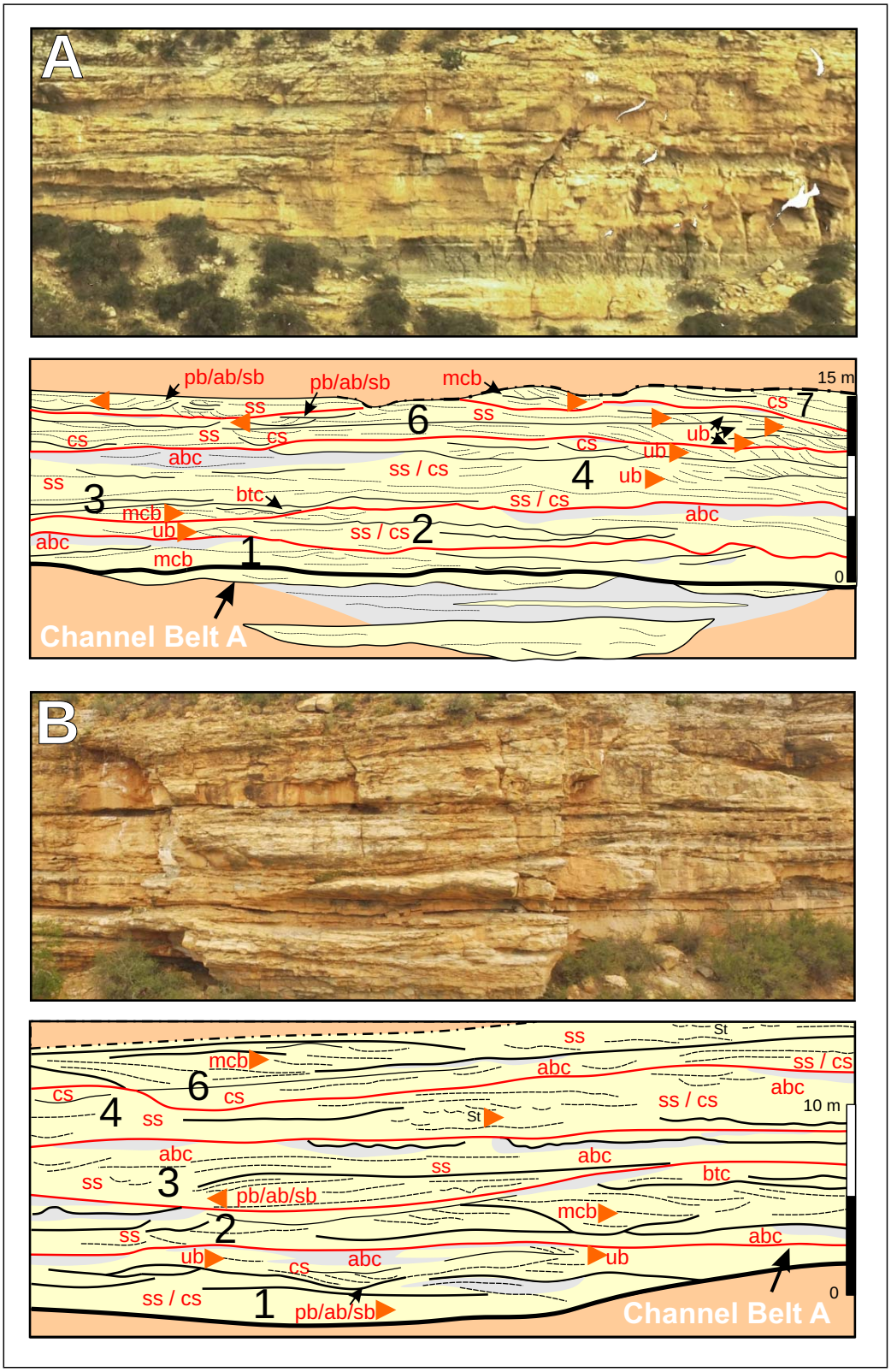

FIG. 8.—Architecture of Channel Belt A, showing channel belt, component channel bodies, geomorphic units, and apparent accretion directions. Note the presence of bar components as unit bars (ub), cores of mid-channel bars (mcb) with bartop channels (btc), and inclined bedsets attributed to point, alternate, or side bars (pb/ab/sb). Apparent accretion directions are mainly to the right (north). Legend in Figure 9.

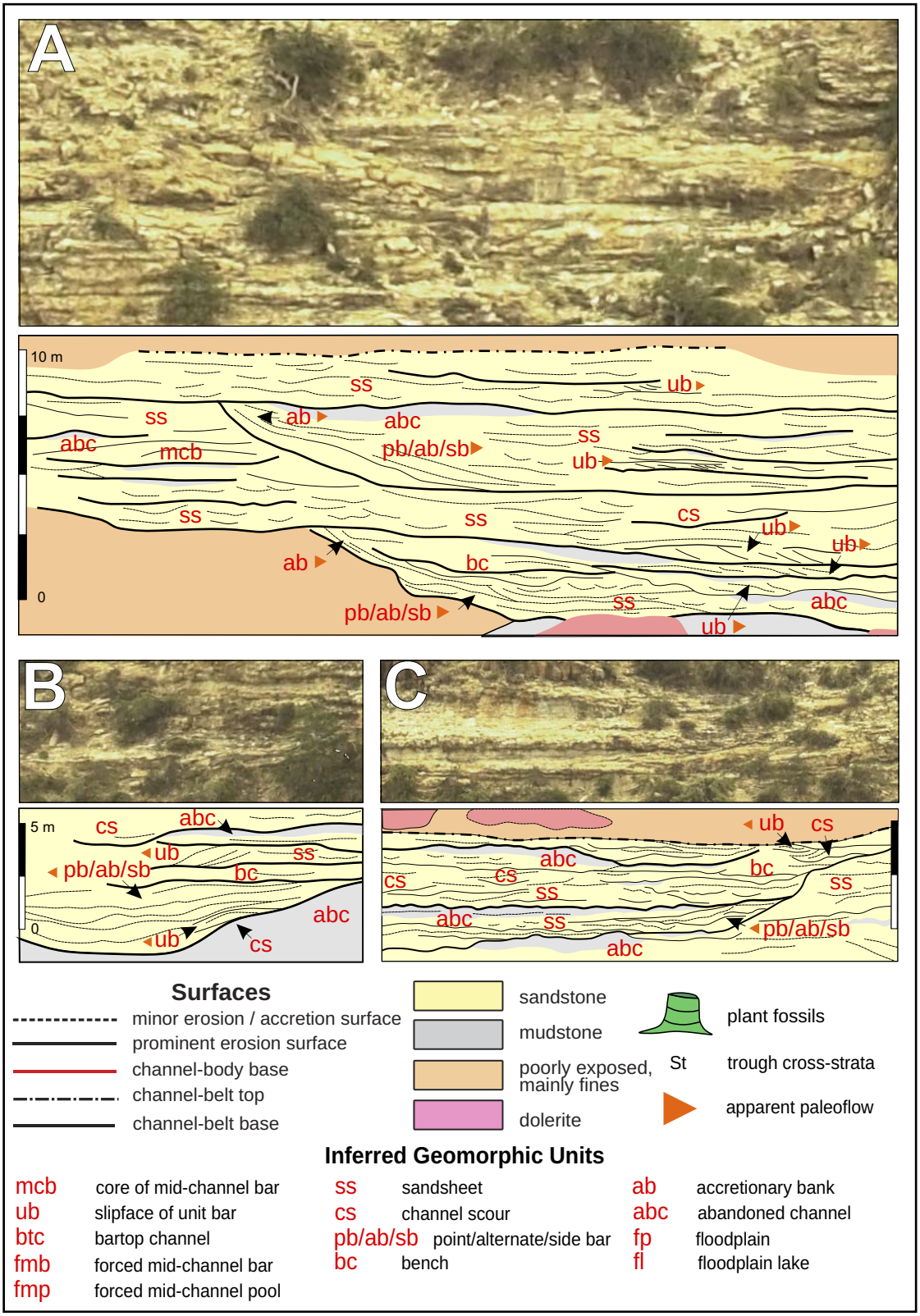

FIG. 9.—Bank-attached bars in the southern, thinner part of Channel Belt A. Note that the bars occupy discrete channels cut into abandoned-channel fills or underlying fine intervals. Inclined accretion surfaces can be traced for only a few meters, passing laterally into sand sheets, and they are associated with benches and accretionary-bank deposits that mantle the channel margin. A distinction cannot readily be drawn between point, alternate, and side bars without a fuller 3-D exposure.

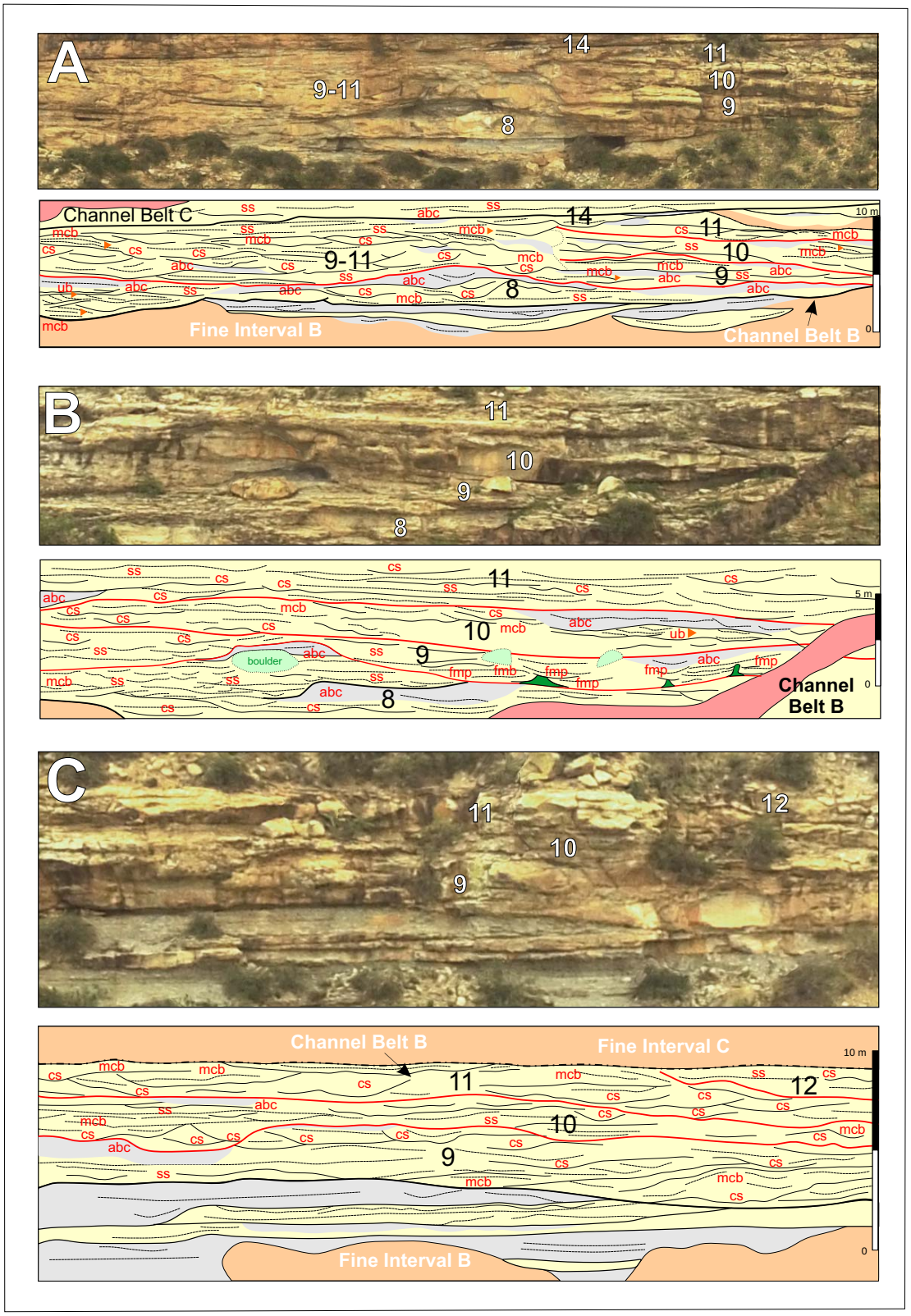

FIG. 10.—Architecture of Channel Belt B, with numerous bar components as unit bars (ub), cores of mid-channel bars (mcb), many of which built up over scours. They are associated with sand sheets (ss) and channel scours (cs). Note the complex suite of channel bodies, which are variably extensive or inset in the plane of the cliff face. Legend in Figure 9.

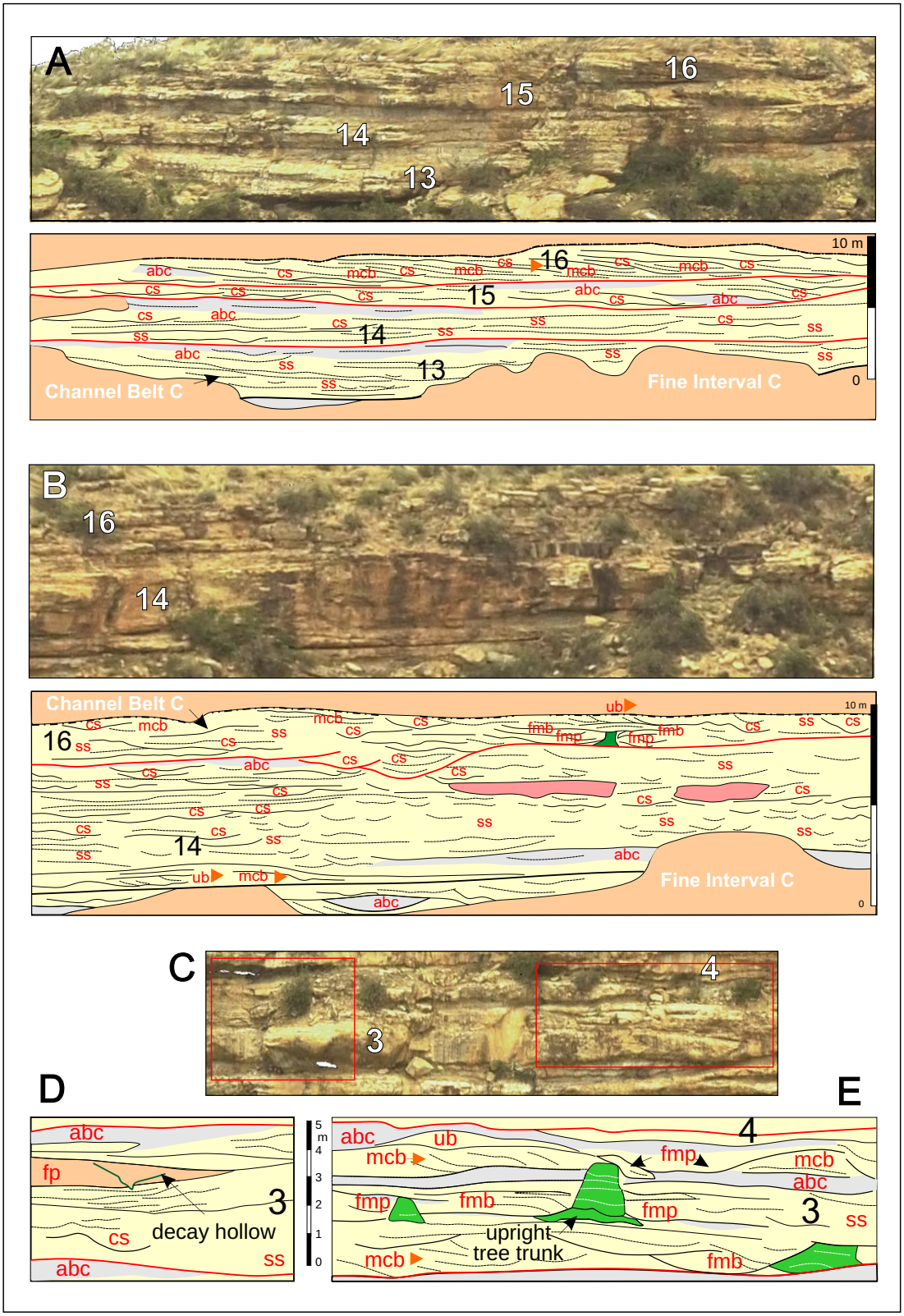

FIG. 11.—Channel-belt architecture. **A**, **B)** Channel Belt C, with a predominance of sand sheets (ss) and channel scours (cs). Mid-channel bars (mcb) are present locally, with an extensive barform with inclined accretion surfaces at the top of the channel belt in Part A. A set of forced bars and pools is present in Part B, associated with vegetation. **C)** Forced mid-channel bars and pools in Channel Belt A, formed by scour and deposition around upright tree trunks or log accumulations. The decay hollow in Part D is a V-shaped depression in a mudstone unit, marking the former position of a trunk that was lost to decay or windthrow (Rygel et al. 2004). The trunk at lower right in Part E stands on a channel base, suggesting that the plant was established in a seasonally dry or abandoned channel. Legend in Figure 9.

TABLE 5.—*Stratification surfaces identified in drone images of the Swartberg Koppie outcrop.*

Surface	Description
Channel-belt base	Prominent throughgoing erosion surfaces that can be traced along the 500 m S–N extent of outcrop. Cut into fine intervals and locally into underlying channel belts. Surfaces are sub-planar, with relief of a few m. The base of Channel Belt A is incised more deeply in the northern area.
Channel-belt top	Top of the topmost channel fills below fine intervals, extending along the S–N outcrop. Surfaces are abrupt to gradational with finer beds above.
Channel base	Prominent erosion surfaces cut into underlying sandy channel fills and muddy abandoned-channel fills. Some surfaces can be traced over the 500 m S-N extent of outcrop, whereas others extend for tens to a few hundred m, cut out below overlying channel fills. Surfaces have a few m of relief and are sub-planar to gently inclined, locally with deeper scours.
Prominent erosion surface	Surfaces extend for tens of m. Some are sub-planar, others are concave-up and overlain by minor channel fills a few m thick.
Minor erosion and accretion surfaces	Sub-planar to gently dipping surfaces that extend for tens of m, with little or no evidence for erosion. Commonly bound bedsets and bedforms.
Macroform top	Sub-planar to convex-up surfaces with vertical relief of a few m and lateral extent of m to tens of m. Pass laterally into minor erosion or accretion surfaces and are locally scoured.
Macroform accretion surfaces	Inclined, convex-up, and concave-up surfaces within macroforms. Inclined surfaces are locally scoured (reactivation surfaces).

to flat-lying surfaces with scooped segments. Bedforms are difficult to identify but trough cross-stratification is visible locally.

The main subset (2A) is attributed to *channel scours* (cs) that represent primary or secondary channels or confluence scours where braid channels join. A minor subset (2B) is incised into the tops of mounded macroforms and is attributed to *bartop channels* or bartop hollows (btc).

High-Angle Inclined Strata at Scour Margins (ROF 3).—ROF 3 is characterized by dipping bedsets with up to 3.2 m of relief on individual surfaces and apparent dips of up to 15° (Fig. 9A–C). The surfaces appear irregular in cross section with some flat-lying segments, and they have modest apparent extents of up to 10 m, passing laterally into sand sheets (Fig. 9A, C).

The main subset (3A) is prominent in Channel Belt A and is attributed to bank-attached bars that may include *point bars* (pb) in high-sinuosity channels and *alternate bars* (ab) or *side bars* (sb) in low-sinuosity channels. Deciding between these options would require a fuller 3-D or planform exposure to explore channel sinuosity and bar disposition. Flat-lying segments are attributed to *benches* (bc) on the bar surfaces, developed at levels below the tops of the bordering scours. A minor subset (3B) comprises thin bedsets with steeper dips of up to 25°, mantling the upper parts of some scoured margins and passing downdip into facies 3A. The bedsets are attributed to *accretionary banks* (ab). The bar, bench, and bank deposits record deposition in stably positioned channels.

High-Angle Inclined Strata with Flat-Lying Bedsets (ROF 4).—ROF 4 comprises solitary or stacked planar cross-sets (facies Sp) up to 1.8 m thick, averaging 0.9 m, and is present in all channel belts. The cross-sets have apparent dips of up to 21° and apparent extents of up to 10 m (Fig. 8A, B), and they are considerably thicker than associated trough cross-beds (facies St). Most of the cross-sets rest on planar surfaces, but a few overlie scours. An especially prominent example at the top of Channel Belt C (Fig. 11A) shows a set of inclined strata 2.2 m thick and 50 m in apparent extent, with reactivation surfaces on the upper parts of some foresets.

The facies is interpreted as the slip-face component of bars, probably mainly *unit bars* (ub), which are widespread in modern sandbed rivers.

Mounded Macroforms with Inclined Strata (ROF 5).—Mounded macroforms of ROF 5 are prominent in all the channel belts and have no apparent connection with channel margins (e.g., Figs. 8B, 10A). The mounds rest on flat-lying surfaces or are built over scours, aggrading across the scour margins, and they are probably linear with an along-stream orientation (Fig. 4C). Mound stratification is flat-lying or mounded in concordance with the top surface, and some contain inclined sets with dips of up to 10°. The mounds average 1.7 m thick (73 examples) but are up to 2.8 m thick, with apparent extents of up to 10 m. In one case, a planar cross-set (ROF 4) stalled on the upflow side of a mound, generating a composite form 2.2 m thick (Fig. 7). In another case, a mound built over the top of a planar cross-set (Fig. 7).

ROF 5 is interpreted as the *mounded cores of mid-channel bars* (mcb), probably a component of compound bars. Some mounds may be remnants of sediment sheets that were scoured on two sides, but many modern river bars experience erosion along their margins.

Vegetation-Influenced Strata (ROF 6).—ROF 6 was identified in all three channel belts as mounded or flat-topped accumulations associated with features interpreted as upright trees or log stacks (Figs. 10B, 11B–E). The vegetation elements range from 0.4 to 2.5 m high (average 0.4 m) and taper upwards. Although at the limit of resolution in the drone images, one well exposed upright tree contains sediment layers that built up in a hollowed trunk (Fig. 11E). Sediment accumulations up to 2.5 m thick and 4 m in apparent extent built up over scours that bordered or formed above the vegetation elements. In some instances, inclined strata are present on one side of the vegetation element or dip inwards on both sides (centroclinal cross-stratification: Underwood and Lambert 1974). The vegetation elements are mainly preserved on flat-lying or inclined parts of prominent erosion surfaces, some of which mark the bases of channel bodies that may have been active or abandoned at the time of vegetation growth or log buildup.

ROF 6 is interpreted as representing *forced mid-channel bars* that typically overlie *forced mid-channel pools* (fmb, fmp), with hydraulic forcing around the obstacles. Similar features have been documented as vegetation-induced sedimentary structures or VISSs (Rygel et al. 2004; Ielpi et al. 2015). A few sheets to lenses of facies Fm locally show V-shaped features 1.0 m deep (Fig. 11D) that are inferred to mark the former positions of trees lost to windthrow or decay. The bedsets are interpreted as the remnants of *floodplains* (fp), possibly denoting vegetated islands in the channel belts.

Interbedded Muddy and Sandy Strata (ROF 7).—ROF 7 deposits are flat-lying and gently inclined sheets and lenses of gray strata in all the channel belts (e.g., Fig. 8B). Exposures at the base of Channel Belt A and fine, pale layers visible in drone images indicate that most fills comprise thin beds of massive sandstone (Sm), along with drab-colored laminated and massive mudstone (Fl, Fm). Contorted laminae in some fills may denote small slumps, and one prominent slump block was identified (Fig. 3). Most occurrences in the channel belts (subset 7A) occupy discrete hollows and are up to 2.5 m thick in the S–N face, averaging 0.8 m (66 examples). In some cases, extents of tens of meters generate an elongate appearance in the broadly flow-parallel S–N face.

ROF 7 is interpreted as *abandoned channel fills* (abc) of primary and secondary channels. The low average thickness of the occurrences indicates that the sediment filled small channels or larger channels that had been substantially filled with sand. In the three fine intervals, extensive sheets up to 3 m thick (subset 7B) are interpreted as the deposits of *floodplain lakes* (fl; e.g., Figs. 8A, 10A, C).

As shown in Figure 12A, the depth of channel scours (ROF 2A) scales broadly with the thickness of strata interpreted as bank-attached bars, components of mid-channel bars, and forced mid-channel bars (ROFs 3–6). Preserved planar cross-sets of ROF 4 are much thinner on average. There is little indication of systematic change in the scale of the inferred geomorphic units between the three channel belts.

Relative Proportions of Remote Outcrop Facies

Sand sheets (ROF 1) and channel scours (ROF 2) average 48% and 28% of the outcrop panels, respectively (Table 6). The boundaries of the two types are relatively diffuse, in contrast with other types and, together, they average 76% as an interconnected geomorphic assemblage (see Fig. 11A, B for good examples). Bank-attached and related geomorphic units (ROF 3) are relatively uncommon, averaging only 1% but forming 7% in one panel (Fig. 8B). Several prominent occurrences are present in the southern, less well exposed part of Channel Belt A, which was not amenable to analysis. The slipface components of unit bars (ROF 4) average 2% but form 6% in one panel with stacked sets (Fig. 8A). Mounded bar cores (ROF 5) average 11% but form 18% in one panel. Bars and pool fills associated with vegetation (ROF 6) average 1% but form 3% and 5% in two panels. Collectively, the bar components represented by ROFs 3–6 average 15%, with 22% in one panel. Abandoned-channel fills (ROF 7A) average 8%.

Oriented broadly along paleoflow, the S–N face is suitable for identifying downstream-accreting components of macroforms but is less suitable for identifying obliquely or laterally accreted components that may include bank-attached bars. The latter, however, are not prominent in the broadly across-flow E–W face (Fig. 3). The proportion of abandoned channel fills is underestimated in the along-flow section, which does not necessarily show the maximum thickness of the fills. For Channel Belt A, abandoned-channel fills comprise 8% of each of the two panels in the S–N section but constitute 16% in the equivalent section of the E–W face, where individual occurrences are thicker (Fig. 3).

Table 6 demonstrates that bar components (ROFs 3–6) are more abundant in Channel Belts A and B than in Channel Belt C. The latter channel belt has a relatively higher proportion of sand sheets, generating a planar appearance, and a lower proportion of channel scours (Figs. 11, 12B). Forced mid-channel bars and pools form low proportions in the upper two channel belts but are also present outside the analyzed panels in Channel Belt A (Fig. 11C–E). The distinction of sand sheets (ROF 1) and channel scours (ROF 2) may be problematic because: 1) many flat-lying sand sheets have scoured bases, 2) channel scours with concave-up erosional forms are best identified in transverse sections, and 3) channel-scour fills commonly grade up into unconfined, sheet-like bedsets.

System-Scale Architecture

Architecture of Channel Belts and Channel Bodies.—Channel Belts A–C are 16.5 m, 9.5 m, and 9 m thick, respectively (Figs. 2, 3), and they are associated with a suite of stratigraphic surfaces (Table 5). *Channel-belt bases* are relatively planar along the S–N face, with a few meters of relief. Channel Belt A thins southward, and Channel Belts B and C are amalgamated in the central part of the face, cutting out Fine Interval C. *Channel-belt tops* for Channel Belts A and B appear scalloped with small channel cuts, grading up locally into the overlying finer intervals. In contrast, Channel Belt C has a sharp, planar upper surface all along the S–N face.

Sixteen channel bodies or stories were identified in the multistory channel belts in the S–N face, resting on *channel bases* that form prominent, extensive erosional surfaces. Although a few channel bodies have relatively uniform thickness all along the S–N face (e.g., 14 and 16), most are cut out below overlying channel bodies (e.g., 5 and 15). Some rest on erosion surfaces that lose their prominence laterally, requiring channel bodies to be grouped (e.g., 9–11). The channel bodies contain numerous smaller channel scours, and it was a matter of judgment which to number in the spectrum of thickness and extent. The most extensive channel bodies are inferred to represent channel belts and primary channels, with component channel scours representing smaller braid channels. Channel-body thickness shows little upward change in the channel belts. An exception is channel body 7, which is a composite of thin channel fills along the top of Channel Belt A, representing a suite of channels emplaced in the final stage of the channel belt or cut after avulsion.

The numbered channel bodies average 3.6 m in maximum thickness, ranging from 1.8 to 6.5 m (Fig. 12A). Some sandstone bedsets lack major erosional surfaces and pass upward into fine-grained abandoned-channel fills that are truncated below the next prominent erosional surface. These large-scale facies successions are slightly thinner, averaging 2.9 m in thickness and ranging from 1.0 to 5.1 m ($n = 50$, Fig. 12A).

Although the true widths of the channel bodies could not be established, most of those recognized on the S–N face could be traced round the outcrop corner into the E–W face, where additional channel bodies were identified and numbered in accord with their relative elevation (e.g., 11A–D, Fig. 13A, B). The apparent widths of channel bodies that have both margins visible in Figure 13B range from 15 to 205 m, with an average of 82 m ($n = 19$).

The fluvio-lacustrine strata of the three fine intervals (9.5 m, 6.5 m, and 3.5 m thick, respectively) extend all along the S–N face, except where Fine Interval C is cut out by channel-belt amalgamation. Bedsets of facies Sm and Fl up to 4 m thick (Fig. 5A, B) are associated with lensoid channel bodies that rest on concave-up to sub-planar bases, locally crosscutting and amalgamated in places with the overlying channel belts (Fig. 2). These channel bodies contain flat-lying to gently concave-up sandstone layers attributed to sand sheets, channel scours, and unit bars and the cores of mid-channel bars. Their fills aggraded upward and inward from the channel margins, in some cases leaving an abandoned channel that was later filled and overtopped with fines (Figs. 8A, 10A, C). Lensoid channel bodies in Fine Interval A average 4.3 m thick (3.5 to 5 m range, Fig. 12A), and eight channel-bodies in Fine Intervals B and C average 2.5 m thick (1.8 to 3.8 m range). These values are less than the overall thickness of channel bodies and facies successions in the channel belts, but the aggregate thickness is difficult to determine where channels in the fine intervals were overtopped by fines.

Cross-Sectional Geometry of Channel Belts.—Ten numbered events in channel-belt evolution were recognized in the transverse cross section of Figure 13B. During initial emplacement of the Swartberg rivers, Channel Belt A incised to its deepest level near the outcrop corner (event 1), with the base rising westward by 20 m over 235 m. The abundance of

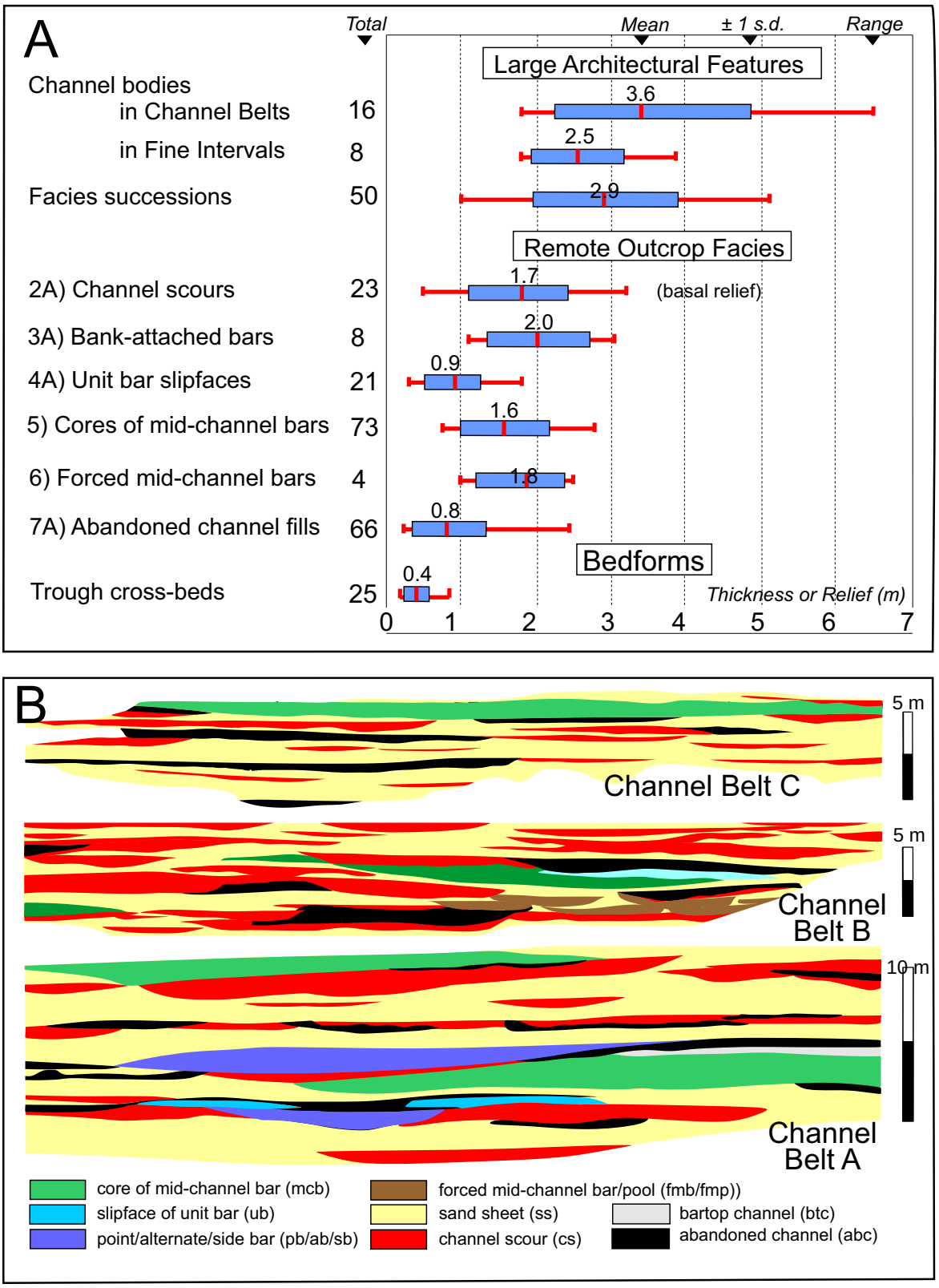

FIG. 12.—**A)** Thickness of channel bodies and facies successions, and remote outcrop facies and geomorphic units (269 measurements), and 25 cross-beds in the S–N face of Swartberg Koppie. The channel-body measurements represent maximum values in the cliff section, whereas facies successions represent sites with an upward transition from sandstone to mudstone. Bar components (remote outcrop facies) scale broadly with the channel bodies but are thinner. **B)** Mosaics of geomorphic units in 2-D panels of Channel Belts A, B, and C (Figs. 8B, 10B, and 11A, respectively). Sand sheets (ss) and the fills of channel scours (cs) predominate in all three panels, especially in Channel Belt C, with bar components prominent in Channel Belts A and B and at the top of Channel Belt C. See Table 6 for the proportions of geomorphic units in these and other panels.

TABLE 6.—*Proportion of remote outcrop facies in 2-D images of Channel Belts A–C in the S–N face. The seven panels are those interpreted in Figures 8A and 8B, 10A, 10B, and 10C, and 11A and 11B, as shown in left-hand column. Three of the mosaics are illustrated in Figure 14.*

Remote Outcrop Facies (ROF)	Flat-Lying Strata (1)	Strata within Concave-up Surfaces		ROF 1 + 2A + 2B	High-Angle Inclined Strata at Scour Margins (3A, B)	High-Angle Inclined Strata with Flat-Lying Bedsets (4)	Mounded Macroforms (5)	Vegetation-Influenced Strata (6)	ROF 3–6	Interbedded Muddy and Sandy Strata (7A)
		(2A)	(2B)							
Geomorphic Unit	Sand sheet (ss)	Channel scour (cs)	Bartop channel (btc)		Point/alternate/side bar (pb/ab/sb)	Slipface of unit bar (ub)	Core of mid-channel bar (mbc)	Forced mid-channel bar/pool (fmb/fmp)		Abandoned channel (abc)
Channel Belt C										
Panel 2 (11B)	61	24	0	85	0	1	6	3	11	4
Panel 1 (11A)	60	14	0	73	0	0	14	0	14	12
Channel Belt B										
Panel 3 (10B)	41	36	0	77	0	2	7	5	14	10
Panel 2 (10C)	38	40	0	77	0	0	18	0	18	4
Panel 1 (10A)	43	31	0	73	0	1	13	0	15	12
Channel Belt A										
Panel 2 (8B)	50	18	2	68	7	1	14	0	22	8
Panel 1 (8A)	44	33	2	77	1	6	6	0	12	8
Average	48	28	1	**76**	1	2	11	1	**15**	**8**

facies Gl with reworked mud fragments in the basal strata indicates considerable erosion into the underlying fluvio-lacustrine strata during avulsion (reworked mudstone fragments are not apparent in drone images of the higher channel belts). Channel bodies 1 to 7b progressively onlapped this basal surface, with renewed incision of channel body 3a and a broadening of individual channel bodies (events 2, 3) before abandonment (event 4).

Channel Belt B reoccupied the area (event 5) with the point of deepest incision ~ 100 m west of the deepest point of Channel Belt A. The base rises westward by 10 m over 100 m. Channel bodies 7c to 11d progressively onlapped the basal surface (event 6), broadening the channel belt before abandonment (event 7). Channel Belt C has a point of deepest incision close to that of Channel Belt A (event 8), broadening with several extensive channel bodies and less systematic basal onlap (event 9), before abandonment (event 10). The maximum relief on the channel-belt base is 6 m. Successive channel belts were thinner and less extensive.

The numerous channel bodies in the multistory channel belts imply the repeated abandonment and relocation of primary channels in the belt. The avulsion that ended sediment accumulation in each channel belt probably resulted from aggradation in the initial incision and later broader conduit until the conduit was unable to contain the largest discharges. There is no indication that extrinsic factors, such as tectonic or climatic events, controlled channel formation, filling, and avulsion, although that cannot be ruled out.

Strong and Paola (2008) distinguished *topographic valleys*, which existed at near-maximum depth during initial incision, from *stratigraphic valleys*, for which the bounding surface evolved when later channels cut into aggrading floodplain sediment. In the latter case, the preserved valley form does not correspond to a discrete valley at any point in time. Channel Belt A, with 20 m of relief from its deepest eastern point to its westward termination, probably occupied a shallow topographic valley underlain by a master surface because abundant mud fragments in the basal strata are indicative of strong local incision. Furthermore, the thickness of channel body 1 is only 4.5 m, which would imply the considerable accretion of some 15 m of floodplain sediment during the life of the channel belt, if the channels and floodplains had aggraded together. Shallow topographic valleys also probably best describe the higher, thinner channel belts with their zones of deeper incision.

Channel clustering also may have influenced the architecture. Channel bodies may show clustering due to repeated local avulsions and the tendency for channels to occupy depressed areas generated by subsidence or differential compaction (Hajek et al. 2010; Hofmann et al. 2011). In the present study, channel bodies 3a and 14c are more deeply incised than the adjoining channel bodies. These channel bodies may represent separate avulsions in the fluvial zone, with channel fill later incorporated into the channel belts when overlying, more extensive channel bodies (6 and 16b) cut across them. Additionally, channel body 3a appears to be capped by floodplain deposits at its left-hand margin (Fig. 13B), implying a gap in time before the rest of Channel Belt A was formed. Examination of the adjoining floodplain deposits might indicate the relative importance of valley formation and channel clustering because: 1) mature paleosols adjacent to channel-belt tops would imply limited overbank flow and prolonged soil formation adjacent to a valley cut, whereas 2) crevasse splays extending from channel bodies into the floodplain deposits would imply the presence of alluvial channels with active floodplains. However, exposure of fine-grained strata is minimal in the cliff face, where vegetation and debris cover the outcrop. An unsuccessful attempt was made to trace finer beds laterally from the accessible basal strata, and traceable beds were not identified in the drone images.

The deepest incision in all three channel belts is close to the cliff corner. This implies that the S–N cliff line approximates the thickest original development of the Swartberg Koppie fluvial channel belts. These channel belts thinned westward (Fig. 13B) and probably also eastward, where fine-grained floodplain and fluvio-lacustrine deposits would have been eroded to yield the modern escarpment and valley. The southward rise of the basal

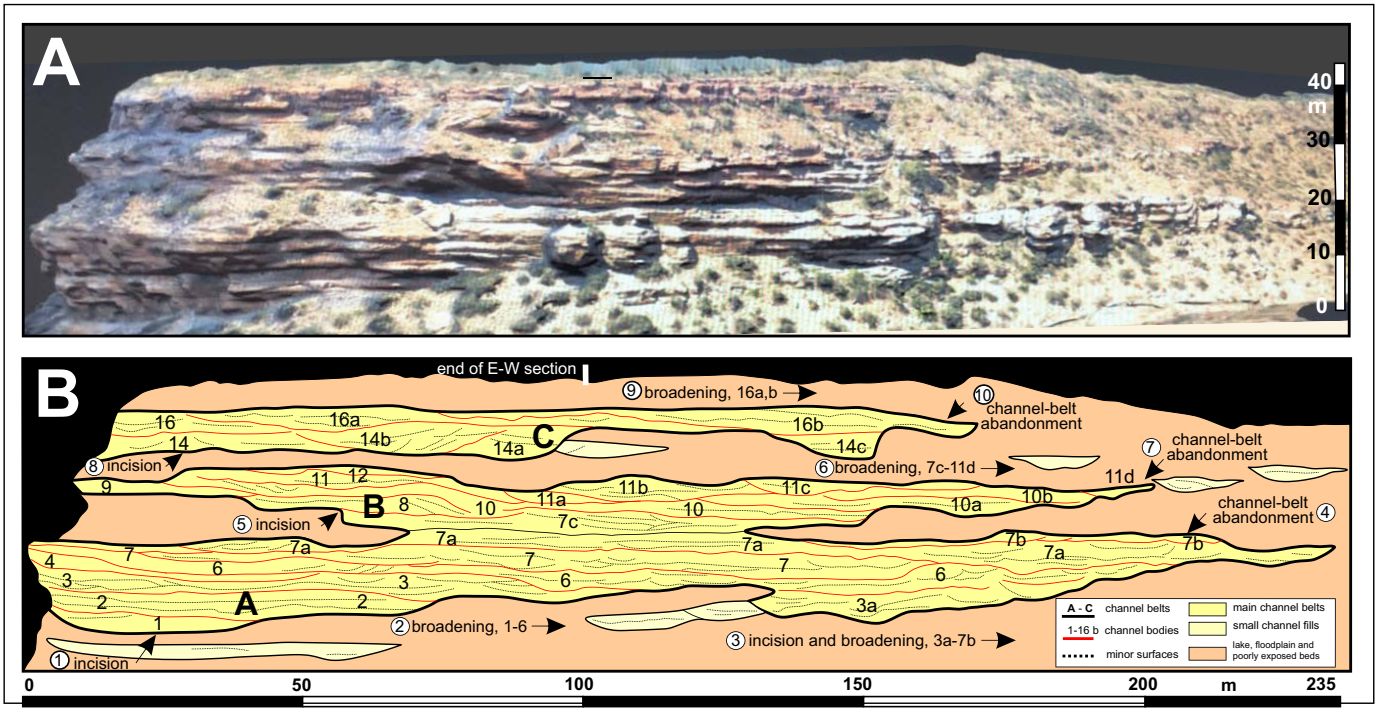

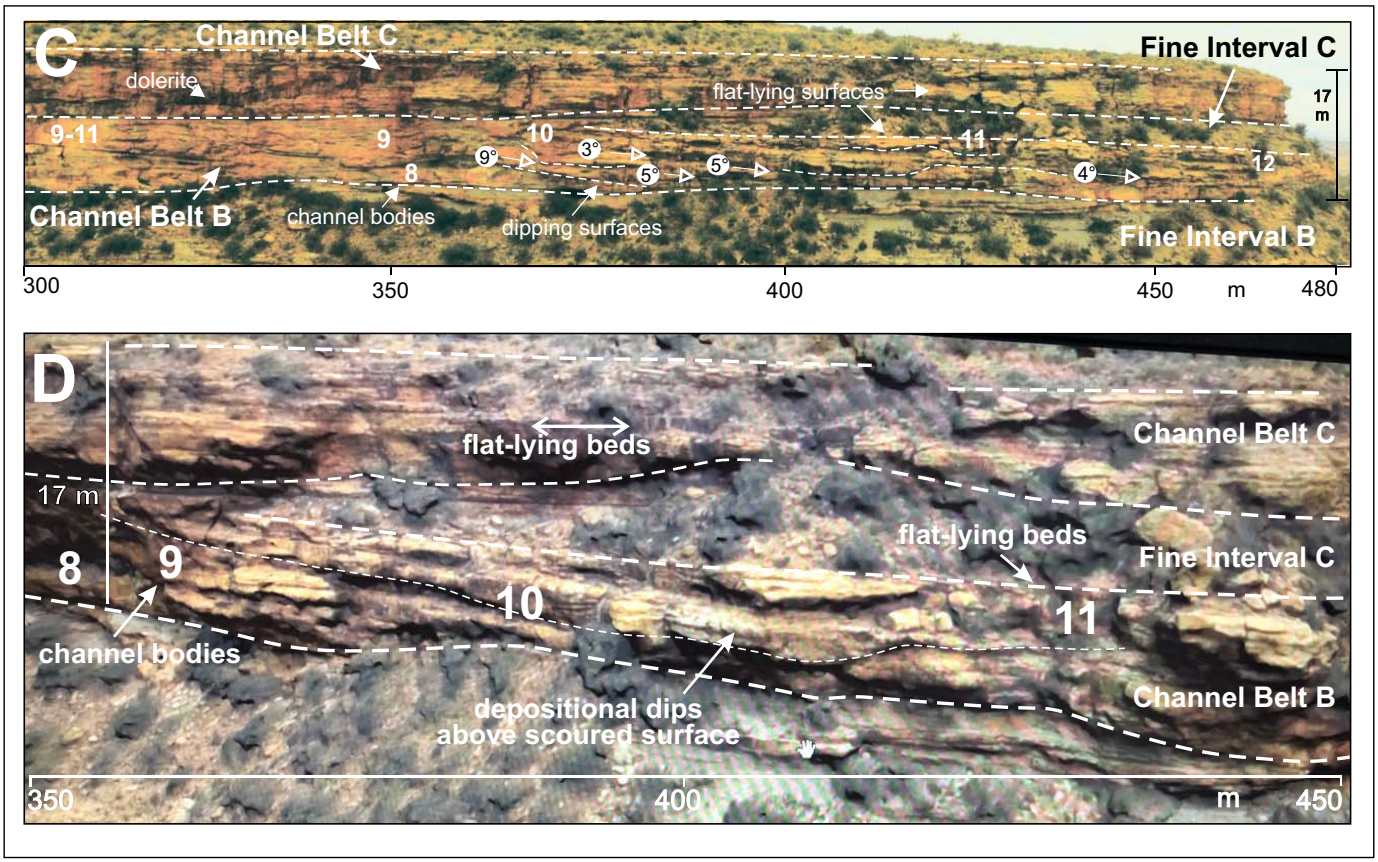

FIG. 13.—**A)** Uninterpreted and **B)** interpreted view of E–W profile from 3-D model of Swartberg Koppie, showing channel-belt architecture in a section broadly transverse to paleoflow direction. Notations of a) to d) represent channel bodies that were not apparent and numbered in the S–N profile. Ten major events are circled. The three channel belts show initial incision in shallow valleys, after which the conduit widened with a rising basal surface and progressive onlap of younger channel bodies. Abandonment of the channel belt resulted in a subplanar top surface. The approximate half-width of Channel Belt A, from deepest incision to western margin is 235 m, and the overlying channel belts are thinner and narrower. **C**, **D)** Steeply inclined large-scale bedsets in Channel Bodies 9 and 10 of Channel Belt B, indicative of a possible tributary system. The inclined surfaces have apparent northward dips of up to 9° and can be traced for ~ 150 m in the S–N face.

TABLE 7.—*Channel, hydraulic, and basinal parameters for 16 channel bodies in Channel Belts A–C. Estimates are from equations in Long (2021), derived from data for > 4,000 modern rivers.*

	Maximum Storey Thickness	Decompacted Thickness (Thalweg Depth)	Average Bankfull Depth	Bankfull Channel Width	Bankfull Discharge	Drainage Basin Area
Symbol	d_{max} (measured)	d_{max}	d_{bf}	w_{bf}	Q_{bf}	DA
Unit	m	m	M	m	m^3s^{-1}	km^2
Maximum	6.5	7.5	3.8	172	211	4284
Minimum	1.8	2.0	1.1	37	41	285
Average	**3.5**	**3.9**	**2.1**	**84**	**99**	**1370**

surface of Channel Belt A (Fig. 2) indicates the presence of a valley margin in that area and possibly an oblique orientation of this part of the channel belt relative to the cliff line.

Channel Belt A appears to be the widest of the three, in accord with its greater thickness. Its width is at least 235 m in a broadly transverse section (Fig. 13B). With deepest incision at or near the outcrop corner, an original channel-belt width of twice this amount (~ 500 m) is likely. Channel Belt B thins both east and west from its area of greatest thickness, and its width may not have greatly exceeded 200 m. Channel Belt C has a width of at least 170 m and may originally have been 200–250 m wide.

Tributary Systems.—Channel Bodies 9 (3.9 m) and 10 (2.7 m) in Channel Belt B rest on inclined erosional surfaces that show an apparent northward dip, as do their overlying bedsets (Figs. 2, 13C, D). Apparent dips are typically 3–5° but locally as high as 9° (minimum estimates of the true dip). The steeper bedsets in channel body 10 extend for ~ 100 m along the outcrop face, and the apparent overall extent of inclined strata is ~ 150 m. In contrast, bedsets in the overlying channel body 11 are flat-lying, as are those in Channel Belts A and C.

Such steep depositional dips are unusual for a trunk channel. The base of Channel Belt B appears flat-lying, and the steep dips are not readily explained as cascades or rapids at a knickpoint in the river floor. However, similarly steep dips have been documented in small alluvial fans, such as those of Death Valley (Blair 1999), which have surface slopes of up to 5° and bedsets that dip downfan at 5°. In a Pennsylvanian valley fill in Kansas, Feldman et al. (1995) mapped well defined tributaries with benches on limestone substrates that imply rapids or waterfalls dropping steeply to the trunk channel. A steep tributary system provides a possible explanation for the inclined bedsets of Channel Belt B, with the northward dips reflecting an angled confluence into the trunk channel. It is not clear whether such a tributary entered from the west or the east.

In the 200–250 m region of Figure 2, relatively thick fluvio-lacustrine beds of Fine Interval C lie to the south (upflow) of amalgamated sandstones of Channel Belts B and C. A lensoid channel body (part of channel body 9) underlies the lacustrine beds, which are bounded to the north by channel body 10 and are cut by channel body 11 of Channel Belt B. Tracing was difficult in this part of the profile, which is also affected by a dolerite intrusion. However, sand deposited from tributary systems (possibly represented by the three channel bodies) may have impounded small lakes in the tributary or trunk channel. In upland valleys of western Canada, steep tributary systems with high loads build out into the trunk channels, locally overloading the system and impounding the flow in wetlands (Makaske et al. 2017).

Quantitative Estimates for Fluvial Parameters

The maximum (story) thickness, corrected for compaction, for the thicker channel bodies is considered representative of the braided-channel belt at its largest dimensions. The thinner channel bodies may represent smaller channel belts, tributary channels, or local braid channels. The maximum thickness serves as a proxy for maximum thalweg depth (d_{max}), which probably represents the deepest scour at braid-channel confluences (Long 2021). Although most channel-body thicknesses are minimum estimates measured between major erosional surfaces, inspection showed that the topmost, complete stories in each channel belt are similar in thickness to those below. Facies successions that include mudstone are on average thinner than maximum story thicknesses (Fig. 12A), although decompaction of the mudstone would generate a better match.

The maximum thalweg depth and the calculated bankfull width yield an approximation of the active-channel dimensions. The *maximum thalweg depth*, corrected for compaction, was calculated as 2.0 to 7.5 m for the 16 channel bodies, averaging 3.9 m (Table 7). The *average bankfull depth* was calculated at 1.1 to 3.8 m, averaging 2.1 m. These results exceed slightly, but accord broadly with, the measured height of bank-attached bars (average 2.0 m) and mid-channel bar components (average 1.6 m) in Figure 12A, not corrected for compaction. The *bankfull width* was calculated at 37 to 172 m, averaging 84 m. Although true channel width could not be determined, the estimates are broadly in accord with the average apparent width of 82 m in the E–W face.

Bankfull discharge averaged 99 m^3s^{-1}, and drainage basin area averaged 1370 km^2. These results are considered provisional due to uncertainties in channel-body and belt geometry for multichannel, braided systems (Long 2021).

Fluvial Style

Four fluvial styles are represented in parts of the Swartberg member outcrop (Fig. 14). Style 1 (*Channel-Bar Complex*) is the predominant style of Channel Belts A and B, comprising sand sheets, channel scours, components of mid-channel and unit bars, bank-attached bars, and abandoned-channel fills. The abundance of trough cross-beds in the sand sheets, and the prominence of mid-channel bar components, are indicative of perennial flow conditions.

Style 2 (*Low-Sinuosity Complex*) is notable for the prominence of bank-attached bars with benches and associated accretionary banks, passing laterally into sand sheets. The style is best developed in discrete channel cuts in the southern part of the S–N face. Here, Channel Belt A thins and the bars developed against steeper banks with more resistant substrates of the underlying Fine Interval A (Fig. 2). The limited extent of inclined bedsets is evidence to support an interpretation of alternate or side bars rather than point bars, which typically show sustained migration over longer distances. Style 2 is likely indicative of a low-sinuosity channel form, although planform outcrops are not available for confirmation.

Style 3 (*Sand Sheet and Scour Complex*) comprises sand sheets composed of flat-lying bedsets with trough cross-beds, along with channel scours, a small proportion of mid-channel bar components, and abandoned-channel fills. The style characterizes Channel Belt C, which is notable for its planar form and even upper surface with plane beds (Sh) and mounds (Sac).

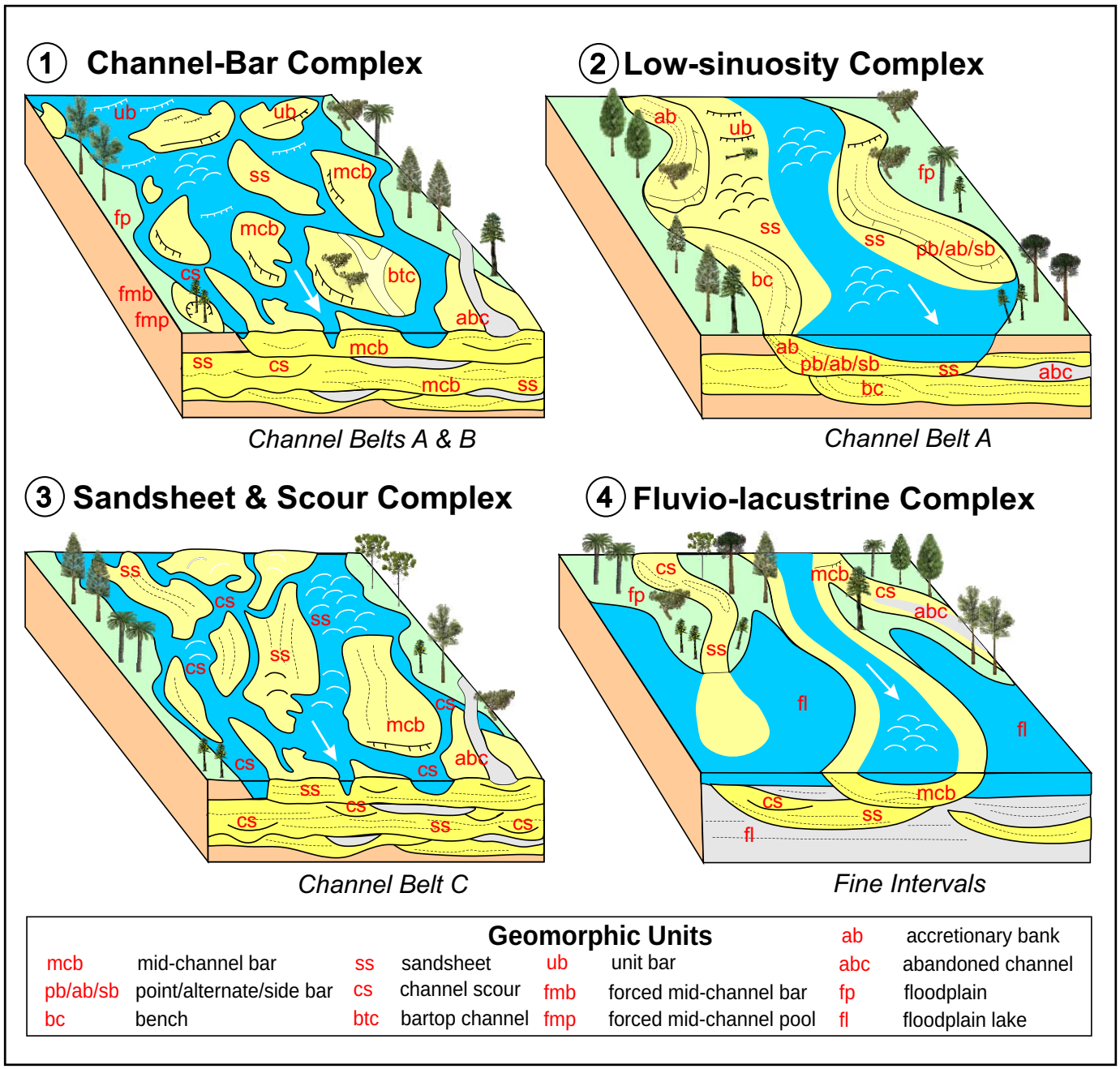

FIG. 14.—Block diagrams to illustrate four major fluvial styles in the Swartberg member exposed on the Bethel and Heldenmoed farms, Free State Province. Styles 1 and 3 predominate, with mid-channel bars, sand sheets, and channel scours, and Style 2 with bank-attached bars is present locally in discrete channels, probably with low-sinuosity planform. Vegetation illustrates Triassic taxa.

The channel belt is capped by a prominent unit bar that accreted over an apparent distance of 50 m.

Style 4 (*Fluvio-Lacustrine Complex*) represents the three fine intervals, where stratified mudstone and sandstone were laid down in shallow standing water bodies (lakes). Thickening/thinning rhythms (Fig. 5B) suggest the advance and retreat of supply from point sources. Bioturbation was not observed where the stratified deposits could be examined, for reasons that are not clear, but lake deposits elsewhere also show a scarcity of bioturbation (e.g., Simon et al. 2016). Associated lensoid channel bodies with sand sheets, channel scours, and a few mid-channel and unit bars are interpreted as distributary channels a few meters deep (Fig. 12A).

Fine Interval A comprises nearly 10 m of strata and is well exposed at the outcrop corner, overlying reddish-gray mudstone. This interval represents a prolonged lake phase with Style 4 channel bodies, before the avulsion into the area of a major fluvial system. There is no indication from the outcrop belt as to why a lake formed at this level and what the containing dam may have been. Fine Intervals B and C are thinner (6.5 and 3.5 m, respectively), with similar but thinner Style 4 channel bodies, representing standing water in shallow trunk and tributary valleys following avulsion of the channel belt. Wetlands and lakes are prominent in many modern valleys, including systems such as Mulwaree Ponds of Australia (Williams and Fryirs 2021), where reduced river flow has led to chains of lakes, some of them occupying

TABLE 8.—*LA-ICPMS U-Pb age results from pedogenic nodule samples, Swartberg Koppie, South Africa. MSWD, mean square of weighted deviations; PbC, $^{207}Pb/^{206}Pb$.*

Sample	^{238}U ppm	^{206}Pb ppm	Th/U	Age (Ma)	MSWD	$^{207}Pb/^{206}Pb$ (PbC)
120822-8	33.9	4.4	0.23	**241 ± 3**	1.0	0.822 ± 0.008
120822-7	16.7	5.7	0.16	**243 ± 2**	1.8	0.834 ± 0.005
120822-4	12.6	4.2	0.17	**247 ± 10**	1.5	0.841 ± 0.006

former thalweg positions. The tops of the channel belts are uneven, and there is plenty of scope for local blockage by trunk and tributary sand.

U-Pb Geochronology of Pedogenic Nodules

Analytical results of U-Pb LA ICPMS dating of calcite-cemented pedogenic nodules are presented in Table 8. Sample 120822-7 is an *in situ* paleosol nodule collected in the hillslope outcrop ~ 94 m below the base of the Swartberg member (Fig. 15; S–30.41836°, E 026.26051°; Supplemental Material S1). The sample gives an age estimate of 243 ± 2 Ma (2σ; MSWD = 1.8) indicating that crystallization occurred in the late Anisian or early Ladinian (Fig. 1D). Sample 120822-8 (S 30.41847°, E 026.26016°) was collected from a reworked intraformational conglomerate, representing the recalcitrant remains of a "ghost paleosol" (Gastaldo et al. 2020b), overlying the previous sample site by ~ 15 m (~ 80 m below the Swartberg base). This sample gives an age estimate of 241 ± 3 Ma (2σ; MSWD = 1.0) indicating that the paleosol in which the nodule precipitated was early Ladinian or late Anisian.

One additional sample, 120822-4 (S 30.414654°, E 026.261167°) collected lower in the section contained high common Pb and was insufficiently radiogenic to yield a precise age date. This is reflected in the clustering of data points towards the Y axis (common Pb component), indicating that the system was reset (Supplemental Material S1). Hence, the age of this sample cannot be determined with a high degree of accuracy, resulting in an uncertainty of 10 Ma (247 ± 10 Ma, MSWD = 1.5).

DISCUSSION

Comparison of Swartberg Fluvial Styles with Modern Braided Rivers

Sandy braided rivers of the western North American plains provide partial analogues for the Swartberg Koppie outcrop. These rivers include the Platte (Smith 1970, 1971, 1972; Blodgett and Stanley 1980; Crowley 1983; Horn et al. 2012a, 2012b), Niobrara (Skelly et al. 2003), Calamus (Bridge et al. 1986, 1998), and Wisconsin (Mumpy et al. 2007) of USA, and the South Saskatchewan of Canada (Sambrook Smith et al. 2006; Parker et al. 2013). The grain size of these rivers is typically greater than that in the Swartberg member. Large rivers elsewhere, such as the Brahmaputra and the Paraná, also provide partial analogues (Best et al. 2003; Sambrook Smith et al. 2009). Lunt and Bridge (2004) noted that a generalized braided-fluvial model applies to sandy and gravelly systems, and analogues may also be found in the gravelly Sagavanirktok River of Alaska (Lunt and Bridge 2004) and the Squamish, Fraser, and Kicking Horse rivers of Canada (Wooldridge and Hickin 2005; Cyples et al. 2020). Most of these rivers exhibit anthropogenic effects, including dams and water takeout, requiring caution in their application to fluvial systems in deep time.

Fluvial parameters for the Swartberg Koppie outcrop match the scale of braided channels on the North American plains. For example, the South Saskatchewan has a channel belt ~ 600 m wide with the main channels 50–150 m wide and 2–5 m deep, with maximum thalweg depths typically ~ 3 m below the tops of the adjacent compound bars (Sambrook Smith et al. 2006; Parker et al. 2013). The Niobrara has a channel belt 90–330 m wide (Skelly et al. 2003), and vegetated banks of the Platte are up to 2 m high (Smith 1971). In all these rivers, the channel belts comprise channel-bar complexes with primary and secondary channels, mid-channel unit bars, amalgamated compound bars, and bank-attached bars. Vegetated islands with trees and woody debris are prominent. Swartberg fluvial styles 1–3 have good analogues in many of these river systems. Near Outlook, Saskatchewan, Parker et al. (2013) noted that bars were generally overtopped when flows exceeded 230 m^3s^{-1}, in accord with the maximum bankfull discharge calculated for the Swartberg member channel systems.

Reflector patterns similar to ROF 1, with flat-lying strata and abundant cross-stratification, are widely represented in GPR profiles, especially in along-flow traverses (Skelly et al. 2003). The facies is prominent in primary and secondary channels where sinuous-crested dunes are abundant (Sambrook Smith et al. 2006; the "open-water channels" of Horn et al. 2012a, 2012b), as well as within and capping mid-channel compound and unit bars (Mumpy et al. 2007; Parker et al. 2013). Radar facies with these features account for 40–83% of the profile areas (Wooldridge and Hickin 2005; Sambrook Smith et al. 2009; Parker et al. 2013; Cyples et al. 2020). Flat-lying beds with transcritical plane beds are prominent in ephemeral rivers with strongly seasonal flow, including the Ghash River of Sudan (Abdullatif 1989) and the Luni River of India (Carling and Leclair 2019), but the prominence of trough cross-beds in the Swartberg outcrop is indicative of more sustained flow conditions. Many analogues exist for the channel scours of ROF 2. For example, GPR profiles in the Platte River, Nebraska, imaged the fills of secondary channels 1–3 m deep and 10–20 m wide, as well as smaller bartop channels (Horn et al. 2012a).

The macroforms represented in ROFs 3–6 also can be matched in many GPR profiles. The bank-attached bars of ROF 3 resemble those of the low-sinuosity (< 1.3) channel of the Calamus River, where alternate bars and point bars form single or double rows depending on channel width (Bridge et al. 1986). The side bars of the Kicking Horse River are also possible analogues, attached to an accretionary bank and accreting downstream (Cyples et al. 2020). Bank-attached bars with benches and accretionary banks are prominent in strongly seasonal rivers of Australia and Canada (Brooks 2003; Page et al. 2003).

High-angle inclined bedsets, similar to those of ROF 4, form components of unit bars in many GPR profiles (transverse bars of Smith 1971, 1972; Horn et al. 2012a), with simple forms that remain relatively unmodified during bar migration (Smith 1971). The bars are typically lobate with straight-to-arcuate avalanche faces and a predominant down-current migration direction, with subsidiary lateral to oblique accretion. They generate tabular sediment bodies that are typically 1–2 m thick, and they commonly build into channel thalwegs and confluence scours (Sambrook Smith et al. 2019). The inclined bedsets dip steeply (15–36°: Smith 1972); the relatively low dips of 8–21° recorded in the Swartberg outcrop may indicate that the cliff cuts obliquely through the macroforms.

The mounded macroforms of ROF 5 have analogues in the convex-up bar cores imaged in across-flow radar profiles of the Niobrara River, Nebraska, developed over scours and with flanking clinoforms traceable for up to 10 m (Skelly et al. 2003). Similar features have also been noted in the Calamus and South Saskatchewan rivers (Bridge et al. 1998; Parker et al. 2013). The mounded macroforms at Swartberg Koppie are interpreted as components of compound bars, generated as assemblages of unit bars that

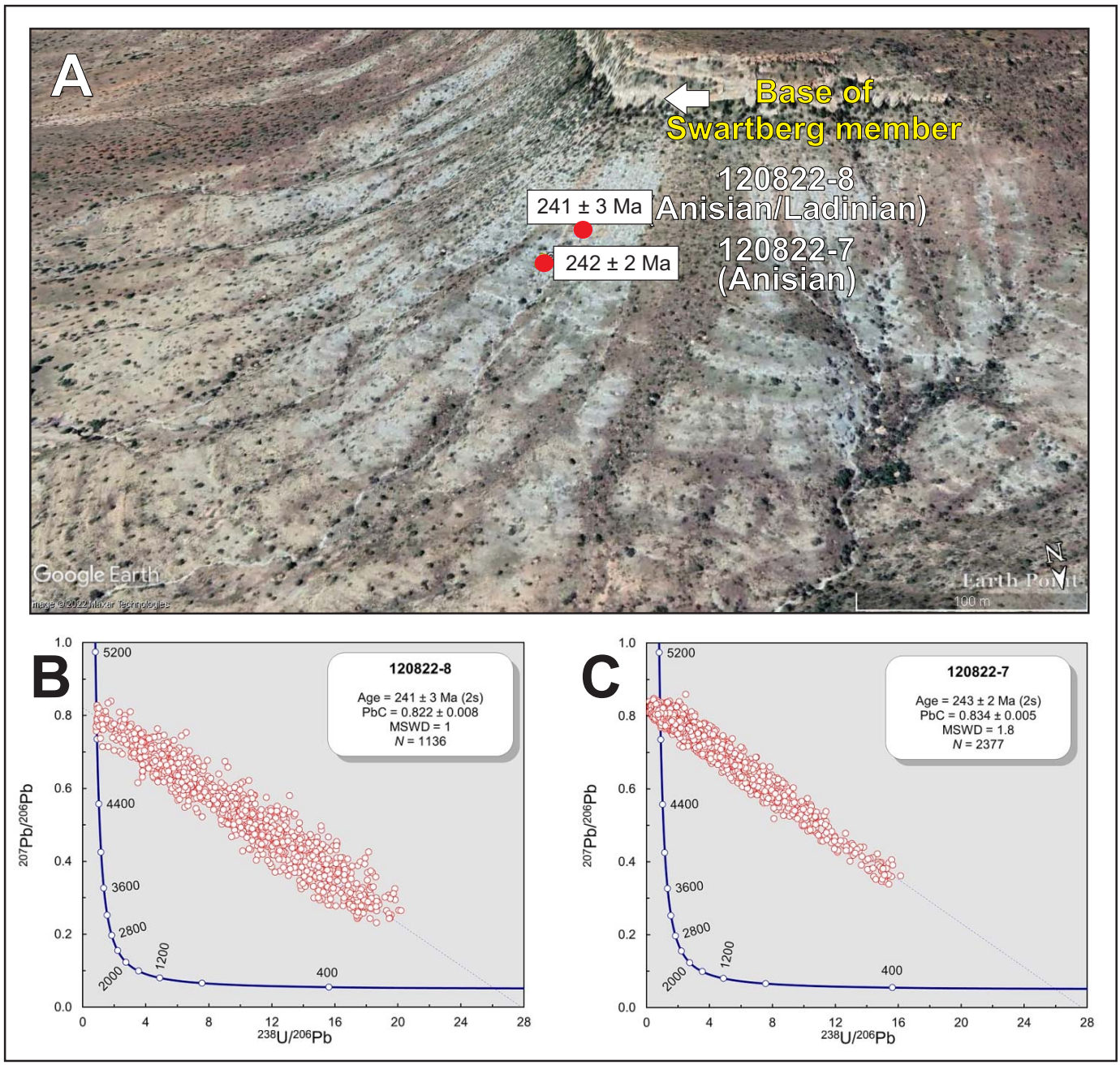

FIG. 15.—Sample locations and results of U-Pb LA-ICPMS analyses of pedogenic nodules collected in outcrop below the base of the Swartberg member (see Supplemental Material S1 for stratigraphic context). **A)** An oblique Google Earth image on which pedogenic nodule samples 120822-7 (S –30.41836°, E 026.26051°) and 120822-8 (S –30.41847°, E 026.26016°) are shown with U-Pb age estimates derived from pedogenic calcite cements. **B)** Concordia plot of Sample 120822-7. **C)** Concordia plot of Sample 120822-8.

evolved through erosional and depositional events (Lunt and Bridge 2004). In the Sagavanirktok River, Alaska, Lunt and Bridge (2004) documented compound bars composed of 3–7 sets of large-scale inclined strata, each formed by a unit bar.

Hyperbolic GPR reflections in rivers with abundant woody material have been attributed to buried logs (Mumpy et al. 2007; Cyples et al. 2020), suggesting parallels with ROF 6. The reflections are probably associated with forced mid-channel bars and pools, but these are difficult to image with GPR. Abandoned-channel fills (ROF 7A) are not widely documented in subsurface studies, but partially to completely abandoned channels are present in the Tagliamento River of Italy, especially at channel-belt margins (Tockner et al. 2003). The vegetated intervals of sandstone and mudstone illustrated in Figure 11D may represent vegetated islands.

Many studies have noted a contrast between surface morphology, where macroforms with avalanche faces are generally prominent, and the subsurface record where mesoform cross-beds, planar strata, and channel scours are prominent (Horn et al. 2012a; Parker et al. 2013). GPR profiles through bars are typically dominated by dunes, with a modest proportion (15–20%) of inclined reflector sets (Wooldridge and Hickin 2005; Sambrook Smith et al. 2009; Cyples et al. 2020). As discharge falls, bar

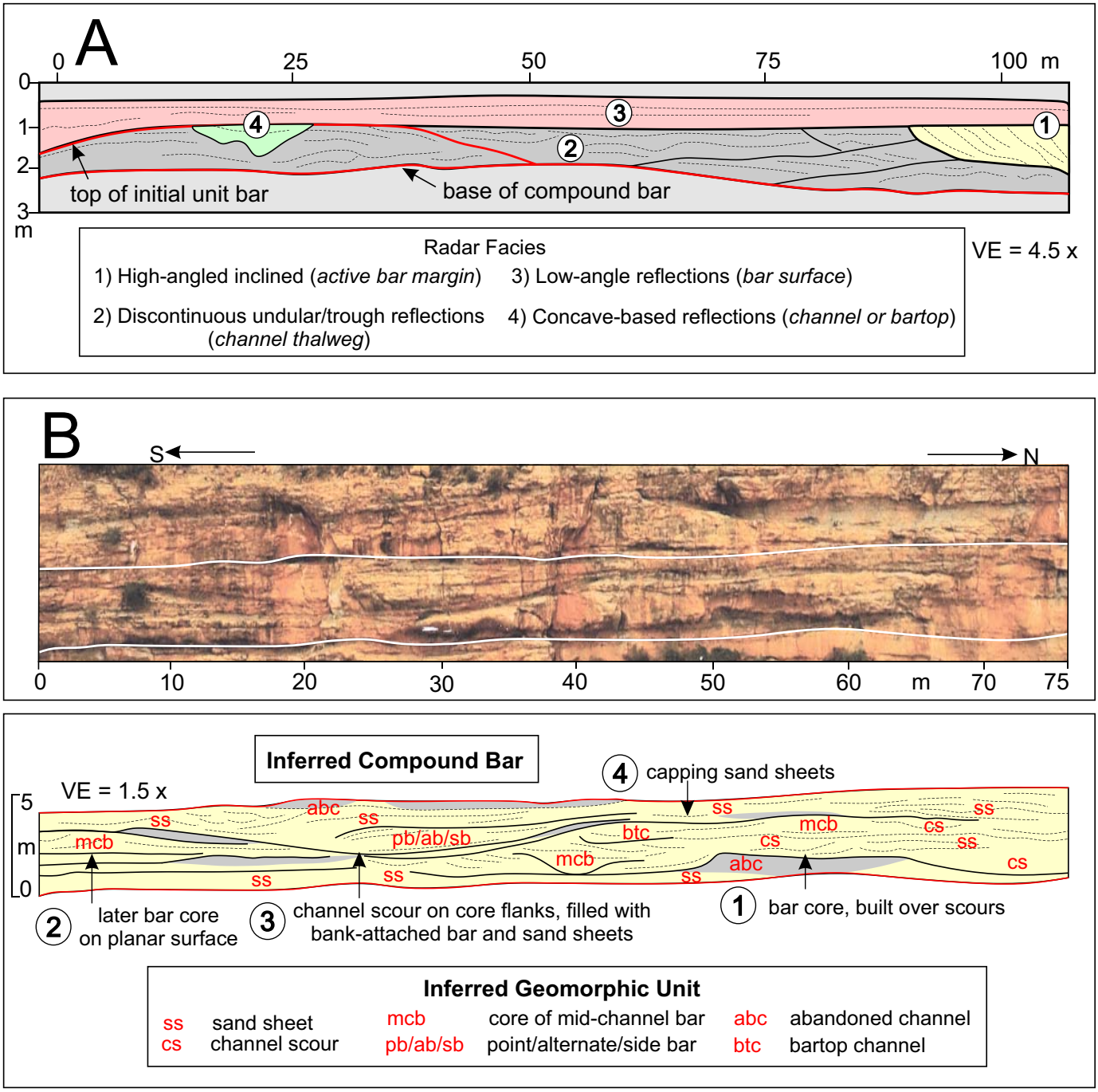

FIG. 16.—**A)** GPR profile through a compound bar in the South Saskatchewan River, Canada, with a succession ~ 2.5 m thick. The bar originated as a unit bar with a convex-up profile, ~ 1.5 high, cut by a bartop channel. The bar grew laterally and vertically through the addition of flat-lying channel thalweg and bar-surface deposits (principally dunes) and inclined bedsets generated at a bar-margin avalanche face. Modified from Parker et al. (2013). **B)** Inferred compound bar in Channel Belt A of the Swartberg member, with four stages in bar development.

tops and margins developed at high-flow stage are truncated, and slipface deposits are replaced with smaller dune sets and channel scours. Rhythms of macroform growth and reworking may operate over periods of only a few years.

In the South Saskatchewan River, Canada, Parker et al. (2013) noted some "textbook examples" of compound bars in GPR profiles, but typically only remnants were preserved, making diagnosis difficult. In one good example, an initial convex-up unit bar, ~ 50 m wide, developed into a large compound bar through the accretion of thalweg, bar surface, and avalanche-face deposits, the latter forming only a small proportion of the GPR panel (Fig. 16A, with 4.5× vertical exaggeration).

With a S–N face ~ 500 m long, the Swartberg Koppie exposure is long enough to image compound bars comparable in scale to those of modern rivers, which are commonly tens to several hundred meters in extent. However, the high proportion of flat-lying bedsets and channel scours (ROFs 1 and 2) and the modest proportion of macroforms (ROFs 3–6) are

indicative of substantial reworking, as in the modern analogues. An inferred compound bar with a thickness of ~ 4 m and an apparent length > 75 m is illustrated in Figure 16B, with 1.5× vertical exaggeration and four events highlighted. Resting on a scoured surface cut into an abandoned channel fill (abc), the mounded core of a mid-channel bar (mcb) occupies the 30–70 m position (event 1), with inclined accretion sets that show an apparent northward dip (Fig. 8B). The mound is cut by a shallow bartop channel (btc) and passes southward into a sand sheet (ss), overlain by a second mound (event 2). A shallow scour occupies the hollow between the two mounds and contains a small bank-attached bar that built from the flank of the initial mound, passing upward into sand sheets (event 3). Finally, sand sheets built up and flattened the topography over the mounds (event 4). Minor hollows on the mounded topography filled with mud. Joeckel et al. (2014) noted the amalgamation of architectural elements into compound bars in the Miocene Ogallala Group of the U.S. Great Plains.

Paleoclimate Assessment for the Swartberg Member

Fine-scale sedimentary features such as desiccation cracks, rain prints, and evaporite pseudomorphs have been widely used for paleoclimate reconstruction in the Beaufort Group (e.g., Stear 1978; Smith 1980), but they are below the resolution of the UAV images for the Swartberg member. However, the predominance of trough cross-beds in the sand sheets of all three channel belts implies perennial subcritical flow, allowing systematic bedform migration. Local plane-laminated and scour-and-mound sandstones (facies Sh and Sac) imply periods of transcritical and supercritical flow in shallow water, probably associated with episodic discharge (Wang and Plink-Björklund 2020). Facies successions that pass upward from subcritical to transcritical bedforms (Fig. 5A) are probably linked to shallowing upward in flow conduits. Channel scours (facies Ss and larger scour fills) indicate frequent erosive events. The prominence of bedsets interpreted as mid-channel bars supports an interpretation of sustained-flow periods close to bankfull level. The flat-topped bar at the top of Channel Belt C (Fig. 7), with an apparent accretion distance of 50 m and foreset erosion and reactivation, indicates seasonal variation in discharge with alternate high-stage accretion and low-stage erosion.

These observations collectively imply a humid, seasonal paleoclimate, under which rivers experienced sustained, perennial discharge with seasonal variation. The fluvial style accords with patterns of intermediate discharge variation (Fielding et al. 2018). Although the discharge pattern may reflect the paleoclimate in the Cape Fold Belt source area, water was in good supply on the landscape, as indicated by standing water in lakes in fine intervals, in blocked trunk and tributary channels, and in abandoned channels. The wide range of calculated discharge for the 16 channel bodies may imply variation in channel-belt discharge but more probably reflects scatter in the thickness of the sampled channel fills. Turner (1983) used similar reasoning to infer a humid paleoclimate for the Upper Triassic Molteno Formation.

Vegetation, including upright trees, is preserved in all the channel belts. Its presence is inferred from vegetation-induced sedimentary structures (VISSs) (Fig. 11C–E), associated with forced mid-channel bars and pools and floodplain remnants. Occurrences in the basal deposits of some channel bodies implies seasonal dryness or the growth of vegetation in abandoned channels. These structures have particular utility for evaluating the Permian and Triassic vegetation record of the Karoo Basin, where organic matter is commonly poorly preserved due to taphonomic factors (Gastaldo et al. 2005). Plant fossils are typically below the resolution of the drone images and may be more abundant than noted, although megafloral elements are preserved in less than 1% of these rocks (Gastaldo and Bamford 2023). Riparian vegetation is prominent in modern dryland areas, and the identification of VISSs does not necessarily imply a humid climate, although it may support other lines of evidence.

Temporal Relationship of the Swartberg Member to the End-Permian Event

Advances in obtaining U-Pb age estimates from calcite cements, including those from pedogenic nodules (Palafox et al. 2022; Rochín-Bañaga et al. 2023), provide a means to test hypotheses about the age and continuity of continental successions in the absence of volcaniclastic deposits. Currently, the Swartberg member at Bethulie is dated as Induan (e.g., Smith et al. 2022), based on the presence of an interval in which *Lystrosaurus* skeletons predominate (Viglietti et al. 2013). The genus has been interpreted as a disaster taxon (Botha-Brink et al. 2016; but see Modesto 2020) and is believed to represent post-extinction ecosystems of the very earliest Triassic.

Smith et al. (2022, their Fig. 2) reported a stratigraphic distance of less than 50 m between their vertebrate-defined End Permian Mass Extinction interval (EPME, the three-phased extinction model of Smith and Botha-Brink 2014, and others) and the *Lystrosaurus*-rich interval described as located less than 20 m below the base of the Swartberg member. Hence, these authors show a stratigraphic thickness between the EPME and the base of the Swartberg member of about 70 m, corresponding broadly to the lower part of the Katberg Formation. However, in previously published measured sections, Botha and Smith (2006) placed the base of the Swartberg member at 162 m above the Permian–Triassic boundary as defined by vertebrates. Consequently, there is significant ambiguity about: 1) where the base of the Swartberg member lies relative to the vertebrate-defined datum, and 2) the thickness of strata exposed on Swartberg Koppie, especially for the lower Katberg Formation. Our measured sections (Supplemental Material S1) indicate that the base of the Swartberg member lies ~ 210 m above the vertebrate-defined datum of Botha and Smith (2006), and hence we document an additional 50 m of section in this classic locality. Regardless of boundary issues, an Early Triassic age is currently assigned to the lower member of the Katberg Formation (Smith et al. 2022).

The ^{238}U-^{206}Pb dates of 243 ± 2 Ma (late Anisian) and 241 ± 3 Ma (early Ladinian), obtained from two samples of calcite-cemented pedogenic nodules, were collected from exposures ~ 15 m apart in the Katberg Formation below the base of the Swartberg member (Fig. 15). They indicate that pedogenic nodule cementation centered around the late Anisian (Middle Triassic), implying a Middle Triassic or younger age for the Swartberg member. These results correspond to data reported from the same stratigraphic interval exposed at the farm Nooitgedacht (Rochín-Bañaga et al. 2023), located 33 km to the west-northwest of the study area. Fossils of the reported *Lystrosaurus* bone bed, attributed to the post-EPME recovery ecosystem at ~ 251 Ma (Smith and Botha 2005; Botha and Smith 2006; Smith and Botha-Brink 2014; Smith et al. 2022), are located only a few tens of meters below the base of the Swartberg member. Thus, they are likely also late Middle Triassic in age.

The results indicate that the Katberg Formation is a highly condensed stratigraphic unit, in which erosional surfaces and, probably, mature paleosols incorporate considerable time. These observations have implications for the continuity of measured sections, interpretation of fluvial style, and inferred unidirectional trends, as explored schematically in Figure 17. For the Swartberg member, the three channel belts taper out westward within shallow valleys, which have 6 m to 20 m of basal relief and are deeply incised at their lowest points and locally elsewhere. In the succession, four fluvial styles are closely associated in a *multi-style system*, with low-sinuosity complexes prominent in thinner, marginal areas. Sheetlike sandstones in the Karoo Basin successions have commonly been attributed to low-sinuosity, ephemeral rivers (e.g., Smith 1995; Smith et al. 2022), but similar deposits (Style 3) form components of all three channel belts, especially the topmost channel belt (Fig. 17). The barforms may include downstream, lateral and oblique components of accretion, and in the absence of paleocurrent data, they could be attributed variously to high- or

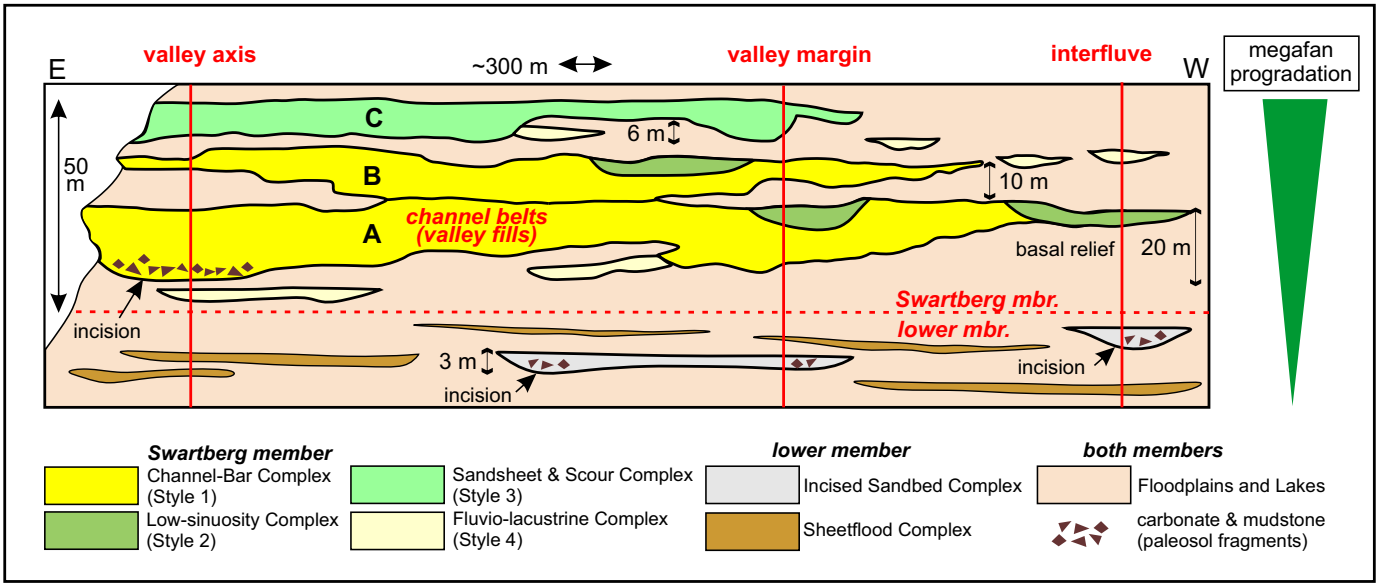

FIG. 17.—Schematic cross section of three channel belts (shallow valleys) in the Swartberg Koppie exposure, based on the E–W face shown in Figure 13B and broadly transverse to paleoflow. The Katberg Formation coarsens up from the lower member to the Swartberg member, linked to northward progradation of a megafan from the Cape Fold Belt and avulsion scenarios. Low-sinuosity complexes could not be identified with the low-resolution 3-D model but are present in similar positions in the S–N face. Information on the lower member from Pace et al. (2009) at Carlton Heights, who documented high-frequency climatic fluctuations superimposed on an architecture of avulsive channel systems. Measured sections in the valley axis, valley margin, and interfluve would show varied stratal thickness, extent of channel units, fluvial style, accumulations of eroded paleosol material, and sites of incision that generate time gaps. Such a complex and discontinuous stratigraphic record is characteristic of dryland alluvial plains and megafans, and careful analysis is required to establish robust trends in fluvial style and paleoclimate.

low-sinuosity systems, especially as many mid-channel bars feature a strong component of lateral accretion (Bristow 1987).

For measured sections in the lower member at Carlton Heights (as illustrated in Fig. 17), Pace et al. (2009) documented suites of narrow fixed channels with basal relief of up to 3 m, pinching out over distances of tens of meters, as well as lenticular sheetflood deposits up to 2 m thick. Channel-lag accumulations of carbonate paleosol fragments (also documented at Bethulie: Smith 1995; Smith et al. 2022), as well as pedogenic mud aggregates (Gastaldo et al. 2013), indicate alternate aggradation and degradation of the landscape, implying the presence of significant diastems. Paleosol characteristics show evidence of fluctuating paleoclimate, with overprinting of older by younger paleosols.

Depending on where sections were measured in the transition from valley axis to valley margin to interfluve (Fig. 17), assessments of stratigraphic continuity, thickness, and fluvial style would be radically different. Similar Quaternary rhythms of aggradation and degradation have been documented for channel and floodplain deposits in the Himalayan Foreland Basin of India, with evidence of high-frequency climatic fluctuation, reworked carbonate and mud clasts linked to floodplain gully erosion, and numerous diastems (Gibling et al. 2005, 2011; Tandon et al. 2006).

Similarly, fluvial systems of the Abrahamskraal and Teekloof formations display a range of styles in complex channel bodies, with a close association of mid-channel and bank-attached bars (downstream and lateral accretion) and no single style dominant (Gulliford et al. 2014; Wilson et al. 2014; see also Bordy and Paiva 2021). Wilson et al. (2014) noted also that incision into semi-consolidated alluvium (including indurated paleosols) influenced fluvial style by confining the channels, disconnecting them from the adjoining floodplain so that they cease to be truly alluvial channels. Gastaldo et al. (2018, 2019a, 2021) found no consistent change in sandstone body or bedset thickness in the Elandsberg and Palingkloof members, beyond local thinning of fluvial sheets or ribbons, closely linked to outcrop orientation with respect to paleoflow. Trough cross-beds were common throughout, a similar range of primary sedimentary structures was present, and intraformational conglomerate was prominent in channel lags throughout the successions, in the form of pedogenic nodules, mudclasts, and bone. Gastaldo et al. (2021) concluded that fluvial style showed little systematic change through the latest Permian and earliest Triassic.

Mudclasts (facies Gl) are prominent at the base of the Swartberg member (Fig. 17) where the avulsing fluvial system incised deeply into floodplain and lacustrine deposits, as well as in the lower member (Pace et al. 2009). Reworked biscuit-shaped wisps and nearly spherical particles of mudstone are widespread in the upper Balfour and Katberg formations (Gastaldo et al. 2015, 2018, 2021; Viglietti et al. 2017), where they have been attributed variously to erosion of short-lived mud drapes in channels and shallow ponds and to erosion of thicker accumulations in abandoned-channel fills and floodplain deposits (e.g., Stear 1978; Hiller and Stavrakis 1980; Stavrakis 1980; Smith 1995; Wilson et al. 2014). Retallack et al. (2003) attributed mudclasts with soil microfabrics in the Palingkloof Member to a global soil-stripping crisis linked to vegetation dieback and landscape destabilization. The inferred first appearance of such clasts, reported to be restricted to the transitional interval, was used as a diagnostic criterion for the onset of aridification (Smith and Ward 2001; Ward et al. 2005; Smith and Botha-Brink 2014, p. 107). However, in view of the abundance of such clasts in fluvial deposits of the Karoo Basin, the Palingkloof occurrences are unlikely to be unique, especially in the absence of a comparable technical analysis of mudclasts at other levels.

Significance of the Katberg Formation in Evaluating Paleoclimate Trends

The Katberg Formation has played, and continues to play, an important role in the interpretation of continental landscapes following the end-Permian ecosystem crisis in South Africa and worldwide. The formation has been interpreted as part of a northward-tapering megafan or DFS (Groenewald 1996), resting on an unconformity with the Balfour Formation (Catuneanu and Elango 2001; Viglietti et al. 2017). A coarsening-upward

succession culminates in the Swartberg member, with subsequent upward fining through the Burgersdorp Formation, with a prominent nonconformity separating the two formations in distal areas (Neveling 2004). A northward paleoflow assessment from our study is in accord with deposition on a megafan building from the Cape Fold Belt (Hiller and Stavrakis 1980; Stavrakis 1980; Neveling 2004). Similarly, the Abrahamskraal and Teekloof formations in the western part of the basin (Fig. 1B) are attributed to deposition on megafans (Gulliford et al. 2014; Bordy and Paiva 2021), and the Molteno Formation was deposited as a clastic wedge in Late Triassic time (Turner 1983; Hancox 1998).

Although more research is needed to explore a megafan model for the Katberg Formation, such a depositional setting needs to be considered when inferring secular change in fluvial style and paleoclimate. Megafans may extend for hundreds of kilometers from mountain exit points (Weissmann et al. 2010), and they display proximal-to-distal trends in fluvial style, as well as progradation and retrogradation due to thrust loading and relaxation in the hinterland (Owen et al. 2017). Fluvial style is highly variable across megafans due to avulsion of major and minor drainage systems (e.g., Sinha et al. 2014; Chesley and Leier 2018), the formation of new fan lobes laterally and downfan (Abrahami et al. 2018), and superimposed high-frequency climatic rhythms that affect channel and floodplain equilibrium profiles (Tandon et al. 2006). Owen et al. (2017) stressed the inherent inhomogeneity and complex surface mosaic of fluvial sequences in DFS successions.

The end-Permian extinction was associated with major changes to vegetation (Looy et al. 2001), with evidence for increased sediment supply in continental ecosystems (Algeo and Twitchett 2010). However, in a DFS context, the abrupt appearance of the Swartberg member is most simply explained by the avulsion into the Bethulie area of a large sandbed river, on the scale of the Platte or the South Saskatchewan. Major river avulsions are well documented for megafans in the Himalayan Foreland Basin, as in the 2008 Kosi River avulsion (Sinha et al. 2014) and the relocation of the Sutlej and Yamuna rivers on their respective fans (Singh et al. 2017). Although climatic changes are likely to have accompanied the relocation of the Swartberg river systems, as with the Sutlej and Yamuna systems (Singh et al. 2017), the tectonically active Cape Fold Belt and Karoo foreland basin provides an obvious explanation for this major change in the fluvial system.

CONCLUSIONS

The importance of the Karoo Basin of South Africa for interpreting end-Permian extinction in continental settings is not in doubt. However, much ambiguity remains about how the landscape evolved, especially as regards the style of fluvial systems, paleoclimate and relative aridity, and landscape stability and sediment flux. Our study assesses the fluvial style and paleoclimate for a key stratigraphic unit, the Swartberg member of the Katberg Formation, previously assigned to the Induan (Early Triassic).

Our approach is to use UAV (drone) images to identify what we term *remote outcrop facies* in the inaccessible cliff face, leading to interpretations of *geomorphic units*. This approach draws on GPR studies of modern rivers, in which the identification of radar facies links the preserved, subsurface strata with the geomorphic units at surface. In this way, we have been able to make a direct comparison between the fluvial style of the Swartberg member and possible modern analogues. The Swartberg member exhibits a predominance of planar-bedded sand sheets and channel-scour fills, as well as a range of mid-channel and, less commonly, bank-attached bars, inviting comparison in scale and geomorphic style with braided rivers in western North America, for which an abundance of GPR data are available. The modest proportion of identifiable barforms with slipfaces in the Swartberg member accords with observations of these modern braided rivers, in which bars accrete at high-stage flow but are reworked during falling and low-stage flow. Observations of dipping accretion surfaces and cross-beds in the cliff sections, aided by rotation of the 3-D model, established a broadly northward paleoflow direction, in accord with regional assessments and deposition on megafans emerging from the Cape Fold Belt, which is known to have been active at least into the Early Triassic.

We were unable to collect fine-scale evidence for paleoclimate from sedimentary structures, hindering comparisons with earlier research (Table 1). However, the predominance of sand sheets with trough cross-beds and the presence of barforms accords with deposition in perennially flowing rivers, and the presence of bar reactivation surfaces and numerous scours suggests strongly seasonal discharge. We infer a relatively humid but seasonal paleoclimate for the Swartberg member. Although river discharge patterns may reflect the paleoclimate of the source area in the Cape Fold Belt, standing water was prominent in lakes and abandoned channels in the Swartberg channel belt. The identification of vegetation-induced sedimentary structures (VISSs) in the channel belt indicates the presence of vegetation, even though macrofloral remains and palynomorphs are scarce (Gastaldo et al. 2005).

Our Middle Triassic geochronometric dates for pedogenic carbonate nodules in strata underlying the Swartberg member, more than seven million years after the Permian–Triassic boundary, requires substantial revision to the age model for the succession. The dates imply that major, currently unidentified gaps in time are present, probably associated with major breaks in the distal part of the basin linked to megafan tectonics, smaller-scale erosional surfaces in the succession, and periods of landscape stasis associated with mature paleosols. Similarly disjunct successions are typical of Quaternary dryland river plains and megafans, where tectonic effects, high-frequency climate rhythms, and autogenic channel relocation cause episodes of aggradation and degradation.

In view of the revised age model and probable time gaps in the succession, we suggest revisiting the inferred unidirectional trend of fluvial style and aridification across the Permian–Triassic boundary in the Karoo Basin. As illustrated by the studies of Fielding et al. (2019, 2021) in Australia and Ji et al. (2023) in China, the end-Permian extinction in terrestrial settings was not necessarily accompanied by changes in fluvial style and climate.

SUPPLEMENTAL MATERIALS

Supplemental materials are available from the SEPM Data Archive: https://www.sepm.org/supplemental-materials.

ACKNOWLEDGMENTS

The authors thank the following colleagues who either assisted during field work in South Africa and/or were instrumental in instructing and facilitating the use of Metashape for the current study: Timothy Stonesifer, Colby College; John W. Geissman, UT-Dallas; Sandra L. Kamo, University of Toronto; and Lucas Joel, University of California–Riverside. We are grateful to Tobi Payenberg, Brian Willis, and an anonymous reviewer for comments that greatly improved the manuscript, and to Alessandro Ielpi for a thoughtful review of an earlier draft. We acknowledge the hospitality and assistance of Tony Hocking and cordial staff of the Royal Hotel Bethulie. Student participation was supported by the Selover Family Student-Research Endowment and Barrett T. Dixon Geology Research-and-Internship Fund for undergraduate experiences in the Department of Geology, Colby College. Research was supported by the Council for Geoscience; National Science Foundation EAR 0749895, 0934077, 1123570, and 1624302; a Fulbright Award to RAG at the Geology Department, Rhodes University; and faculty start-up funding to JWG from the University of Texas at Dallas.

REFERENCES

Abdala, F., Cisneros, J.C., and Smith, R.M.H., 2006, Faunal aggregation in the Early Triassic Karoo Basin: earliest evidence of shelter-sharing behavior among tetrapods? Palaios, v. 21, p. 507–512.

Abdullatif, O.M., 1989, Channel-fill and sheet-flood facies sequences in the ephemeral terminal River Gash, Kassala, Sudan: Sedimentary Geology, v. 63, p. 171–184.

Abrahami, R., Huyghe, P., van der Beek, P., Lowick, S., Carcaillet, J., and Chakraborty, T., 2018, Late Pleistocene–Holocene development of the Tista megafan (West Bengal, India): ^{10}Be cosmogenic and IRSL age constraints: Quaternary Science Reviews, v. 185, p. 69–90.

Algeo, T.J., and Twitchett, R.J., 2010, Anomalous Early Triassic sediment fluxes due to elevated weathering rates and their biological consequences: Geology, v. 38, p. 1023–1026.

Algeo, T.J., Chen, Z.Q., Fraiser, M.L., and Twitchett, R.J., 2011, Terrestrial–marine teleconnections in the collapse and rebuilding of Early Triassic marine ecosystems: Palaeogeography, Palaeoclimatology, Palaeoecology, v. 308, p. 1–11.

Allen, J.R.L., 1983, Studies in fluviatile sedimentation: bars, bar complexes and sandstone sheets (low-sinuosity braided streams) in the Brownstones (L. Devonian), Welsh Borders: Sedimentary Geology, v. 33, p. 237–293.

Arche, A., and López-Gómez, J., 2005, Sudden changes in fluvial style across the Permian–Triassic boundary in the eastern Iberian Ranges, Spain: analysis of possible causes: Palaeogeography, Palaeoclimatology, Palaeoecology, v. 229, p. 104–126.

Benton, M.J., and Newell, A.J., 2014, Impacts of global warming on Permo-Triassic terrestrial ecosystems: Gondwana Research, v. 25, p. 1308–1337.

Best, J.L., Ashworth, P.J., Bristow, C.S., and Roden, J., 2003, Three-dimensional sedimentary architecture of a large, mid-channel sand braid bar, Jamuna River, Bangladesh: Journal of Sedimentary Research, v. 73, p. 516–530.

Billi, P., 2008, Bedforms and sediment transport processes in the ephemeral streams of Kobo basin, Northern Ethiopia: Catena, v. 75, p. 5–17.

Blair, T.C., 1999, Sedimentology of the debris-flow-dominated Warm Spring Canyon alluvial fan, Death Valley, California: Sedimentology, v. 46, p. 941–965.

Blewett, S.C.J., and Phillips, D., 2016, An overview of Cape Fold Belt geochronology: implications for sediment provenance and the timing of orogenesis, *in* Linol, B., and de Wit, M.J., eds., Origin and Evolution of the Cape Mountains and Karoo Basin: Switzerland, Springer International Publishing, p. 44–55.

Blewett, S.C.J., Phillips, D., and Matchan, E.L., 2019, Provenance of Cape Supergroup sediments and timing of Cape Fold Belt orogenesis: constraints from high-precision ^{40}Ar/^{39}Ar dating of muscovite: Gondwana Research, v. 70, p. 201–221.

Blodgett, R.H., and Stanley, K.O., 1980, Stratification, bedforms, and discharge relations of the Platte braided river system, Nebraska: Journal of Sedimentary Petrology, v. 50, p. 139–148.

Bond, D.P.G., and Grasby, S.E., 2017, On the causes of mass extinction: Palaeogeography, Palaeoclimatology, Palaeoecology, v. 478, p. 3–29.

Bordy, E.M., and Krummeck, W.D., 2016, Enigmatic continental burrows from the Early Triassic transition of the Katberg and Burgersdorp formations in the main Karoo Basin, South Africa: Palaios, v. 31, p. 389–403.

Bordy, E.M., and Paiva, F., 2021, Stratigraphic architecture of the Karoo river channels at the end-Capitanian: Frontiers in Earth Science, v. 8, doi:10.3389/feart.2020.521766.

Bordy, E.M., Hancox, P.J., and Rubidge, B.S., 2004, Basin development during the deposition of the Elliot Formation (Late Triassic–Early Jurassic), Karoo Supergroup, South Africa: South African Journal of Geology, v. 107, p. 397–412.

Bordy, E.M., Sztanó, O., Rubidge, B.S., and Bumby, A., 2010, Early Triassic vertebrate burrows from the Katberg Formation of the south-western Karoo Basin, South Africa: Lethaia, v. 44, p. 33–45.

Botha, J., and Smith, R.M.H., 2006, Rapid vertebrate recuperation in the Karoo Basin of South Africa following the End-Permian extinction: Journal of African Earth Sciences, v. 45, p. 502–514.

Botha, J., and Smith, R.M.H., 2020, Biostratigraphy of the *Lystrosaurus declivis* Assemblage Zone (Beaufort Group, Karoo Supergroup), South Africa: South African Journal of Geology, v. 123, p. 207–216.

Botha, J., Huttenlocker, A.K., Smith, R.M.H., Prevec, R., Viglietti, P., and Modesto, S. P., 2020, New geochemical and palaeontological data from the Permian–Triassic boundary in the South African Karoo Basin test the synchronicity of terrestrial and marine extinctions: Palaeogeography, Palaeoclimatology, Palaeoecology, v. 540, doi:10.1016/j.paleo.2019.109467.

Botha-Brink, J., Codron, D., Huttenlocker, A.K., Angielczyk, K.D., and Ruta, M., 2016, Breeding young as a strategy during Earth's greatest mass extinction: Science Reports, v. 6, doi:10.1038/srep24053.

Bridge, J.S., 1993, Description and interpretation of fluvial deposits: a critical perspective: Sedimentology, v. 40, p. 801–810.

Bridge, J.S., 2003, Rivers and Floodplains: Oxford, U.K., Blackwell, 491 p.

Bridge, J.S., Smith, N.D., Trent, F., Gabel, S.L., and Bernstein, P., 1986, Sedimentology and morphology of a low-sinuosity river: Calamus River, Nebraska Sand Hills: Sedimentology, v. 33, p. 851–870.

Bridge, J., Collier, R., and Alexander, J., 1998, Large-scale structure of Calamus River deposits (Nebraska, USA) revealed using ground-penetrating radar: Sedimentology, v. 45, p. 977–986.

Bristow, C.S., 1987, Brahmaputra River: channel migration and deposition, *in* Ethridge, F. G., Flores, R.M., and Harvey, M.D., eds., Recent Developments in Fluvial Sedimentology: SEPM, Special Publication 39, p. 63–74.

Brooks, G.R., 2003, Alluvial deposits of a mud-dominated stream: the Red River, Manitoba, Canada: Sedimentology, v. 50, p. 441–458.

Buatois, L.A., Borruel-Abadía, V., De la Horra, R., Belén Galán-Abellán, A., López-Gómez, J., Barrenechea, J.F., and Arche, A., 2021, Impact of Permian mass extinctions on continental invertebrate infauna: Terra Nova, v. 33, p. 455–464.

Burgess, S.D., Bowring, S.A., and Shen, S.-Z., 2014, High-precision timeline for Earth's most severe extinction: National Academy of Sciences, Proceedings, v. 111, p. 3316–3321.

Burgess, S.D., Muirhead, J.D., and Bowring, S.A., 2017, Initial pulse of Siberian Traps sills as the trigger of the end-Permian mass extinction: Nature Communications, v. 8, doi:10.1038/s41467-017-00083-9.

Cairncross, B., Beukes, N.J., Coetzee, L.L., and Rehfeld, U., 2005, The bivalve *Megadesmus* from the Permian Volksrust Shale Formation (Karoo Supergroup), northeastern Karoo Basin, South Africa: implications for late Permian Basin development: South African Journal of Geology, v. 108, p. 547–556.

Carling, P.A., and Leclair, S.F., 2019, Alluvial stratification styles in a large, flash-flood influenced dryland river: the Luni River, Thar Desert, north-west India: Sedimentology, v. 66, p. 102–128.

Catuneanu, O., and Elango, H.N., 2001, Tectonic control on fluvial styles: the Balfour Formation of the Karoo Basin, South Africa: Sedimentary Geology, v. 140, p. 291–313.

Catuneanu, O., Hancox, P.J., and Rubidge, B.S., 1998, Reciprocal flexural behaviour and contrasting stratigraphies: a new basin development model for the Karoo retroarc foreland system, South Africa: Basin Research, v. 10, p. 417–439.

Catuneanu, O., Wopfner, H., Eriksson, P.G., Cairncross, B., Rubidge, B.S., Smith, R.M. H., and Hancox, P.J., 2005, The Karoo basins of south-central Africa: Journal of African Earth Sciences, v. 43, p. 211–253.

Chesley, J.T., and Leier, A.L., 2018, Sandstone-body variability in the medial–distal part of an ancient distributive fluvial system, Salt Wash Member of the Morrison Formation, Utah, U.S.A.: Journal of Sedimentary Research, v. 88, p. 568–582.

Crowley, K.D., 1983, Large-scale bed configurations (macroforms), Platte River Basin, Colorado and Nebraska: primary structures and formative processes: Geological Society of America, Bulletin, v. 94, p. 117–133.

Cyples, N.N., Ielpi, A., and Dirszowsky, R.W., 2020, Planform and stratigraphic signature of proximal braided streams: remote-sensing and ground-penetrating-radar analysis of the Kicking Horse River, Canadian Rocky Mountains: Journal of Sedimentary Research, v. 90, p. 131–149.

Davies, C.E., Allen, M.B., Buslov, M.M., and Safonova, I.Y., 2010, Deposition in the Kuznetsk Basin, Siberia: insights into the Permian–Triassic transition and the Mesozoic evolution of Central Asia: Palaeogeography, Palaeoclimatology, Palaeoecology, v. 295, p. 307–322.

Davis, D.W., and Rochín-Bañaga, H., 2021, A new Bayesian approach toward improved regression of low-count U–Pb geochronology data generated by LA–ICPMS: Chemical Geology, v. 582, doi:10.1016/j.chemgeo.2021.120454.

Ethridge, F.G., and Schumm, S.A., 1978, Reconstructing paleochannel morphologic and flow characteristics: methodology, limitations, and assessment, *in* Miall, A.D., ed., Fluvial Sedimentology: Canadian Society of Petroleum Geologists, Memoir 5, p. 703–721.

Feldman, H.R., Gibling, M.R., Archer, A.W., Wightman, W.G., and Lanier, W.P., 1995, Stratigraphic architecture of the Tonganoxie Paleovalley Fill (Lower Virgilian) in northeastern Kansas: American Association of Petroleum Geologists, Bulletin, v. 79, p. 1019–1043.

Fielding, C.R., Alexander, J., and Allen, J.P., 2018, The role of discharge variability in the formation and preservation of alluvial sediment bodies: Sedimentary Geology, v. 365, p. 1–20.

Fielding, C.R., Frank, T.D., McLoughlin, S., Vajda, V., Mays, C., Tevyaw, A.P., Winguth, A., Winguth, C., Nicoll, R.S., Bocking, M., and Crowley, J.L., 2019, Age and pattern of the southern high-latitude continental end-Permian extinction constrained by multiproxy analysis: Nature Communications, v. 10, doi:10.1038/s41467-018-07934-z.

Fielding, C.R., Frank, T.D., Tevyaw, A.P., Savatic, K., Vajda, V., McLoughlin, S., Mays, C., Nicoll, R.S., Bocking, M., and Crowley, J.L., 2021, Sedimentology of the continental end-Permian extinction event in the Sydney Basin, eastern Australia: Sedimentology, v. 68, p. 30–62.

Friend, P.F., Slater, M.J., and Williams, R.C., 1979, Vertical and lateral building of river sandstone bodies, Ebro Basin, Spain: Geological Society of London, Journal, v. 136, p. 39–46.

Fryirs, K.A., and Brierley, G.J., 2018, What's in a name? A naming convention for geomorphic river types using the River Styles Framework: PLos ONE, v. 13, doi:10.1371/journal.pone.0201909.

Gastaldo, R.A., and Bamford, M.K., 2023, The influence of taphonomy and time on the paleobotanical record of the Permian–Triassic transition of the Karoo Basin (and elsewhere): Journal of African Earth Sciences, v. 204, doi:10.1016/j.jafrearsci.2023.104960.

Gastaldo, R.A., and Demko, T.M., 2011, Long term hydrology controls the plant fossil record, *in* Allison, P.A., and Bottjer, D.J., eds., Taphonomy, Second Edition: Processes and Bias Through Time: Topics in Geobiology, v. 32, p. 249–286.

Gastaldo, R.A., and Rolerson, M.W., 2008, *Katbergia* gen. nov., a new trace fossil from the Late Permian and Early Triassic of the Karoo Basin: implications for paleoenvironmental conditions at the P/Tr extinction event: Palaeontology, v. 51, p. 215–229.

Gastaldo, R.A., Adendorff, R., Bamford, M., Labandeira, C., Neveling, J., and Sims, H., 2005, Taphonomic trends of macrofloral assemblages across the Permian–Triassic boundary, Karoo Basin, South Africa: Palaios, v. 20, p. 479–497.

Gastaldo, R.A., Pludow, B.A., and Neveling, J., 2013, Mud aggregates from the Katberg Formation, South Africa: additional evidence for Early Triassic degradational landscapes: Journal of Sedimentary Research, v. 83, p. 531–540.

Gastaldo, R.A., Knight, C., Neveling, J., and Tabor, N., 2014, Late Permian Paleosols from Wapadsberg Pass, South Africa: implications for Changhsingian Climate: Geological Society of America, Bulletin, v. 126, p. 665–679.

Gastaldo, R.A., Kamo, S.L., Neveling, J., Geissman, J.W., Bamford, M., and Looy, C., 2015, Is the vertebrate-defined Permian–Triassic Boundary in the Karoo Basin, South Africa, the terrestrial expression of the End Permian marine event?: Geology, v. 43, p. 939–942.

Gastaldo, R.A., Neveling, J., Geissman, J.W., and Kamo, S.L., 2018, A lithostratigraphic and magnetostratigraphic framework in a geochronologic context for a purported Permian–Triassic boundary section at Old (West) Lootsberg Pass, Karoo Basin, South Africa: Geological Society of America, Bulletin, v. 130, p. 1411–1438.

Gastaldo, R.A., Neveling, J., Geissman, J.W., and Looy, C.V., 2019a, Testing the *Daptocephalus* and *Lystrosaurus* Assemblage Zones in a lithostratigraphic, magnetostratigraphic, and palynological framework in the Free State, South Africa: Palaios, v. 34, p. 542–561.

Gastaldo, R.A., Neveling, J., Geissman, J.W., and Li., J.W., 2019b, A multidisciplinary approach to review the vertical and lateral facies relationships of the purported vertebrate-defined terrestrial boundary interval at Bethulie, Karoo Basin, South Africa: Earth Science Reviews, v. 189, p. 220–243.

Gastaldo, R.A., Kamo, S.L., Neveling, J., Geissman, J., Looy, C.V., and Martini, A.M., 2020a, The base of the *Lystrosaurus* Assemblage Zone, Karoo Basin, predates the end-Permian marine extinction: Nature Communications, v. 11, doi:10.1038/s41467-020-15243-7.

Gastaldo, R.A., Tabor, N., and Neveling, J., 2020b, Trends in stable isotopes and climate proxies from late Changhsingian ghost landscapes of the Karoo Basin, South Africa: Frontiers in Ecology and Evolution, v. 8, doi:10.3389/fevo.2020.567109.

Gastaldo, R.A., Neveling, J., Geissman, J.W., Kamo, S.L., and Looy, C.V., 2021, A tale of two Tweefonteins: what physical correlation, geochronology, magnetic polarity stratigraphy, and palynology say about the end-Permian terrestrial extinction paradigm: Geological Society of America, Bulletin, v. 133, p. 691–721.

Ghinassi, M., and Ielpi, A., 2017, Precambrian snapshots: morphodynamics of Torridonian fluvial braid bars revealed by three-dimensional photogrammetry and outcrop sedimentology: Sedimentology, v. 65, p. 492–516.

Gibling, M.R., 2006, Width and thickness of fluvial channel bodies and valley fills in the geological record: a literature compilation and classification: Journal of Sedimentary Research, v. 76, p. 731–770.

Gibling, M.R., Tandon, S.K., Sinha, R., and Jain, M., 2005, Discontinuity-bounded alluvial sequences of the southern Gangetic Plains, India: aggradation and degradation in response to monsoonal strength: Journal of Sedimentary Research, v. 75, p. 369–385.

Gibling, M.R., Fielding, C.R., and Sinha, R., 2011, Alluvial valleys and alluvial sequences: towards a geomorphic assessment, *in* North, C.P., Davidson, S., and Leleu, S., eds., From River to Rock Record: The Preservation of Fluvial Sediments and their Subsequent Interpretation: SEPM, Special Publication 97, p. 423–447.

Gibling, M.R., Ielpi, A., Ghinassi, M., and Buatois, L.A., in press, Alluvial sediments, *in* Levell, B., ed., Reading's Sedimentary Environments: Processes, Facies and Stratigraphy: Wiley.

Gresse, P.G., Theron, J.N., Fitch, F.J., and Miller, J.A., 1992, Tectonic inversion and radiometric resetting of the basement in the Cape Fold Belt, *in* de Wit, M.J., and Ransome, I.G.D., eds., Inversion Tectonics of the Cape Fold Belt, Karoo and Cretaceous Basins of Southern Africa: Rotterdam, Balkema, p. 217–228.

Groenewald, G.H., 1996, Stratigraphy of the Tarkastad Subgroup, Karoo Supergroup, South Africa [Ph.D. Thesis]: University of Port Elizabeth, South Africa, 145 p.

Gulliford, A.R., Flint, S.S., and Hodgson, D.M., 2014, Testing applicability of models of distributive fluvial systems or trunk rivers in ephemeral systems: reconstructing 3-D fluvial architecture in the Beaufort Group, South Africa: Journal of Sedimentary Research, v. 84, p. 1147–1169.

Gulliford, A.R., Flint, S.S., and Hodgson, D.M., 2017, Crevasse splay processes and deposits in an ancient distributive fluvial system: the lower Beaufort Group, South Africa: Sedimentary Geology, v. 358, p. 1–18.

Hajek, E.A., Heller, P.L., and Sheets, B.A., 2010, Significance of channel-belt clustering in alluvial basins: Geology, v. 38, p. 535–538.

Hälbich, I.W., 1992, The Cape Fold Belt Orogeny: State of the art 1970s–1980s, *in* de Wit, M.J., and Ransome, I.G.D., eds., Inversion Tectonics of the Cape Fold Belt, Karoo and Cretaceous Basins of Southern Africa: Rotterdam, Balkema, p. 141–158.

Hancox, P.J., 1998, A stratigraphic, sedimentological and palaeonvironmental synthesis of the Beaufort–Molteno contact in the Karoo Basin [Ph.D. Thesis]: University of the Witwatersrand, Johannesburg, 381 p.

Hancox, P.J., Brandt, D., Reimold, W.U., Koeberl, C., and Neveling, J., 2002, Permian–Triassic boundary in the northwest Karoo basin: current stratigraphic placement, implications for basin development models, and the search for evidence of impact, *in* Koeberl, C., and MacLeod, K.G., eds., Catastrophic Events and Mass Extinctions: Impacts and Beyond: Geological Society of America, Special Paper 356, p. 429–444.

Hansma, J., Tohver, E., Schrank, C., Jourdan, F., and Adams, D., 2016, The timing of the Cape Orogeny: new $^{40}Ar/^{39}Ar$ age constraints on deformation and cooling of the Cape Fold Belt, South Africa: Gondwana Research, v. 32, p. 122–137.

Hill, C.A., Polyak, V.J., Asmerom, Y., and Provencio, P., 2016, Constraints on a Late Cretaceous uplift, denudation, and incision of the Grand Canyon region, southwestern Colorado Plateau, USA, from U–Pb dating of lacustrine limestone: Tectonics, v. 35, p. 896–906.

Hiller, N., and Stavrakis, N., 1980, Distal alluvial fan deposits in the Beaufort Group of the Eastern Cape Province: Geological Society of South Africa, Transactions, v. 83, p. 353–360.

Hiller, N., and Stavrakis, N., 1984, Permo-Triassic fluvial systems in the southeastern Karoo Basin, South Africa: Palaeogeography, Palaeoclimatology, Palaeoecology, v. 45, p. 1–21.

Hofmann, M.H., Wroblewski, A., and Boyd, R., 2011, Mechanisms controlling the clustering of fluvial channels and the compensational stacking of cluster belts: Journal of Sedimentary Research, v. 81, p. 670–685.

Holbrook, J., 2001, Origin, genetic interrelationships, and stratigraphy over the continuum of fluvial channel-form bounding surfaces: an illustration from middle Cretaceous strata, southeastern Colorado: Sedimentary Geology, v. 144, p. 179–222.

Horn, J.D., Fielding, C.R., and Joeckel, R.M., 2012a, Revision of Platte River alluvial facies model through observations of extant channels and barforms, and subsurface alluvial valley fills: Journal of Sedimentary Research, v. 82, p. 72–91.

Horn, J.D., Joeckel, R.M., and Fielding, C.R., 2012b, Progressive abandonment and planform changes of the central Platte River in Nebraska, central USA, over historical timeframes: Geomorphology, v. 139–140, p. 372–383.

Huggenberger, P., 1993, Radar-facies: recognition of facies patterns and heterogeneities within Pleistocene Rhine gravels, NE Switzerland, *in* Best, J.L., and Bristow, C.S., eds., Braided Rivers: Geological Society of London, Special Publication 75, p. 163–176.

Ielpi, A., Gibling, M.R., Bashforth, A.R., and Dennar, C.I., 2015, Impact of vegetation on Early Pennsylvanian fluvial channels: insight from the Joggins Formation of Atlantic Canada: Journal of Sedimentary Research, v. 85, p. 999–1018.

Isbell, J.L., Cole, D.I., and Catuneanu, O., 2008, Carboniferous–Permian glaciation in the main Karoo Basin, South Africa: stratigraphy, depositional controls, and glacial dynamics, *in* Fielding, C.R., Frank, D.K., and Isbell, J.L., eds., Resolving the Late Paleozoic Ice Age in Time and Space: Geological Society of America, Special Publication 441, p. 71–82.

Jackson, R.G., 1976, Depositional model of point bars in the lower Wabash River: Journal of Sedimentary Petrology, v. 46, p. 579–594.

Ji, K., Wignall, P.B., Tong, J., Yu, Y., Guo, W., Shu, W., and Chu, D., 2023, Sedimentology of the latest Permian to Early Triassic in the terrestrial settings of the North China Basin: low-latitude climate change during a warming-driven crisis: Geological Society of America, Bulletin, v. 135, p. 481–503.

Joeckel, R.M. Wooden, S.R., Jr., Korus, J.T., and Garbische, J.O., 2014, Architecture, heterogeneity, and origin of late Miocene fluvial deposits: Sedimentary Geology, v. 311, p. 75–95.

Johnson, M.R., 1976, Stratigraphy and sedimentology of the Cape and Karoo sequences in the Eastern Cape Province [Ph.D. Thesis]: Rhodes University, Grahamstown, 336 p.

Johnson, M.R., Van Vuuren, C.J., Visser, J.N.J., Cole, D.I., Wickens, H.D., Christie, A.D.M., Roberts, D.L., and Brandl, G., 2006, Sedimentary rocks of the Karoo Supergroup, *in* Johnson, M.R., Anhaeusser, C.R., and Thomas, R.J., eds., The Geology of South Africa: Geological Society of South Africa/Council for Geoscience, Pretoria, South Africa, p. 461–500.

Leclair, S.F., and Bridge, J.S., 2001, Quantitative interpretation of sedimentary structures formed by river dunes: Journal of Sedimentary Research, v. 71, p. 713–716.

Li, J., Gastaldo, R.A., Neveling, J., and Geissman, J.W., 2017, Siltstones across the *Daptocephalus* (*Dicynodon*) and *Lystrosaurus* assemblage zones, Karoo Basin, South Africa, show no evidence for aridification: Journal of Sedimentary Research, v. 87, p. 653–671.

Long, D.G.F., 2021, Trickling down the paleoslope: an empirical approach to paleohydrology: Earth-Science Reviews, v. 220, doi:10.1016/j.earscirev.2021.103740.

Looy, C.V., Twitchett, R.J., Dilcher, D.L., Van Konijnenburg-Van Cittert, J.H.A., and Visscher, H., 2001, Life in the end-Permian dead zone: National Academy of Sciences, Proceedings, v. 98, p. 7879–7883.

Lunt, I.A., and Bridge, J.S., 2004, Evolution and deposits of a gravelly braid bar, Sagavanirktok River, Alaska: Sedimentology, v. 51, p. 415–432.

Lunt, I.A., Sambrook Smith, G.A., Best, J.L., Ashworth, P.J., Lane, S.N., and Simpson, C. J., 2013, Deposits of the sandy braided South Saskatchewan River: implications for using modern analogues to reconstruct channel dimensions for use in reservoir characterisation: American Association of Petroleum Geologists, Bulletin, v. 97, p. 553–576.

MacLeod, K.G., Quinton, P.C., and Bassett, D.J., 2017, Warming and increased aridity during the earliest Triassic in the Karoo Basin, South Africa: Geology, v. 45, p. 483–486.

Makaske, B., Lavooi, E., De Haas, T., Kleinhans, M.G., and Smith, D.G., 2017, Upstream control of river anastomosis by sediment overloading, upper Columbia River, British Columbia, Canada: Sedimentology, v. 64, p. 1488–1510.

McElwain, J.C., and Punyasena, S.W., 2007, Mass extinction events and the plant fossil record: Trends in Ecology and Evolution, v. 22, p. 548–557.

Miall, A.D., 1978, Lithofacies types and vertical profile models in braided river deposits: a summary, *in* Miall, A.D., ed., Fluvial Sedimentology: Canadian Society of Petroleum Geologists, p. 597–604.

Miall, A.D., 1996, The Geology of Fluvial Deposits: New York, Springer-Verlag, 582 p.

Midwinter, D., Hadlari, T., and Dewing, K., 2017, Lower Triassic river-dominated deltaic successions from the Sverdrup Basin, Canadian Arctic: Palaeogeography, Palaeoclimatology, Palaeoecology, v. 476, p. 55–67.

Modesto, S.P., 2020, The disaster taxon *Lystrosaurus*: a paleontological myth: Frontiers in Earth Science, v. 8, doi:10.3389/feart.2020.610463.

Mumpy, A.J., Jol, H.M., Kean, W.F., and Isbell, J.L., 2007, Architecture and sedimentology of an active braid bar in the Wisconsin River based on 3-D ground penetrating radar, *in* Baker, G.S., and Jol, H.M., eds., Stratigraphic Analyses Using GPR: Geological Society of America, Special Paper 432, p. 111–131.

Nanson, G.C., 1980, Point bar and floodplain formation of the meandering Beatton River, northeastern British Columbia, Canada: Sedimentology, v. 27, p. 3–29.

Nesbit, P.R., Durkin, P.R., Hugenholtz, C.H., Hubbard, S.M., and Kucharczyk, M., 2018, 3-D stratigraphic mapping using a digital outcrop model derived from UAV images and structure-from-motion photogrammetry: Geosphere, v. 14, p. 2469–2486.

Neveling, J., 2004, Stratigraphic and sedimentological investigation of the contact between the *Lystrosaurus* and the *Cynognathus* Assemblage Zones (Beaufort Group: Karoo Supergroup): Council for Geoscience, Bulletin 137, 164 p.

Neveling, J., Gastaldo, R.A., Kamo, S.L., Geissman, J.W., Looy, C.V., and Bamford, M.K., 2016a, A review of stratigraphic, geochemical, and paleontologic correlations data of the terrestrial end-Permian record in the Karoo Basin, South Africa, *in* Linol, B., and de Wit, M., eds., Origin and Evolution of the Cape Mountains and Karoo Basin: Springer Publishing, Regional Geology Reviews, p. 151–157.

Neveling, J., Gastaldo, R.A., and Geissman, J.W., 2016b, The Permo–Triassic Boundary in the Karoo Basin: Pretoria, Council for Geoscience, 35th International Geological Congress, Pre-Meeting Field Trip Guide P-3, 102 p, doi:10.13140/RG.2.2.22414.15683.

Newell, A.J., Tverdokhlebov, V.P., and Benton, M.J., 1999, Interplay of tectonics and climate on a transverse fluvial system, Upper Permian, Southern Uralian Foreland Basin, Russia: Sedimentary Geology, v. 127, p. 11–29.

Ogg, J.G., Ogg, G.M., and Gradstein, F.M., 2016, A Concise Geologic Time Scale 2016: Amsterdam, Elsevier, 234 p.

Owen, A., Ebinghaus, A., Hartley, A.J., Santos, M.G.M., and Weissmann, G.S., 2017, Multi-scale classification of fluvial architecture: an example from the Palaeocene–Eocene Bighorn Basin, Wyoming: Sedimentology, v. 64, p. 1572–1596.

Pace, D.W., Gastaldo, R.A., and Neveling, J., 2009, Early Triassic aggradational and degradational landscapes of the Karoo basin and evidence for climate oscillation following the P–Tr Event: Journal of Sedimentary Research, v. 79, p. 316–331.

Page, K.J., Nanson, G.C., and Frazier, P.S., 2003, Floodplain formation and sediment stratigraphy resulting from oblique accretion on the Murrumbidgee River, Australia: Journal of Sedimentary Research, v. 73, p. 5–14.

Palafox, L.E.A., Montañez, I., McLean, N.M., Möller, A., and Tabor, N.J., 2022, U-Pb carbonate dating of earliest diagenetic cements within paleosol carbonate nodules: preliminary work and future opportunities: Geological Society of America, Abstracts with Programs, v. 54, doi:10.1130/abs/2022AM-380880.

Parker, N.O., Sambrook Smith, G.H., Ashworth, P.J., Best, J.L., Lane, S.N., Lunt, I.A., Simpson, C.J., and Thomas, R.E., 2013, Quantification of the relation between surface morphodynamics and subsurface sedimentological product in sandy braided rivers: Sedimentology, v. 60, p. 820–839.

Retallack, G.J., 2021, Multiple Permian–Triassic life crises on land and at sea: Global and Planetary Change, v. 198, doi:10.1016/j.gloplacha.2020.103415.

Retallack, G.J., Smith, R.M.H., and Ward, P.D., 2003, Vertebrate extinction across Permian–Triassic boundary in Karoo Basin, South Africa: Geological Society of America, Bulletin, v. 115, p. 1133–1152.

Roberts, N.M.W., Rasbury, T., Parrish, R.R., Smith, C.J., Horstwood, M.S.A., and Condon, D.J., 2017, A calcite reference material for LA-ICP-MS U-Pb geochronology: Geochemistry Geophysics Geosystems, v. 18, p. 2807–2814.

Rochín-Bañaga, H., Gastaldo, R.A., Davis, D.W., Neveling, J., Kamo, S.L., Looy, C.V., and Geissman, J.W., 2023, U–Pb dating of pedogenic calcite near the Permian–Triassic boundary, Karoo Basin, South Africa: Geological Society of America, Bulletin, v. 135, doi.org/10.1130/B36968.

Rubidge, B.S., Hancox, P.J., and Mason, R., 2012, Waterford Formation in the southeastern Karoo: implications for basin development: South African Journal of Science, v. 108, p. 1–5.

Rubidge, B.S., Erwin, D.H., Ramezani, J., Bowring, S.A., and De Klerk, W.J., 2013, High-precision temporal calibration of Late Permian vertebrate biostratigraphy: U-Pb zircon constraints from the Karoo Supergroup, South Africa: Geology, v. 41, p. 363–366.

Rygel, M.C., Gibling, M.R., and Calder, J.H., 2004, Vegetation–induced sedimentary structures from fossil forests in the Pennsylvanian Joggins Formation, Nova Scotia: Sedimentology, v. 51, p. 531–552.

Sambrook Smith, G.H., Ashworth, P.J., Best, J.L., Woodward, J., and Simpson, C.J., 2006, The sedimentology and alluvial architecture of the sandy braided South Saskatchewan River, Canada: Sedimentology, v. 53, p. 413–434.

Sambrook Smith, G.H., Ashworth, P.J., Best, J.L., Lunt, I.A., Orfeo, O., and Parsons, D. R., 2009, The sedimentology and alluvial architecture of a large braid bar, Rio Parana, Argentina: Journal of Sedimentary Research, v. 79, p. 629–642.

Sambrook Smith, G.H., Nicholas, A.P., Best, J.L., Bull, J.M., Dixon, S.J., Goodbred, S., Sarkar, M.H., and Vardy, M.E., 2019, The sedimentology of river confluences: Sedimentology, v. 66, p. 391–407.

Sasajima, T., Gastaldo, R.A., and Neveling, J., 2015, Using drone technology to characterize the Katberg Sandstone above the Permian–Triassic boundary at Old Wapadsberg Pass, Karoo Basin, South Africa [Abstract]: Geological Society of America, Annual Meeting, Abstracts with Program, v. 47, p. 570.

Sephton, M.A., Jiao, D., Engel, M.H., Looy, C.V., and Visscher, H., 2015, Terrestrial acidification during the end-Permian biosphere crisis?: Geology, v. 43, p. 159–162.

Seton, M., Muller, R.D., Zahirovic, S., Gaina, C., Torsvik, T., Shephard, G., Talsma, A., Gurnis, M., Turner, M., Maus, S., and Chandler, M., 2012, Global continental and ocean basin reconstructions since 200 Ma: Earth-Science Reviews, v. 113, p. 212–270.

Simon, S.S.T., Gibling, M.R., DiMichele, W.A., Chaney, D.S., Looy, C.V., and Tabor, N.J., 2016, An abandoned-channel fill with exquisitely preserved plants in redbeds of the Clear Fork Formation, Texas, USA: an Early Permian water-dependent habitat on the arid plains of Pangea: Journal of Sedimentary Research, v. 86, p. 944–964.

Singh, A., Thomsen, K.J., Sinha, R., Buylaert, J.-P., Carter, A., Mark, D.F., Mason, P.J., Densmore, A.L., Murray, A.S., Jain, M., Paul, D., and Gupta, S., 2017, Counter-intuitive influence of Himalayan river morphodynamics on Indus Civilisation urban settlements: Nature Communications, v. 8, doi:10.1038/s41467-017-01643-9.

Sinha, R., Sripriyanka, K., Jain, V., and Mukul, M., 2014, Avulsion threshold and planform dynamics of the Kosi River in north Bihar (India) and Nepal: a GIS framework: Geomorphology, v. 216, p. 157–170.

Sixsmith, P.J., Flint, S.S., Wickens, H.D., and Johnson, S.D., 2004, Anatomy and stratigraphic development of a Basin floor turbidite system in the Laingsburg Formation, Main Karoo Basin, South Africa: Journal of Sedimentary Research, v. 74, p. 239–254.

Skelly, R.L., Bristow, C.S., and Ethridge, F.G., 2003, Architecture of channel-belt deposits in an aggrading shallow sandbed braided river: the lower Niobrara River, northeast Nebraska: Sedimentary Geology, v. 158, p. 249–270.

Smith, N.D., 1970, The braided stream depositional environment: comparison of the Platte River with some Silurian clastic rocks, north-central Appalachians: Geological Society of America, Bulletin, v. 81, p. 2993–3014.

Smith, N.D., 1971, Transverse bars and braiding in the lower Platte River, Nebraska: Geological Society of America, Bulletin, v. 82, p. 3407–3420.

Smith, N.D., 1972, Some sedimentological aspects of planar cross-stratification in a sandy braided river: Journal of Sedimentary Petrology, v. 42, p. 624–634.

Smith, R.M.H., 1980, The lithology, sedimentology and taphonomy of flood-plain deposits of the Lower Beaufort (Adelaide Subgroup) strata near Beaufort West: Geological Society of South Africa, Transactions, v. 83, p. 399–413.

Smith, R.M.H., 1987, Morphology and depositional history of exhumed Permian point bars in the southwestern Karoo, South Africa: Journal of Sedimentary Petrology, v. 57, p. 19–29.

Smith, R.M.H., 1993a, Sedimentology and ichnology of floodplain paleosurfaces in the Beaufort Group (Late Permian), Karoo Sequence, South Africa: Palaios, v. 8, p. 339–357.

Smith, R.M.H., 1993b, Vertebrate taphonomy of Late Permian floodplain deposits in the southwestern Karoo Basin of South Africa: Palaios, v. 8, p. 45–67.

Smith, R.M.H., 1995, Changing fluvial environments across the Permian–Triassic boundary in the Karoo basin, S. Africa and possible causes of tetrapod extinctions: Palaeogeography, Palaeoclimatology, Palaeoecology, v. 117, p. 81–104.

Smith, R.M.H., and Botha, J., 2005, The recovery of terrestrial vertebrate diversity in South African Karoo basin after the end-Permian extinction: Compte Rendu Palevol, v. 4, p. 623–636.

Smith, R.M.H., and Botha-Brink, J., 2014, Anatomy of a mass extinction: sedimentological and taphonomic evidence for drought-induced die-offs at the Permo-Triassic boundary in the Main Karoo Basin, South Africa: Palaeogeography, Palaeoclimatology, Palaeoecology, v. 316, p. 99–118.

Smith, R.M.H., and Ward, P.D., 2001, Pattern of vertebrate extinctions across an event bed at the Permian–Triassic boundary in the Karoo Basin of South Africa: Geology, v. 29, p. 1147–1150.

Smith, R.M.H., Botha, J., and Viglietti, P.A., 2022, Taphonomy of drought afflicted tetrapods in the Early Triassic Karoo Basin, South Africa: Palaeogeography, Palaeoclimatology, Palaeoecology, v. 604, doi:10.1016/j.palaeo.2022.111207.

Smith, R.M.H., Rubidge, B.S., Day, M.O., and Botha, J., 2020, Introduction to the tetrapod biozonation of the Karoo Supergroup: South African Journal of Geology, v. 123, p. 131–140.

Stavrakis, N., 1980, Sedimentation of the Katberg Sandstone and adjacent formation in the southeastern Karoo Basin: Geological Society of South Africa, Transactions, v. 83, p. 361–374.

Stear, W.M., 1978, Sedimentary structures related to fluctuating hydrodynamic conditions in flood plain deposits of the Beaufort Group near Beaufort West, Cape: Geological Society of South Africa, Transactions, v. 81, p. 393–399.

Stear, W.M., 1980, Channel sandstone and bar morphology of the Beaufort Group uranium district near Beaufort West: Geological Society of South Africa, Transactions, v. 83, p. 391–398.

Stear, W.M., 1983, Morphological characteristics of ephemeral stream channel and overbank splay sandstone bodies in the Permian Lower Beaufort Group, Karoo Basin, South Africa, *in* Collinson, J.D., and Lewin, J., eds., Modern and Ancient Fluvial

Systems: International Association of Sedimentologists, Special Publication 6, p. 405–420.

Stear, W.M., 1985, Comparison of the bedform distribution and dynamics of modern and ancient sandy ephemeral flood deposits in the southwestern Karoo region, South Africa: Sedimentary Geology, v. 45, p. 209–230.

Stonesifer, T., Jia, R., Gastaldo, R.A., and Neveling, J., 2018, Using drone technology, photogrammetry, and virtual reality in the analysis of remote and inaccessible classic localities: the vertebrate-defined Permian–Triassic section on the Bethel Farm, Free State Province, South Africa [Abstract]: Geological Society of America, Abstracts with Program, v. 50, doi:10.1130/abs/2018AM-318053.

Strong, N., and Paola, C., 2008, Valleys that never were: time surfaces versus stratigraphic surfaces: Journal of Sedimentary Research, v. 78, p. 579–593.

Tandon, S.K., Gibling, M.R., Sinha, R., Singh, V., Ghazanfari, P., Dasgupta, A.S., Jain, M., and Jain, V., 2006, Alluvial valleys of the Gangetic Plains, India: timing and causes of incision, *in* Dalrymple, R.W., Leckie, D.A., and Tillman, R.W., eds., Incised Valleys in Time and Space: SEPM, Special Publication 85, p. 15–35.

Tockner, K., Ward, J.V., Arscott, D.B., Edwards, P.J., Kollmann, J., Gurnell, A.M., Petts, G.E., and Maiolini, B., 2003, The Tagliamento River: a model ecosystem of European importance: Aquatic Sciences, v. 65, p. 239–253.

Turner, B.R., 1983, Braidplain deposition of the Upper Triassic Molteno Formation in the main Karoo (Gondwana) Basin, South Africa: Sedimentology, v. 30, p. 77–89.

Underwood, J.R., Jr., and Lambert, W., 1974, Centroclinal cross strata, a distinctive sedimentary structure: Journal of Sedimentary Petrology, v. 44, p. 1111–1113.

Viglietti, P.A., Smith, R.M.H., and Compton, J.S., 2013, Origin and palaeoenvironmental significance of *Lystrosaurus* bonebeds in the earliest Triassic Karoo Basin, South Africa: Palaeogeography, Palaeoclimatology, Palaeoecology, v. 392, p. 9–21.

Viglietti, P.A., Smith, R.M.H., Angielczyk, K.D., Kammerer, C.F., Fröbisch, J., and Rubidge, B.S., 2016, The *Daptocephalus* Assemblage Zone (Lopingian), South Africa: a proposed biostratigraphy based on a new compilation of stratigraphic ranges: Journal of African Earth Sciences, v. 113, p. 153–164.

Viglietti, P., Rubidge, B., and Smith, R.M.H., 2017, Revised lithostratigraphy of the Upper Permian Balfour and Teekloof formations of the main Karoo Basin, South Africa: South African Journal of Geology, v. 120, p. 45–60.

Viglietti, P.A., Smith, R.M.H., and Rubidge, B.S., 2018, Changing palaeoenvironments and tetrapod populations in the *Daptocephalus* Assemblage Zone (Karoo Basin, South Africa) indicate early onset of the Permo–Triassic mass extinction: Journal of African Earth Science, v. 138, p. 102–111.

Viglietti, P.A., 2020, Biostratigraphy of the *Daptocephalus* Assemblage Zone (Beaufort Group, Karoo Supergroup), South Africa: South African Journal of Geology, v. 123, p. 191–206.

Walker, S., and Holbrook, J., 2022, Structures, architecture, vertical profiles, palaeohydrology and taphonomy of an upper-flow-regime-dominated fluvial system, the Triassic Dockum Group of the Palo Duro Canyon, Texas: Sedimentology, v. 70, p. 645–684.

Wang, J., and Plink-Björklund, P., 2020, Variable-discharge-river macroforms in the Sunnyside Delta interval of the Eocene Green River Formation, Uinta Basin, USA: Sedimentology, v. 67, p. 1914–1950.

Ward, P.D., Montgomery, D.R., and Smith, R.H.M., 2000, Altered river morphology in South Africa related to the Permian–Triassic extinction: Science, v. 289, p. 1740–1743.

Ward, P.D., Botha, J., Buick, R., De Kock, M.O., Erwin, D.H., Garrison, G.H., Kirschvink, J.L., and Smith, R., 2005, Abrupt and gradual extinction among Late Permian land vertebrates in the Karoo Basin, South Africa: Science, v. 307, p. 709–714.

Weissmann, G.S., Hartley, A.J., Nichols, G.J., Scuderi, L.A., Olson, M., Buehler, H., and Banteah, R., 2010, Fluvial form in modern continental sedimentary basins: distributive fluvial systems: Geology, v. 38, p. 39–42.

Wheaton, J.M., Fryirs, K.A., Brierley, G.J., Bangen, S.G., Bouwes, N., and O'Brien, G., 2015, Geomorphic mapping and taxonomy of geomorphic landforms: Geomorphology, v. 248, p. 273–295.

Williams, R.T., and Fryirs, K.A., 2021, The morphology and geomorphic evolution of a large chain-of-ponds river system: Earth Surface Processes and Landforms, v. 45, p. 1732–1748.

Wilson, A., Flint, S., Payenberg, T., Tohver, E., and Lanci, L., 2014, Architectural styles and sedimentology of the fluvial Lower Beaufort Group, Karoo Basin, South Africa: Journal of Sedimentary Research, v. 84, p. 326–348.

Wooldridge, C.L., and Hickin, E.J., 2005, Radar architecture and evolution of channel bars in wandering gravel-bed rivers: Fraser and Squamish rivers, British Columbia, Canada: Journal of Sedimentary Research, v. 75, p. 844–860.

Zhu, Z., Liu, Y., Kuang, H., Benton, M., Newell, A., Xu, H., An, W., Xu, S., Peng, N., and Zhai, Q., 2019, Altered fluvial patterns in North China indicate rapid climate change linked to the Permian–Triassic mass extinction: Scientific Reports, v. 9, doi:10.1038/s41598-019-53321-z.

Received 10 March 2023; accepted 17 July 2023.